8-11-2015

Computational Study in Chaotic Dynamical Systems and Mechanisms for Pattern Generation in Three-Cell Networks

Tingli Xing

COMPUTATIONAL STUDY IN CHAOTIC DYNAMICAL SYSTEMS AND MECHANISMS FOR PATTERN GENERATION IN THREE-CELL NETWORKS

by

TINGLI XING

Under the Direction of Andrey Shilnikov, PhD

ABSTRACT

A computational technique is introduced to reveal the complex intrinsic structure of homoclinic and heteroclinic bifurcations in a chaotic dynamical system. This technique is applied to several Lorenz-like systems with a saddle at the center, including the Lorenz system, the Shimizu-Morioka model, the homoclinic garden model, and the laser model. A multi-fractal, self-similar organization of heteroclinic and homoclinic bifurcations of saddle singularities is explored on a bi-parametric plane of those dynamical systems. Also a great

detail is explored in the Shimizu-Morioka model as an example. The technique is also applied to a reflexion symmetric dynamical system with a saddle-focus at the center (Chua's circuits). The layout of the homoclinic bifurcations near the primary one in such a system is studied theoretically, and a scalability ratio is proved. Another part of the dissertation explores the intrinsic mechanisms of escape in a reciprocally inhibitory FitzHugh-Nagumo type three-cell network, using the phase-lag technique. The escape network can produce phase-locked states such as pace-makers, traveling-waves, and peristaltic patterns with recurrently phase-lag varying.

INDEX WORDS: Saddle, Saddle-focus, Lorenz attractor, Homoclinic, Heteroclinic, T-point, Kneading invariant, Chaos, Escape, Phase-lag, CPG, Inhibitory, Pace-maker, Traveling-wave.

COMPUTATIONAL STUDY IN CHAOTIC DYNAMICAL SYSTEMS AND MECHANISMS FOR PATTERN GENERATION IN THREE-CELL NETWORKS

by

TINGLI XING

A Dissertation Submitted in Partial Fulfillment of the Requirements for the Degree of

Doctor of Philosophy

in the College of Arts and Sciences

Georgia State University

2015

COMPUTATIONAL STUDY IN CHAOTIC DYNAMICAL SYSTEMS AND MECHANISMS FOR PATTERN GENERATION IN THREE-CELL NETWORKS

by

TINGLI XING

Committee Chair: Andrey Shilnikov

Committee: Igor Belykh

Vladimir Bondarenko

Remus Osan

Electronic Version Approved:

Office of Graduate Studies

College of Arts and Sciences

Georgia State University

August 2015

DEDICATION

This dissertation is dedicated to Georgia State University.

ACKNOWLEDGEMENTS

My PhD. research was funded by NSF grant DMS-1009591. This dissertation work would not have been possible without the support of many people. I am very grateful for all the inspiration, motivation and support that my adviser, Dr. Andrey Shilnikov, has provided. I also want to express my gratitude to many of my professors: Dr. Igor Belykh, Dr. Vladimir Bondarenko, Dr. Frank Hall, Dr. Zhongshan Li, Dr. Imre Patyi, Dr. Xin Qi, Dr. Gengsheng Qin, Dr. Yuanhui Xiao and Dr. Yongwei Yao have all imparted their knowledge warmly. I appreciate all the support that the mathematics and neuroscience departments have offered; and especially, I want to thank Dr. Alexandra Smirnova and Dr. Guantao Chen for their confidence. I want to thank Sandra Ahuama-Jonas and Yvonne Pierce in the mathematics department for their wonderful service. I want to thank Sutandra Sarkar for her excellent coordinator work when I taught pre-calculus. I want to thank Rob Poh, Anwar Lopez, Ryan Sleeth and Fatima Adams for great tech and facility support in the neuroscience department. I want to thank Rob Clewley for helping me with PyDSTool coding. I want to thank my labmates, Deniz Alacam, Jarod Collens, Aaron Kelly, Drake Knapper, Ana Noriega, Krishna Pusuluri, Justus Schwabedal and Jeremy Wojcik for sharing research life with me. At last but not least, I want to thank my husband, Martin A. Crowe and his family for their support. Especially, I want thank my sister in-law, Cathrine Keller. Additionally, I would like to acknowledge my mother, my late father and my brother for always encouraging me to do research.

TABLE OF CONTENTS

ACKNOWLEDGEMENTS . . . . . **v**

LIST OF FIGURES . . . . . **ix**

LIST OF ABBREVIATIONS . . . . . **xii**

PART 1 INTRODUCTION **1**

1.1 Basic Dynamical Systems Knowledge 1

1.1.1 Linear dynamical system 2

1.1.2 Nonlinear dynamical system 4

1.1.3 Periodic orbit 4

1.1.4 Bifurcations of dynamical systems 5

1.1.5 Homoclinic loop 7

1.2 Neural Network Modeling 12

1.2.1 The Hodgkin-Huxley model (Wikipedia) 14

1.2.2 The Theta model (Wikipedia) 15

1.2.3 The FitzHugh-Nagumo model (Wikipedia) 15

PART 2 SYMBOLIC QUEST INTO HOMOCLINIC CHAOS . . **17**

2.1 The Shimizu-Morioka model 20

2.1.1 Bykov T-points 24

2.2 Symbolic description via kneadings 25

2.3 Symbolic sweeping: swirls and saddles 29

2.4 Self-similarity of homoclinic swirls 32

2.5 Inclination-switch bifurcations 33

2.6 Shilnikov flames 36

2.7 Wild chaos in phase & parameter space 38

2.7.1 Elliptic islands and saddles 40
2.8 "Saddle-node" bifurcations in 3D-parametric sweeps 41
2.9 Precursor of inclination-switching 43
2.10 Model of homoclinic garden (HG) 44
2.11 Lorenz Model: Primary and Secondary T-points 47

PART 3 ORDERED INTRICACY OF HOMOCLINIC OF THE SHILNIKOV SADDLE-FOCUS IN REFLEXION SYMMETRIC SYSTEMS **50**

3.1 An analytical approach of homoclinic bifurcation (HB) structure of a Shilnikov saddle-focus in a reflexion symmetric system 51
3.1.1 $(1,1)$ or right double-loop homoclinic bifurcation 54
3.1.2 $(1,0)$ or left double-loop homoclinic bifurcation 57
3.1.3 $(1,1,1)$ or right triple-loop homoclinic bifurcation 58
3.1.4 $(1,0,0)$ or left triple-loop homoclinic bifurcation 64
3.1.5 $(1,1,1,\cdots)$ or right multi-loop homoclinic bifurcation 67
3.1.6 $(1,0,0,\cdots)$ or left multi-loop homoclinic bifurcation 69
3.1.7 Mixed multi-loop homoclinic bifurcation 70
3.2 Homoclinic bifurcation structure sweeping of a Chua's circuit by a computational method 73
3.2.1 The introduction of the computational method 73
3.2.2 $(1,1,1,\ldots)$ or right multi-loop homoclinic bifurcation curves . . . 77
3.2.3 $(1,0,0,\ldots)$ or left multi-loop homoclinic bifurcation curves 79
3.2.4 Mixed multi-loop homoclinic bifurcation curves 80

PART 4 INTRINSIC MECHANISMS STUDY IN THREE ESCAPE CELLS NETWORKS **83**

4.1 Fitzhugh-Nagumo model 83
4.2 3-cell escape network 84

4.3 Symmetric 3-cell network 85

4.4 Asymmetric 3-cell network 87

PART 5 CONCLUSIONS **91**

LIST OF FIGURES

Figure 1.1 Dynamics Near a Homoclinic Orbit 8

Figure 1.2 The Poincaré mapping on Π_0 when $\nu_0 < 1$ and $A > 0$ 9

Figure 1.3 The Poincaré mapping on Π_0 when $\nu_0 > 1$ and $A > 0$ 9

Figure 1.4 The Poincaré mapping on Π_0 when $\nu_0 < 1$ and $A < 0$ 10

Figure 1.5 The Poincaré mapping on Π_0 when $\nu_0 > 1$ and $A < 0$ 10

Figure 1.6 Neuron Sketch 13

Figure 1.7 The FitzHugh-Nagumo model 15

Figure 2.1 Symbolic Sequence 18

Figure 2.2 Structure Sketching of T-points by Bykov 19

Figure 2.3 L.P. Shilnikov's Sketch (1967) of an Inclination-Switch Homoclinic Bifurcation en a Route from an Orientable 20

Figure 2.4 Bi-parametric Sweep of the SM Model Using Lyapunov Exponents (LE) 21

Figure 2.5 The Bi-parametric Sweep of The Shimizu-Morioka Model 23

Figure 2.6 The Fractal Structure of T-points 26

Figure 2.7 An Inclination Homoclinic Bifurcation 30

Figure 2.8 Bi-parametric LE-Sweep of the Shimizu-Morioka Model 31

Figure 2.9 LE-Sweep of a Shilnikov Flame 34

Figure 2.10 Magnification into the vicinity of the T_2-point at two different resolutions 35

Figure 2.11 A Center Region in the SM Model 37

Figure 2.12 3D Kneading Diagrams of the SM model 39

Figure 2.13 The Bifurcation Diagram of the SM model at $B = 0.11$ and $B = 0.125$ 41

Figure 2.14 Slow-Fast Dynamics of the SM-model 42

Figure 2.15 Pilot bi-parameter sweeping of the HG-model 45

Figure 2.16 High resolution scan of dynamics of the HG-model 46
Figure 2.17 Bi-parametric scans of the Lorenz equation around the primary T-point 48
Figure 2.18 Bi-parametric sweeping of the Lorenz equation around the secondary T-point 49
Figure 3.1 Bifurcation Diagram of the Chua's Circuit 51
Figure 3.2 A Standard Reflexion Symmetric System with a Shilnikov Saddle-Focus 53
Figure 3.3 Two Plots Illustrating the Region of the Double-loop HBs in the Case That $B_0 < 1$ 55
Figure 3.4 Two Plots Illustrating the Region of the Double-loop HBs in the Case That $B_0 > 1$ 57
Figure 3.5 Illustration of the Dynamics of the Triple-loop Strips 59
Figure 3.6 Two Plots Illustrating the Region of the Right Triple-loop HBs in the Case That $B_0 < 1$ 60
Figure 3.7 Two Plots Illustrating the Region of Right Triple-loop HBs in the Case That $B_0 > 1$ 61
Figure 3.8 Two Plots Illustrating the Region of Left Triple-loop HBs in the Case That $B_0 > 1$ 65
Figure 3.9 Two plots illustrating the region of Left Triple-loop HBs in the case that $B_0 < 1$ 66
Figure 3.10 The Dynamics of the Strips 69
Figure 3.11 The Mix Multi-loop HBs 71
Figure 3.12 Symbolic Sequence Recording in the Chua's Circuit 74
Figure 3.13 The Structure Plots of the Chua's Circuit 75
Figure 3.14 The HB Unfolding by the Kneading Tool 76
Figure 3.15 The Unfolding of Right Multi-loop HBs in the Chua's Circuit . . 78
Figure 3.16 The Bridge and the "Y" Shape 79

Figure 3.17 The Unfolding of the Left Multi-loop HBs in the Chua's Circuit . 80
Figure 3.18 The Unfolding of the Mix Multi-loop HBs in the Chua's Circuit . 81
Figure 4.1 One Cell Dynamical Diagram 83
Figure 4.2 3-cell network connection 84
Figure 4.3 Symmetric Phase Plots of the 3-Cell Network at $\epsilon = 0.25$ 86
Figure 4.4 Symmetric Phase Plots of the 3-Cell Network at $\epsilon = 0.07$ 87
Figure 4.5 Asymmetric Phase Plots of the 3-Cell Network Increasing the Value of g_{31} 87
Figure 4.6 Asymmetric Phase Plots of the 3-Cell Network Decreasing the value of g_{31} 88
Figure 4.7 Asymmetric Phase Plots of the 3-Cell Networks When Changing the Connections Between the First and Third Cells 89
Figure 4.8 Circle Connections of the 3-Cell Network 90
Figure 4.9 The King of the Mountain Case 90
Figure 5.1 A T-point Plot in the Chua's Circuit 93

LIST OF ABBREVIATIONS

- CPG - Central Pattern Generator
- GSU - Georgia State University
- HB - Homoclinic Bifurcation
- PM - Pace-Maker
- TW - Traveling-Wave
- SM - Shimizu-Morioka
- HG - Homoclinic Garden
- HCO - Half Center Oscillator
- IPSP - Inhibitory Post-Synaptic Potential
- EPSP - Excitatory Post-Synaptic Potential
- SN - Saddle-Node
- SF - Saddle-Focus
- PD - Period-Doubling

PART 1

INTRODUCTION

1.1 Basic Dynamical Systems Knowledge

Dynamical phenomena are everywhere, such as traffic, biology, physics, astronomy, weather, etc. Their mathematical models (if a model can be developed) may be expressed by ordinary differential equations, partial differential equations or other forms. The models involved in this dissertation are all described by ordinary differential equations, more precisely first-order autonomous ordinary differential equations that do not explicitly depend on independent variables. The general expression is

$$\frac{dx}{dt} = X(x), \tag{1.1}$$

where the dependent variable x is in the phase space $\mathcal{M}$ ($\mathcal{M} = \mathbb{R}^n$ or torus $\mathbb{T}^n$) and the independent variable t is time. Its solution of initial x_0, $x(t)$, can be written as $x(t) = S^t(x_0)$, where S^t is a family of evolution functions that maps $\mathcal{M}$ to itself. It implies the deterministic rule that $x(t)$ is unique for a given t and x_0. S^t is assumed to be smooth (infinitely differentiable) in this dissertation for any t and $S^{(t+s)} = S^t \circ S^s$.

There are several types of ordinary differential equations that can be solved directly but most of them are not solvable, for example, the Lorenz system. In applications, the behavior of trajectories when $t \to \infty$ may be what one needs and it is meaningless to know the explicit expression of a single trajectory. Even though one may have an expression of every trajectory, the behavior of trajectories can be hard to be gleaned from the expression.

Dynamical systems theory was founded by Henri Poincaré and it investigates the behavior of trajectories instead of solving a differential equation system. A singular point of the vector field where $X(x) = 0$ determines the behavior of trajectories in a linear system:

it is a stable or unstable equilibrium state, or a saddle, or a saddle-node. In a nonlinear system, a singular point determines the local dynamics. Other invariant sets can exist in a nonlinear system, such as a periodic orbit, a torus or even a strange attractor. A simple nonlinear system may induce chaotic behavior.

1.1.1 Linear dynamical system

Equation (1.1) is a linear dynamical system if $X(x) = Ax$, assuming $X(0) = 0$ without loss of generality.

$$\frac{dx}{dt} = Ax. \tag{1.2}$$

The stability of the equilibrium O can be determined by the eigenvalues $(\lambda_1, \lambda_2, \ldots, \lambda_n)$ of the Jacobian matrix A. The eigenvalues are the roots of the characteristic equation

$$det|A - \lambda I| = 0 \tag{1.3}$$

where I is the identity matrix. Assume O is a structurally stable or hyperbolic equilibrium state; in other words, no eigenvalue is on the imaginary axis. If all the eigenvalues have negative real part, O is a stable equilibrium state and all trajectories converge to it when $t \to +\infty$; if all the eigenvalues have a positive real part, O is an unstable equilibrium state and all trajectories converge to O when $t \to -\infty$; if the real part of some of them are positive and the rest are negative, then O is a saddle or saddle-focus.

The general solution of the system (1.2) can be expressed as

$$x(t) = e^{At}x_0$$

where $e^{At} = I + At + A^2t^2/2! + \cdots + A^kt^k/k! + \cdots$. It can be expressed in terms of each eigenvalue of the Jacobian matrix A and its multiplicity. One can find the details in a dynamical systems textbook and this dissertation takes a 3D linear system as an example

(1.4) that will be used in chapter 3. The Jacobian matrix of System (1.4)

$$\dot{x} = -\rho x - \omega y, \quad \dot{y} = \omega x - \rho y, \quad \dot{z} = \lambda_3 z, \tag{1.4}$$

has a pair of complex eigenvalues $\lambda_{1,2} = -\rho \pm i\omega$ and a real eigenvalue λ_3. Its general solution is

$$x(t) = e^{-\rho t}[x_0 \cos(\omega t) - y_0 \sin(\omega t)],\ y(t) = e^{-\rho t}[y_0 \cos(\omega t) + x_0 \sin(\omega t)],\ z(t) = e^{\lambda_3 t} z_0. \tag{1.5}$$

Generally, let's consider a dynamical system with the spectrum of A is $\{\lambda_1, \ldots, \lambda_m, \sigma_1, \ldots, \sigma_n\}$ and $Re\lambda_m \leq \cdots \leq Re\lambda_{k+1} < Re\lambda_k = \cdots = Re\lambda_1 < 0 < Re\sigma_1 = \cdots = Re\sigma_l < Re\sigma_{l+1} \leq \cdots \leq Re\sigma_n$. Let $\mathcal{E}^s$ =span{eigenvectors of $\lambda_1, \ldots, \lambda_m$} and $\mathcal{E}^u$ =span{eigenvectors of $\sigma_1, \ldots, \sigma_n$}. Then $\mathcal{E}^s$ is the stable invariant subspace and trajectories initiated in $\mathcal{E}^s$ converge to O exponentially as $t \to +\infty$; $\mathcal{E}^u$ is the unstable invariant subspace and trajectories initiated in $\mathcal{E}^u$ converge to O exponentially as $t \to -\infty$. $\mathcal{E}^{sL}$ =span{eigenvectors of $\lambda_1, \ldots, \lambda_k$} is the leading stable subspace and $\mathcal{E}^{ss}$ =span{eigenvectors of $\lambda_{k+1}, \ldots, \lambda_m$} is the non-leading stable subspace. $\mathcal{E}^{uL}$ =span{eigenvectors of $\sigma_1, \ldots, \sigma_l$} is the leading unstable subspace and $\mathcal{E}^{uu}$ =span{eigenvectors of $\sigma_{l+1}, \ldots, \sigma_n$} is the non-leading unstable subspace. Define $\mathcal{E}^{sE} = \mathcal{E}^s \bigoplus \mathcal{E}^{uL}$ as the extended stable invariant subspace, $\mathcal{E}^{uE} = \mathcal{E}^u \bigoplus \mathcal{E}^{sL}$ as the extended unstable invariant subspace and $\mathcal{E}^L = \mathcal{E}^{sE} \bigcap \mathcal{E}^{uE}$ as the leading saddle subspace. All trajectories that are not in $\mathcal{E}^{ss}$ converge to the equilibrium state O tangentially to $\mathcal{E}^{uL}$ as $t \to +\infty$ and all trajectories that are not in $\mathcal{E}^{uu}$ converge to O tangentially to $\mathcal{E}^{sL}$ as $t \to -\infty$.

O is a saddle if the numbers in the spectrum are all real but it is called a saddle-focus if there are complex pairs in the spectrum. Moreover, saddle-focus $(2,1)$-type refers to a focus on $\mathcal{E}^s$ and a node on $\mathcal{E}^u$; saddle-focus $(1,2)$-type refers to a node on $\mathcal{E}^s$ and a focus on $\mathcal{E}^u$; saddle-focus $(2,2)$-type refers to focus on both $\mathcal{E}^s$ and $\mathcal{E}^u$.

1.1.2 Nonlinear dynamical system

Theorem 1.1.1 (Grobman-Hartman) *([1])For a structurally stable equilibrium state O in a non-linear dynamical system, there are neighborhoods of it, U_1 and U_2, such that the original non-linear system and the linearized system are topologically equivalent.*

The Grobman-Hartman theory guarantees that the non-linear system

$$\frac{dx}{dt} = Ax + f(x) \tag{1.6}$$

where $f(0) = 0$ and $f'(0) = 0$, are topologically equivalent to the linearized system (1.2).

W^s, W^u, W^{sL}, W^{uL}, W^{ss}, W^{uu}, W^{sE}, W^{uE} and W^L denote the stable manifold, the unstable manifold, the leading stable manifold, the leading unstable manifold, the non-leading stable manifold and the non-leading unstable manifold, the extended stable manifold, the extended unstable manifold and the leading saddle manifold of the equilibrium state O respectively; they are tangential at the point O to $\mathcal{E}^s$, $\mathcal{E}^u$, $\mathcal{E}^{sL}$, $\mathcal{E}^{uL}$, $\mathcal{E}^{ss}$, $\mathcal{E}^{uu}$, $\mathcal{E}^{sE}$, $\mathcal{E}^{uE}$ and $\mathcal{E}^L$ respectively.

1.1.3 Periodic orbit

For the autonomous system (1.1), a periodic orbit or a limit cycle refers to a solution $x = x(t)$ satisfying $x(t) = x(t + h)$, that is to say, the trajectory returns back to its initial point after time h. The smallest positive return time is called the period. Assume the period is h.

Unlike equilibrium states, it is usually hard to find a periodic orbit analytically. One of the solutions is to construct a Poincaré return map to study the behavior of trajectories near a structurally stable periodic orbit, say $\mathcal{L}$. Pick a point P^* on $\mathcal{L}$ and a small transversal cross plane Π at P^*. Without loss of generality, assume the point P^* is at the origin and $\Pi : x_{n+1} = 0$ (say $x \in \mathbb{R}^{n+1}$). Then due to the continuity, a trajectory that starts from a point $P \in \Pi$ sufficiently close to P^* returns to Π at a point, say $\bar{P}$, after a time $t(P)$. A Poincaré map $T : P \mapsto \bar{P}$ can be defined in this manner. Then $T(P^*) = P^*$, i.e., P^* is the

fixed point of the map T. Let $P_i = T^i P$. The behavior of trajectories near the periodic orbit $\mathcal{L}$ is fully determined by the behavior of the sequence $\{\cdots, P_{-1}, P, P_1, P_2, \cdots\}$. The Poincaré map T can be written in the form

$$\bar{x} = Bx + g(x)$$

where $g(0) = g'(0) = 0$. It is equivalent to the linearized form $\bar{x} = Bx$. The eigenvalues of the matrix are called multipliers of the periodic orbit or the fixed point P^* and they determine the dynamics of the trajectories near the periodic orbit $\mathcal{L}$. Assume the spectrum of the matrix B is $\{\lambda_1, \ldots, \lambda_n\}$. If $|\lambda_i| < 1$ $(1 \leq i \leq n)$, $P_i \to P^*$ exponentially as $i \to +\infty$ and therefore trajectories nearby converge to the periodic orbit $\mathcal{L}$ in forward time and thus $\mathcal{L}$ is a stable periodic orbit. If $|\lambda_i| > 1$ $(1 \leq i \leq n)$, $P_i \to P^*$ exponentially as $i \to -\infty$ and therefore trajectories nearby depart from the periodic orbit $\mathcal{L}$ in forward time and thus $\mathcal{L}$ is an unstable periodic orbit. If some of the eigenvalues, say $\lambda_1, \ldots, \lambda_k$, are inside the unit circle and the rest are outside the unit circle, the periodic orbit $\mathcal{L}$ is a saddle. The ones closest to the unit circle from the inside and the outside determine the leading stable and unstable subspaces. Let $\delta_s = sign \prod_{i=1}^{k} \lambda_i$ and $\delta_u = sign \prod_{i=k+1}^{n} \lambda_i$ and define $(k, \delta_s, n-k, \delta_u)$ as the topological type.

Theorem 1.1.2 *([1])Two structurally stable periodic orbits are locally topologically equivalent if and only if their topological types are the same.*

1.1.4 Bifurcations of dynamical systems

The concept of "bifurcation" was introduced by Poincaré to describe the phenomenon that one equilibrium state can decompose into multiple equilibrium sates when varying the parameters of a system. The modern theory of bifurcations in dynamical systems expresses the appearance of non-roughness or structural instability of a system. A bifurcation in a dynamical system suggests a qualitative change of the phase portrait when varying the parameters of the system. In a two dimensional case, bifurcations are the boundaries that

separate the regions of rough systems, in view of the fact that the set of rough systems are dense and open on a plane. The bifurcation theory in high-dimensional systems is not as well organized because structurally stable systems are not dense in the space of dynamical systems.

Definition 1.1.1 *System (1.1) in a closed and bounded region G is called a Morse-Smale system if it satisfies the following conditions: (1) Its non-wondering set consists of a finite number of orbits. (2) All periodic orbits and equilibrium states in G are structurally stable and any intersection of their stable and unstable invariant manifolds is transverse. ([1])*

A bifurcation occurs when a system loses its structural stability and therefore possesses one of the following in a Morse-Smale system:

(1) An equilibrium state that has at least one eigenvalue on the imaginary axis;

(2) A periodic orbit with a unit multiplier;

(3) A homoclinic orbit;

(4) A heteroclinic orbit.

Some of these above may lead the system out of the category of Morse-Smale, however. For example, a homoclinic loop of a saddle-focus in a 3D system may generate infinitely many periodic orbits. Assuming that the saddle-focus has three eigenvalues, $-\rho \pm i\omega$ and λ, and $\rho, \lambda > 0$, Shilnikov proved the following theorem by defining $\sigma = -\rho + \lambda$ as the saddle value and $\nu = \rho/\lambda$ as the saddle index.

Theorem 1.1.3 *([1])For a 3D system with a homoclinic orbit of a saddle-focus, if its saddle value $\sigma > 0$ or its saddle index $\nu < 1$ (Shilnikov condition), the neighborhood of the homoclinic orbit has infinitely many saddle periodic orbits. But if $\sigma < 0$ or $\nu > 1$, the neighborhood of the homoclinic orbit has a trivial structure and no other invariant exists.*

For a family of smooth systems $\dot{x} = X(x, \mu)$, where $\mu \in \mathbb{R}^m$, μ_0 is called a bifurcation parameter value if $\dot{x} = X(x, \mu_0)$ is a non-rough system. The set of all such parameter values is called a bifurcation set.

1.1.5 Homoclinic loop

Assuming that Q_1 and Q_2 are either equilibrium states or periodic orbits and $W^u_{Q_1}$ and $W^s_{Q_2}$ intersects at a point x_0, the trajectory of x_0 is called a heteroclinic orbit if Q_1 and Q_2 are different and it is called a homoclinic orbit if Q_1 and Q_2 are the same. In other words, the trajectory of x_0 is a heteroclinic orbit if $x(t, x_0) \to Q_1$ as $t \to -\infty$ and $x(t, x_0) \to Q_2$ as $t \to +\infty$; the trajectory of x_0 is a homoclinic orbit if $x(t, x_0) \to Q_1$ (or Q_2) as $t \to \infty$.

In a smooth 2D system (1.1), assume that $O(0, 0)$ is a saddle and the spectrum of its Jacobian matrix $\frac{\partial X(O)}{\partial x}$ is $\{\lambda_1, \lambda_2\}$, where $\lambda_1 > 0 > \lambda_2$. Then $W^s_O = O \bigcup \Gamma^-_1 \bigcup \Gamma^-_2$ and $W^u_O = O \bigcup \Gamma^+_1 \bigcup \Gamma^+_2$ in which $\Gamma^-_{1,2}$ denote the two stable separatrices of O and $\Gamma^+_{1,2}$ denote the two unstable separatrices of O. When $\Gamma^-_1 = \Gamma^+_1$, the system has a homoclinic orbit of the saddle O, denoted as Γ. Two cross sections Π_0 and Π_1 are chosen in Figure 1.1. A linear transformation can be applied to the system to straighten the stable and unstable manifold of the origin so that the local map T_0 is determined by the following standard linear system.

$$\dot{x} = \lambda_1 x + f(x, y), \quad \dot{y} = \lambda_2 y + g(x, y),$$

where $f(0, 0) = g(0, 0) = 0$ and $f'(0, 0) = g'(0, 0) = 0$. Then W^s_O tangents the y-axis at O and W^u_O tangents the x-axis at O. The cross sections can be taken as $\Pi_0 : y = d$ and $\Pi_1 : x = d$ where d is some small positive number. Let $T_0 : (x_0, d) \mapsto (d, y_0)$. Then it can be easily calculated that

$$y_0 = d^{1-\nu} x_0^\nu + o(x_0^\nu)$$

where $\nu = -\lambda_2/\lambda_1$ is the saddle index. The time of flight of the map T_1 is fast therefore it can be approximated by a linear transformation $T_1 : x_1 = Ay_0$ $(A > 0)$, knowing that $x_1 = 0$ when $y_0 = 0$. Therefore we have $T : x_1 = Ad^{1-\nu} x_0^\nu + o(x_0^\nu)$ as a Poincaré mapping on the cross section Π_0. $x_1 < x_0$ for a sufficiently small x_0 if $\nu > 1$; therefore, the homoclinic loop is one-side stable. If $\nu < 1$, $x_1 > x_0$ for a sufficiently small x_0; therefore, the homoclinic loop is one-side unstable.

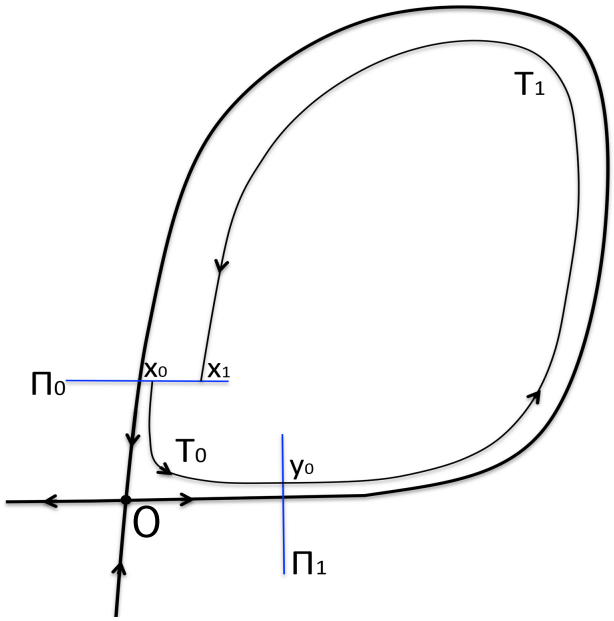

Figure (1.1) The right unstable separatrix of the origin O is also its stable separatrix and converges to O as $t \to +\infty$.Two cross sections Π_0 and Π_1 are chosen near the saddle O. The map $T_0 : \Pi_0 \mapsto \Pi_1$ is a local map and determined fully by the flow of the saddle. The map $T_1 : \Pi_1 \mapsto \Pi_0$ is determined by the global dynamics.

For a nearby system $\dot{x} = X_\mu(x)$, the parameter μ is defined as the shift of the map $T_1 : x_1 = Ay_0 + \mu$. Thus, the system has a homoclinic orbit when $\mu = 0$. Note the spectrum of the saddle as $\{\lambda_1(\mu), \lambda_2(\mu)\}$ and the saddle index $\nu_\mu = -\lambda_2(\mu)/\lambda_1(\mu)$.

Theorem 1.1.4 (Andronov and Leontovich) *([1])(1) If $\nu_0 < 1$, for $\mu < 0$ sufficiently small, there is a unique unstable periodic orbit that is getting close to the saddle when $\mu \to 0-$ and it becomes a homoclinic orbit when $\mu = 0$. There is no such periodic orbit when $\mu > 0$. (2) If $\nu_0 > 1$, for $\mu > 0$ sufficiently small, there is a unique stable periodic orbit that is getting close to the saddle when $\mu \to 0+$ and it becomes an homoclinic orbit when $\mu = 0$. There is no such periodic orbit when $\mu < 0$.*

The Poincaré mappings T on the cross section Π_0 when $\nu_0 < 1$ are plotted in Figure 1.2 with three cases, $\mu > 0$, $\mu = 0$ and $\mu < 0$. The fixed point on the diagonal line corresponds to a periodic orbit. Obviously, when $\mu < 0$, there is a fixed point on the diagonal line with

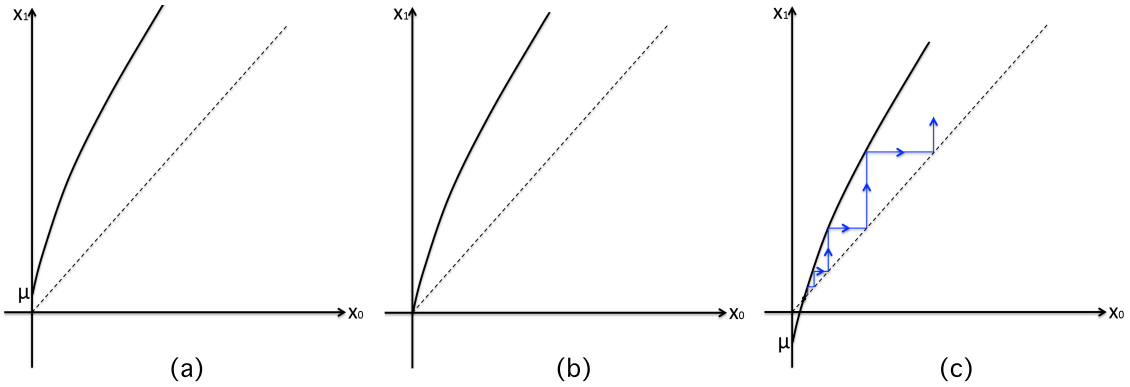

Figure (1.2) (a) $\mu > 0$. (b) $\mu = 0$. (c) $\mu < 0$.

a slope greater than one and therefore there is an unstable periodic orbit. When $\mu > 0$, however, there is no fixed point on the diagonal line and therefore there is no periodic orbit.

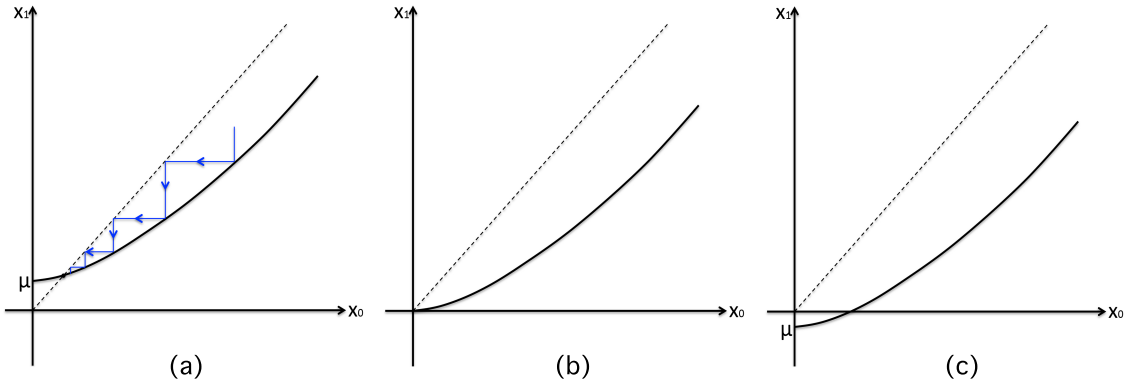

Figure (1.3) (a) $\mu > 0$. (b) $\mu = 0$. (c) $\mu < 0$.

The Poincaré mappings T when $\nu > 1$ are plotted in Figure 1.3. When $\mu > 0$, there is a fixed point on the diagonal line and its slope is less than one, therefore there is a stable periodic orbit. When $\mu < 0$, there is no fixed point on the diagonal line and thus there is no periodic orbit.

The results can be easily proved that it applies to the general case of a homoclinic orbit on a two-dimensional surface. When $A > 0$, a small neighborhood of the homoclinic orbit is homomorphic to a cylinder and the surface is orientable. In this general situation, A can be

less than zero. When $A < 0$, a small neighborhood of the homoclinic orbit is homomorphic to a Möbius band and the surface is non-orientable. The corresponding Poincaré mapping needs to be flipped as in Figure 1.4 and 1.5.

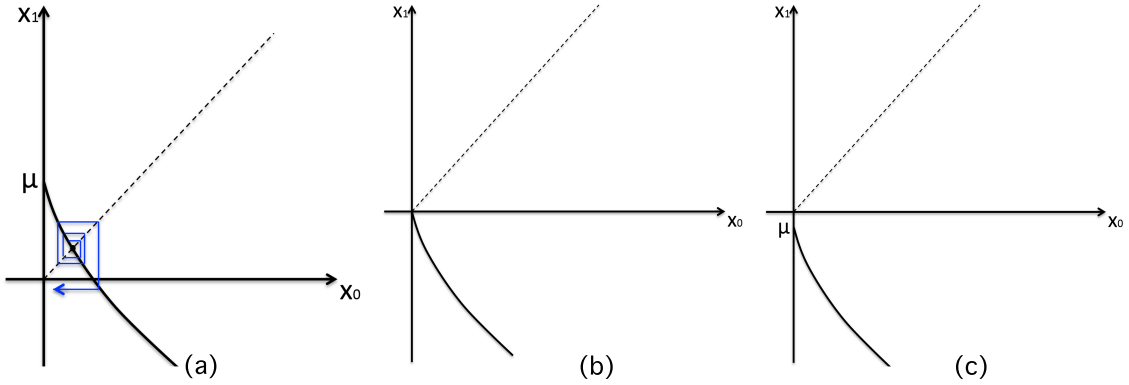

Figure (1.4) (a) $\mu > 0$. (b) $\mu = 0$. (c) $\mu < 0$.

As in Figure 1.4, when $\nu_0 < 1$ and $A < 0$, there is no periodic orbit if $\mu < 0$ and there is an unstable periodic orbit if $\mu > 0$. As in Figure 1.5, when $\nu_0 > 1$ and $A < 0$, there is no periodic orbit if $\mu < 0$ and there is an stable periodic orbit if $\mu > 0$.

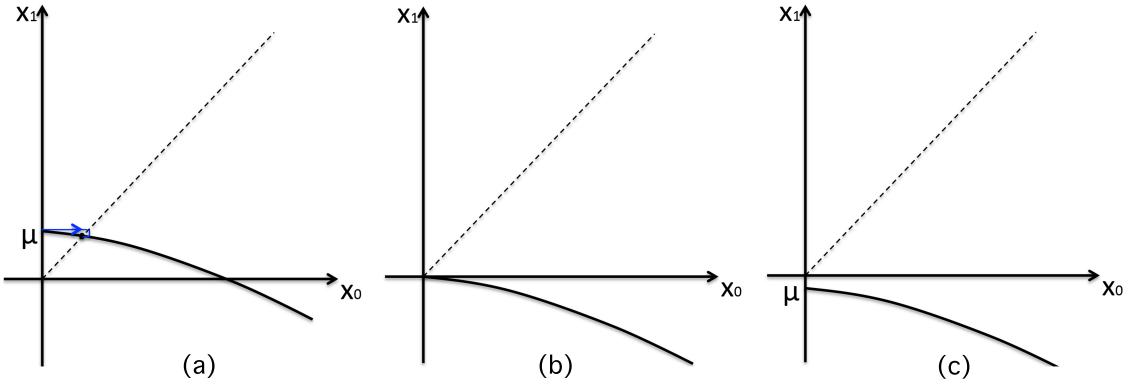

Figure (1.5) (a) $\mu > 0$. (b) $\mu = 0$. (c) $\mu < 0$.

In the case that the dimension is higher than two and $dim(W^u) = 1$, Shilnikov's theory provides the answer. Without loss of generality, assume that the saddle is at the origin. The

unstable eigenvalue is notated as γ and stable eigenvalues are notated as $\lambda_1, \lambda_2, \ldots, \lambda_n$ where λ_1 is the leading one.

Theorem 1.1.5 (Shilnikov) *([1])When the saddle value $\sigma < 0$ at the saddle, a single stable periodic orbit L is born from the homoclinic loop for $\mu > 0$. For $\mu \leq 0$, there is no periodic orbit in a small neighborhood U of the homoclinic loop. The trajectories of X_μ tend either to L (or, to the loop Γ at $\mu = 0$), or to O, or leave U as $t \to +\infty$.*

Under two non-degenerative conditions: (a) $\Gamma \not\subset W^{ss}$, (b) W^{uE} transverses W^s at the points of Γ, the following theorem holds if the leading unstable eigenvalue is simple and real.

Theorem 1.1.6 *([1])If a homoclinic loop Γ to a saddle with a positive saddle value satisfies non-degenerative conditions (a) and (b), then a single saddle periodic orbit $L(\mu)$ is born from the loop for $A\mu < 0$. The unstable manifold of $L(\mu)$ is two-dimensional and orientable when $A > 0$ (then there is only one positive multiplier greater than one), or non-orientable when $A < 0$ (then the multiplier greater than one in absolute value is negative). For $A\mu > 0$, there are no orbits (besides the equilibrium state O) staying in a small neighborhood U of Γ for all times. For $A\mu < 0$, almost all orbits leave U. The exceptions are O, L and one heteroclinic orbit which is α-limit to L and ω-limit to O.*

Theorem 1.1.7 (Shilnikov) *([1])Let a saddle-focus O have a homoclinic loop Γ which satisfies the non-degenerative conditions (a) and (b). Then, in an arbitrarily small neighborhood of Γ, there exist infinitely many saddle periodic orbits if the saddle value $\sigma > 0$ or equivalently the saddle index $\nu < 1$.*

There are three degenerate cases of such homoclinic loops.

(1) $\nu = 1$, $\Gamma \not\subset W^{ss}$ and $A \neq 0$.

(2) $A = 0$, $\Gamma \not\subset W^{ss}$, $1/2 < \nu < 1$ and $\nu_j > 1$ ($j = 2, \ldots, n$) where $\nu_j = |Re\lambda_j/\gamma|$.

(3) $\Gamma \subset W^{ss}$, W^{uE} is transverse with W^s along Γ, $\nu < 1$ and $\nu_j > 1$ ($j = 2, \ldots, n$).

Case (2) is called inclination-flip and case (3) is called orbit-flip.

1.2 Neural Network Modeling

Except for a few simple animals, all animals have a nervous system, including a brain and a spinal cord for higher level animals. Neurons are the core part of a neural system. Some invertebrate animals have big and visible neurons that are convenient for studying the function of a nerve system and most results on a neural system were taken from experiments on those simple neural systems. Neurons can be divided into three main types: sensory neurons, motor neurons, and interneurons, according to their functions and responsibilities within the neural system. Sensory neurons respond to stimuli passed from sensory organs such as touch, sight, and sound. Motor neurons receive signals from the neural system and control muscle movements. Interneurons transfer information between neurons in a neural system. A typical neuron has three parts, the cell body (soma), axon and dendrites. In general, an axon sends signals and dendrites receive signals from other neurons or their own neuron. Electrical and chemical signals pass among neurons in a neuron network through synapses. Across the membrane of a neuron, voltage gradients are generated by the concentration difference of ions, mainly sodium, potassium and calcium. Neurons can be excited electrically. When the membrane potential changes by a sufficient amount, an action potential can be triggered and it activates other neurons by the synaptic connections. A group of neurons that interact with each other in such a manner is called a neural network. Rather than study the entire neural system, scientists have studied central pattern generators (CPGs) because CPGs are relatively small and autonomous neural networks. CPGs generate rhythmic behaviors without inputs from motor or sensory neurons and they commonly involve half center oscillators (HCOs). An HCO is a network of two neurons that have no rhythmic behavior individually but generate rhythmic outcomes after reciprocally coupled. The rhythmic outcomes can be firing anti-phase, or in any other relative phase, or even synchrony. Moreover, HCOs can function in different mechanisms, synaptic release, post-inhibitory rebound and escape.

Release cells are intrinsic bursters individually. Synaptic coupling can lock a release cell on the quiescent stage and the cell is released when the coupling is released in each

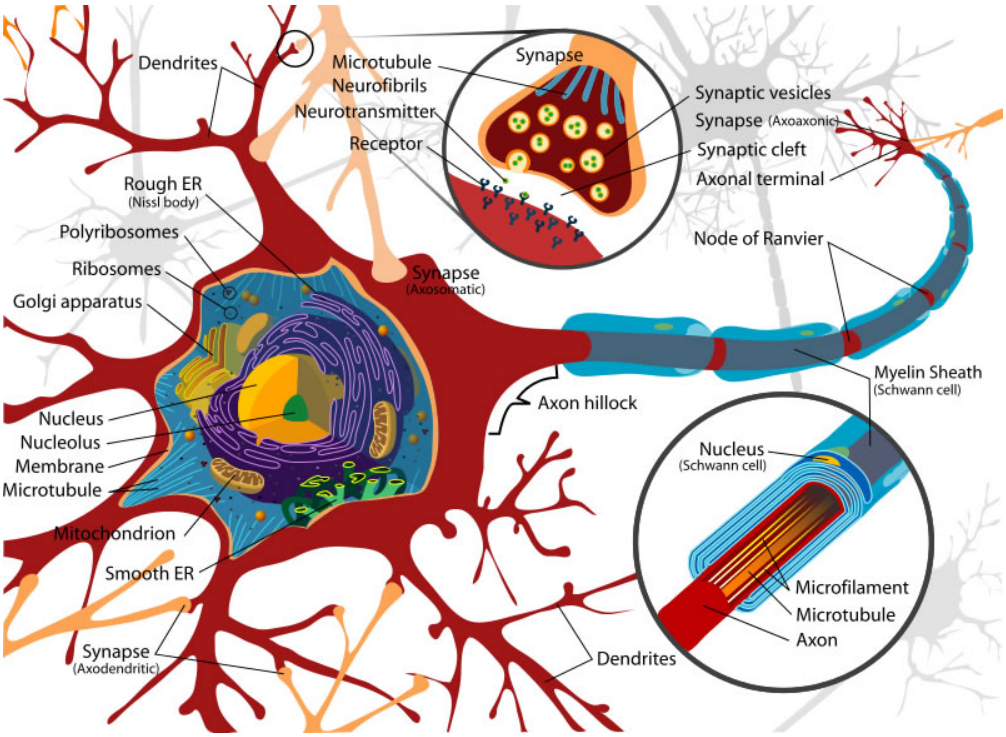

Figure (1.6) A sketch of the structure of a neuron and how a neuron connects and passes information to another neuron. https://en.wikipedia.org/wiki/Neuron

cycled time-span. A post-inhibitory rebound cell is intrinsically quiescent. An inhibitory connection from the post cell excites the cell and the pre-cell starts to burst. An escape cell is intrinsically tonic spiking. The pre-cell escapes from the hyperpolarized tonic spiking stage and starts bursting with a synaptic coupling from a post-cell.

In the meantime, a chemical synaptic connection can be inhibitory or excitatory. An inhibitory post-synaptic potential (IPSP) inhibits the pre-cell and make it less likely to fire an action potential, while an excitatory post-synaptic potential (EPSP) excites the pre-cell and makes it more likely to fire an action potential. In this dissertation, inhibition is assumed to extend the depolarization quiescent stage of a cell and shorten the hyperpolarization spiking stage of the cell.

Many mathematical models that simulate a neuron have been developed. The most well-known and most important one is the Hodgkin-Huxley model.

1.2.1 The Hodgkin-Huxley model (Wikipedia)

Hodgkin-Huxley types of models are biologically relevant models that are developed based on ionic mechanisms of action potentials generated and propagated by neurons and all parameters have their biological or physical meanings.

A typical Hodgkin-Huxley model treats the bi-layer membrane as a capacity (C). The electrical conductance through voltage-gated ion channels is represented as g_{ion}. The reversal potentials for ion channels are denoted by E_{ion}. V represents the membrane potential and I represents the current per unit area. Then a typical Hodgkin-Huxley model is

$$I = C\frac{dV}{dt} + g_K(V - E_K) + g_{Na}(V - E_{Na}) + g_l(V - E_l)$$

where g_K, g_{Na} and g_l are potassium, sodium and leaking conductance respectively and E_K, E_{Na} and E_l are potassium, sodium and leaking reversal potentials respectively.

For voltage-gated ion channels, conductance g_{ion} is voltage and gating variables dependent. They are modeled as following.

$$g_K = \hat{g}_K n^4$$

$$g_{Na} = \hat{g}_{Na} m^3 h$$

$$\frac{dh}{dt} = \alpha_h(V)(1 - h) - \beta_h(V)h$$

$$\frac{dm}{dt} = \alpha_m(V)(1 - m) - \beta_m(V)m$$

$$\frac{dn}{dt} = \alpha_n(V)(1 - n) - \beta_n(V)n$$

where α_i and β_i ($i \in \{h, m, n\}$) are rate constants for the corresponding ion channel. They can be expressed as

$$\alpha_i(V) = B_\infty^{(i)}(V)/\tau_i, \quad \beta_i(V) = (1 - B_\infty^{(i)}(V))/\tau_i$$

where $B_{\infty}^{(i)}(V) = \frac{M_i(V-N_i)}{\exp(\frac{V-N_i}{K_i})-L_i}$ is a Boltzmann equation.

1.2.2 The Theta model (Wikipedia)

Some phenomenon mathematical models simulate the superficial results only without considering the biological meanings. The theta model or Ermentrout-Kopell canonical model is one of them. The phase space of the model is a unit circle and the general expression of the model is

$$\frac{d\theta}{dt} = 1 - \cos\theta + (1 + \cos\theta)I(t)$$

where $I(t)$ is the input and $\theta \in [0, 2\pi)$. A neuron is considered experiencing a spike every time when $\theta = \pi$. When $I(t) > 0$, $\frac{d\theta}{dt} > 0$ and the neuron is doing tonic spiking individually. When $I(t) = 0$, $\theta = 0$ is the only saddle-node equilibrium state and the neuron is an intrinsic silent cell. When $I(t) < 0$, the saddle-node bifurcates into one stable equilibrium state and one unstable equilibrium state.

1.2.3 The FitzHugh-Nagumo model (Wikipedia)

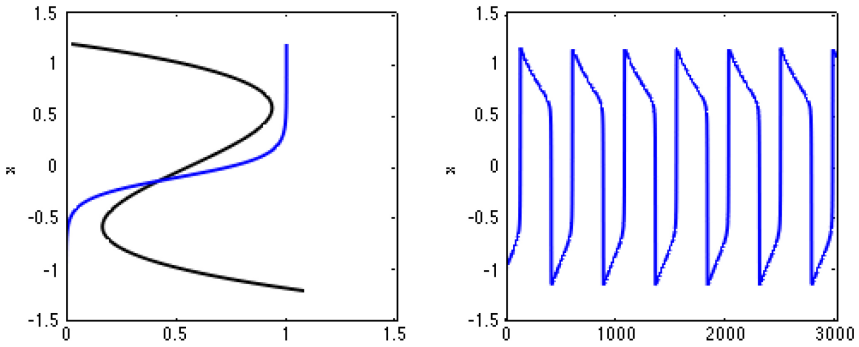

Figure (1.7) The slow nullcline crosses the Z-shape fast nullcline at the middle branch, an oscillation is generated.

The FitzHugh-Nagumo model is an intermediate model. It simulates similar results with the Hodgkin-Huxley model but it has much less complexity. In the meantime, it maintains

crucial biological meanings for its parameter values.

$$\frac{dv}{dt} = m(v - v^3) - w + I_{ext}, \quad \frac{dw}{dt} = \epsilon(av + b - w)$$

where ϵ is relatively small and then the system becomes a slow-fast system. The fast nullcline $m(v - v^3) - w + I_{ext} = 0$ is a cubic shape and the slow nullcline $av + b - w = 0$ is a line. The slow nullcline also can be modeled as a Boltzmann function.

$$\frac{dv}{dt} = m(v - v^3) - w + I_{ext}, \quad \frac{dw}{dt} = \epsilon(\frac{1}{1 + e^{-k(v-a)}} - w)$$

PART 2

SYMBOLIC QUEST INTO HOMOCLINIC CHAOS

The iconic shape of the Lorenz attractor has long been an emblem of Chaos Theory as a new paradigm in nonlinear sciences. This emblem has been reprinted innumerable times on posters announcing popular lectures and professional meetings with cross-disciplinary scopes, and/or with particular emphasis on dynamical systems and bifurcations. The concept of deterministic chaos illustrated by snapshots of the Lorenz attractor has been introduced in all modern textbooks on nonlinear dynamics. Nowadays, its butterfly-shaped image is stereotypically associated with images of deterministic chaos as a whole.

The library of publications on systems with the Lorenz attractor has considerably grown over a half century, since the celebrated paper [2] came out introducing a basic system of three ordinary differential equations with highly unordinary trajectory dynamics.

The ideas of this research trend are deeply rooted in the pioneering studies led by L.P. Shilnikov in the city of Gorky, USSR [4; 5; 6; 3]. He was a creator of the theory of homoclinic bifurcation and a founder of the theory of strange attractors. His extensive knowledge of global bifurcations helped to turn Chaos theory into a mathematical marvel [7; 8; 9; 10; 11; 12; 13; 14]. His contributions to the theory are pivotal and include the identification and description of the structures of and bifurcation routes to spiral and screw-like strange attractors emerging through bifurcations of the famous Shilnikov saddle-focus [15; 16; 17], which have been found in a broad range of applications from nonlinear optics to biology and finance. He proposed scenarios of the onset of chaos through a torus breakdown [18; 19], the onset of complex dynamics caused by structurally unstable homoclinics of saddle periodic orbits [20; 21], as well as that of shift dynamics after the disappearance of a Shilnikov saddle-node, also called a saddle-saddle [22; 23]. Concerning the Lorenz attractor, he pointed out the conditions sufficient for a system to possess the Lorenz attractor [6]. These conditions

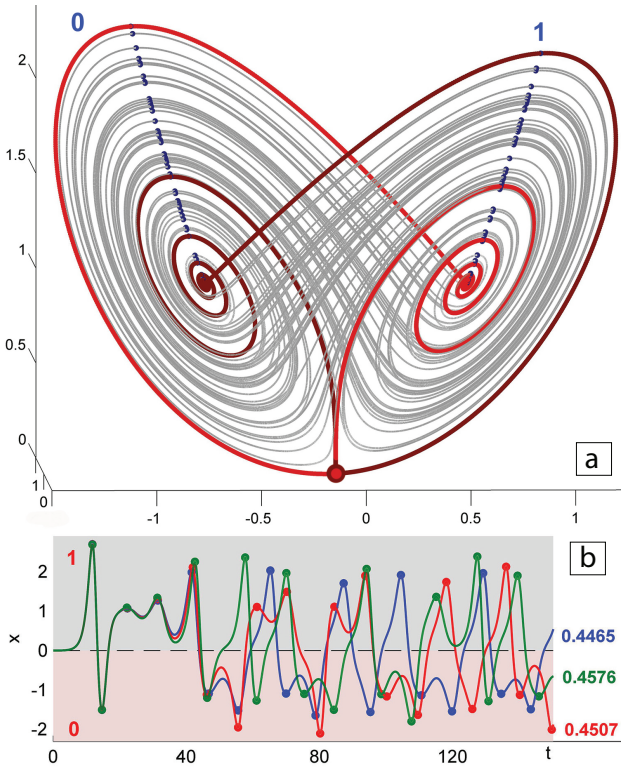

Figure (2.1) (a) The (x, z)-projection of a heteroclinic connection (red color) between the saddle (at the origin) and the saddle-foci overlaid with the chaotic attractor (grey color) in the background in the phase space projection on the SM-model at the primary T-point. The flip-flopping of the "right" separatrix defines the binary entries, {1, 0}, of kneading sequences, depending on whether it turns around the right or left saddle-focus, resp. (b) Sensitivity of time progressions of the separatrix results in kneading sequences with the same initial episode $\{1, 0, 1, 1, 1, 0 \dots\}$ due to small variations of the λ-parameter.

were used to verify and to determine the existence regions of the Lorenz attractor, and to present computer assisted proofs of chaotic dynamics without stable orbits and homoclinic tangencies in the canonical Lorenz model [24; 25; 26].

In his PhD thesis L.P. Shilnikov proved the generalizations of homoclinic bifurcations of a saddle and a saddle-node, which lead to the emergence of a stable periodic orbit in $\mathbb{R}^n$, $n \geq 3$ [27; 28]. Having defended it, his interest wholly switched from systems with trivial dynamics and their spatial generalizations to a brand new challenge that he had set for himself — high-dimensional systems with complex, structurally unstable dynamics – the precursors of deterministic chaos. In 1968, L.P. Shilnikov published a paper proving the existence and

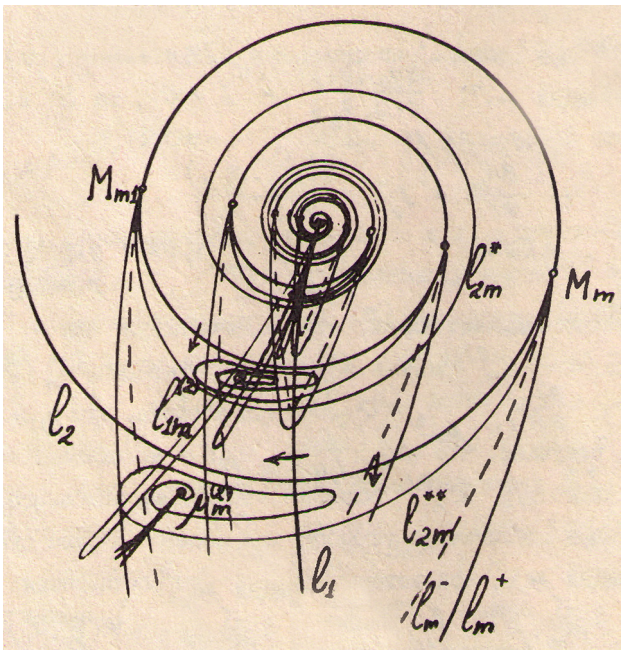

Figure (2.2) Sketch of a partial bifurcation unfolding of a Bykov T-point (from [3]) corresponding to a codimension-two heteroclinic connection between a saddle of the (2,1)-type and a saddle-focus of the (1,2)-type. It features the characteristic spirals corresponding to homoclinic bifurcations of the saddle. Turning points (labeled by M's) on the spiral are codimension-two points of inclination-switch bifurcations giving rise to stable periodic orbits through saddle-node and period-doubling bifurcations (l_m-curves) and subsequent spiral structures of smaller scales between spiral's scrolls.

uniqueness of a saddle periodic orbit emerging through a homoclinic bifurcation of a saddle in $\mathbb{R}^3$ and higher dimensions [29]. In this paper he introduced the conditions giving rise to the novel bifurcations of codimension-two termed as orbit-flip and inclination-switch (Fig. 2.3). [1] This result (as well as ones above, treated as scientific folklore, i.e. without acknowledging his original papers), along with the widely-known Shilnikov saddle-focus [15; 16; 17] and a less known Shilnikov saddle-node [22; 23], constituted his thesis for a degree of Doctor of Science. Mid 1970's and early 80's were just the beginning of the new – his era of Poincaré's qualitative theory of differential equations and bifurcations with the emphasis on complex dynamics, the field that is known today as the advanced dynamical systems theory.

In this dissertation we would like to re-discover the wonder of systems with Lorenz-like attractors, which are viewed not only through the prism of the elegant complexity of

[1] Upon fulfillment of certain conditions these bifurcations can lead to the onset of complex dynamics in Z_2-symmetric systems, specifically, to the appearance of the Lorenz attractor [9].

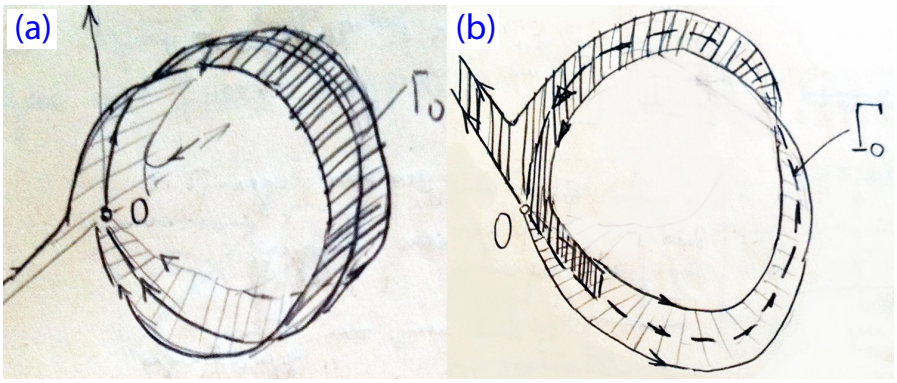

Figure (2.3) (a) to a non-orientable (b) separatrix loop Γ_0 (the median line of a Möbius band) of a saddle O in $\mathbb{R}^3$.

the trajectories' behavior in the phase space, but also by disclosing a plethora of generic fractal-hierarchical organizations of the parameter space. This work is aimed at illustrating the richness of homoclinic bifurcations underlying the magic metamorphoses of chaos in the exemplary Shimizu-Morioka models and like systems. It is an extension of the ideas introduced in the earlier paper "Kneadings, Symbolic Dynamics and Painting Lorenz Chaos" by R. Barrio, A. Shilnikov and L. Shilnikov [30]. The computational approaches that we have developed for studying systems with complex dynamics capitalize on the key property of deterministic chaos – the sensitive dependence of solutions in such a system on perturbations like variations of bifurcation parameters. In particular, for the Lorenz-type attractors, chaotic dynamics are characterized by unpredictable flip-flop switching between the two spatial wings of the strange attractor, separated by a saddle singularity at the origin.

2.1 The Shimizu-Morioka model

The three-parameter extension of the Shimizu-Morioka (SM) model [31; 32; 33; 34] is given by

$$\dot{x} = y, \quad \dot{y} = x - \lambda y - xz - Bx^3, \quad \dot{z} = -\alpha(z + x^2); \tag{2.1}$$

here, $\{\alpha,\ \beta > 0\}$ are the primary bifurcation parameters. Eqs. (2.1) are known to be a normal form for triple-degenerate equilibria and periodic orbits in a Z_2-symmetric central manifold

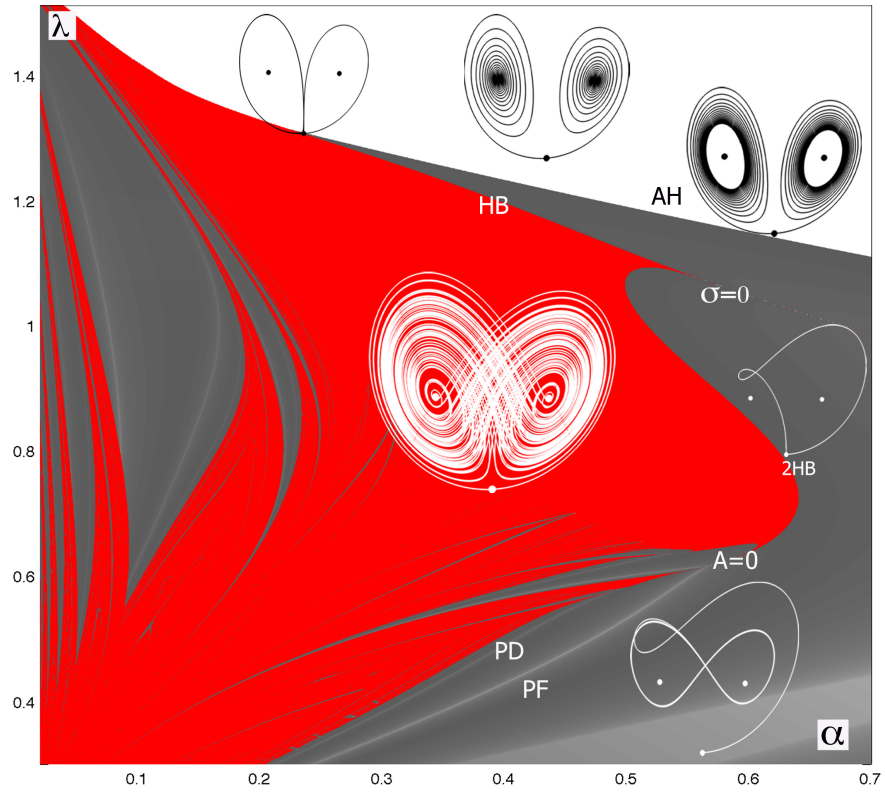

Figure (2.4) The white, grey and red colors correspond to the existence regions of stable equilibria where the largest LE, $L_1 < 0$, stable periodic orbits where $L_1 = 0$, and chaotic dynamics where $L_1 > 0$. White lines in the grey regions are associated with period-doubling (PD) and pitchfork (PF) bifurcations at which the second LE, L_2, also reaches zero from below. The borderline between the white and grey regions corresponds to a supercritical Andronov-Hopf bifurcation. Notice a fractal border between regions of chaotic and simple dynamics.

[35; 36]. Moreover, the Lorenz model can be reduced to Eqs. (2.1) with proper parameter and coordinate substitutions [37]. We will start with the classical case $B = 0$, and later use its variation to unfold globally the bifurcation structures. Like the Lorenz equation, this symmetric model, i.e. $(x, y, z) \leftrightarrow (-x, -y, z)$, has three equilibrium states: two stable-foci at $(\pm\sqrt{\alpha}, 0, 1)$ that become saddle-foci through an Andronov-Hopf bifurcation, which is supercritical, not sub-, in the given case. The origin is a saddle of (2,1)-type, i.e. with a couple of 1D outgoing separatrices. The type of the saddle is determined by the eigenvalues, $s_3 < s_2 < 0 < s_1$, of the linearization matrix at the origin. The saddle index, being a ratio of the leading eigenvalues $\nu = s_1/|s_2|$, determines the stability and the number of periodic orbits

bifurcating from a homoclinic loop. If $\nu > 1$, the only stable periodic orbit can bifurcate from a homoclinic loop [27; 28]. Though cases with $\nu < 1$ are more delicate, generally there is a single saddle orbit bifurcating from a homoclinic loop unless the outgoing separatrix twists along the loop, or returns to the saddle from the direction due to s_3, instead of leading s_2. These bifurcations are referred to as orbit-flip and inclination-switch in modern literature. A saddle with $\nu = 1$ is called resonant; this homoclinic bifurcation gives rise to a saddle-node periodic orbit. These three primary codimension-two bifurcations were discovered by L.P. Shilnikov in the 1960s [29; 1]. Either bifurcation of the homoclinic butterfly made simultaneously from two homoclinic loops in a $\mathbb{Z}_2$-system can give rise to the onset of the Lorenz attractor [9; 32; 38; 39; 40; 35; 41]. Of special interest here are codimension-two homoclinic bifurcations of two kinds: the resonant saddle, giving rise to the appearance of the Lorenz attractor and shaping its existence region in the parameter space together with the inclination-switch bifurcations terminating the Lorenz attractor in the SM-model. As we show below, there is another type of codimension-two points, called Bykov T-points, which are typical for Lorenz like systems [3; 42; 43]. Such a point corresponds to a closed heteroclinic connection between three saddle equilibria (Fig. 2.1a) in Eqs. (2.1): the saddle at the origin and two symmetric saddle-foci of the (1,2) type. Such points turn out to cause the occurrence of self-similar, fractal structures in the parameter region corresponding to chaotic dynamics in the known systems with the Lorenz attractor [30; 44; 45].

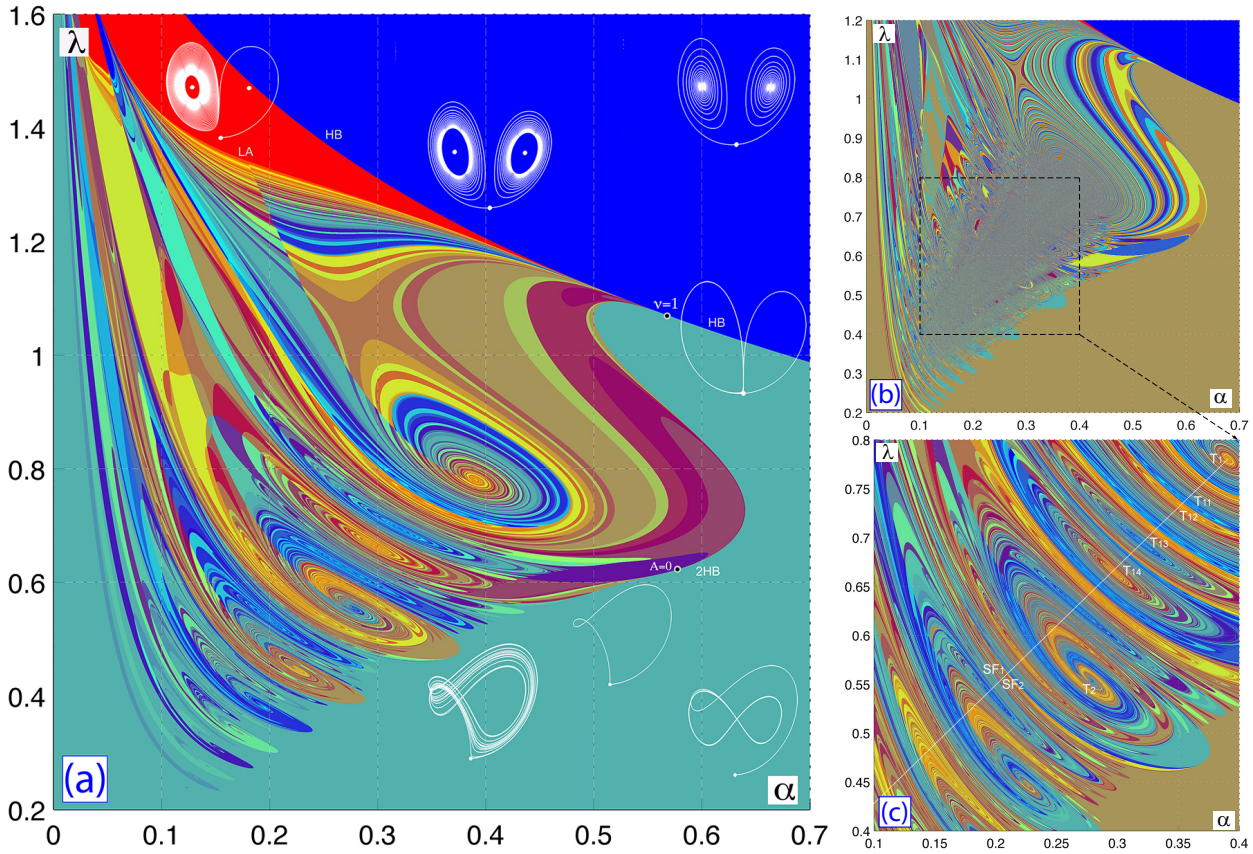

Figure (2.5) (a) (α, λ)-sweep of the SM model using the $\{5-15\}$-kneading range. Solid-color regions, associated with constant values of the kneading invariant, correspond to simple dynamics dominated by stable equilibria (blue and red) or stable periodic orbits (light blue). The borderline between blue and red/light blue region corresponds to the bifurcation curve, HB, of the homoclinic butterfly. The merger point corresponding to a resonant saddle of codimension-two gives rise to loci of bifurcation curves bounding and foliating the region of the Lorenz attractor. This region contains a variety of swirls of various scales centered around Bykov T-points for heteroclinic connections as well as the saddles separating them. The line, 2HB, represents a bifurcation curve of a double-pulsed [10] homoclinic loop with codimension-two inclination-switch point, A=0, on it. (b) Note saddles bounding codimension-two points in the diagram. High-resolution sweep of $\{12-22\}$-kneading range revealing fine foliation of the chaos region by homoclinic curves before the primary T-point at $(0.3903, 0.7805)$. Complex organization of multi-fractal swirls only appears noisy due to superabundant color variations in the given range. (c) Magnification depicting a plethora of embedded homoclinic swirls around T-points of various scales.

Figure 2.4 presents a Lyapunov exponent (LE) based sweep of the parameter space of the model with its attractors superimposed in the color-coded regions. The regions are painted as follows: white, grey and red corresponding to stable equilibrium states, periodic orbits and chaotic dynamics, respectively, in the model. The borderline between the first two should be interpreted as an Andronov-Hopf bifurcation giving rise to stable orbits as the parameter λ is decreased. The red region of chaos has sharp borders too, including a cusp-shaped "beak" with a tip corresponding to a homoclinic butterfly bifurcation of a resonant saddle with the saddle index $\nu = 1$ [32; 33]. The existence of the homoclinic butterfly in the SM-model was proven in [41]. Last but not least, we note multiple stability islands with stable periodic obits that occur within the chaotic red region, or cut it through from outside. In what follows we will elaborate, step by step, on the origin and arrangements of global bifurcations organizing the region of chaotic dynamics that only looks homogeneously solid in the LE-sweep(s).

2.1.1 Bykov T-points

Let us first introduce the principle organization for the bifurcation unfolding, sketched in Fig. 2.2, of a Bykov T-point corresponding to a closed heteroclinic connection between a saddle-focus and a saddle [3]. Its characteristic feature is a bifurcation curve spiraling onto the T-point. This curve corresponds to a homoclinic loop of the saddle such that the number of turns of the separatrix around the saddle-focus increases by one with each turn of the spiral approaching to the T-point. The line, l_1, originating from the T-point corresponds to homoclinics of the saddle-focus satisfying the Shilnikov condition [15; 17; 46], and hence leading to the existence of a denumerable set of saddle periodic orbits nearby [16]. Turning points (labeled by M's) on the primary spiral correspond to inclination-switch homoclinic bifurcations of the saddle [35; 1]. Each such homoclinic bifurcation point gives rise to the occurrence of saddle-node and period-doubling bifurcations of periodic orbits of the same symbolic representation. The central T-point gives rise to countably many subsequent T-points with similar bifurcation structures on smaller scales in the parameter plane. In

addition to the indicated curves in the unfolding of a generic T-point, the unfolding of a T-point in a $\mathbb{Z}_2$-symmetric system has other bifurcation curves, for example, corresponding to heteroclinic connections between both saddle-foci [3; 42; 43].

2.2 Symbolic description via kneadings

A hallmark of a Lorenz-like system is a strange attractor in the emblematic butterfly shape (Fig. 2.1a). The eyes of the butterfly wings demarcate the location of stable foci or saddle-foci. The strange attractor of the Lorenz type is structurally unstable [47; 6] as the separatrices of the saddle at the origin bifurcate constantly as the parameters are varied. These separatrices are the primary cause of structural and dynamic instability of chaos in the Lorenz equations and similar models. We say that the Lorenz attractor undergoes a homoclinic bifurcation when either separatrix of the saddle changes a flip-flop pattern of switching between the butterfly wings centered around the saddle-foci. At such a bifurcation, the separatrices come back to the saddle, thereby causing a homoclinic explosion in phase space [5; 48]. The time progression of either separatrix of the origin can be described symbolically and categorized in terms of the number of turns around two symmetric saddle-foci in the 3D phase space (Fig. 2.1a). Alternatively, the problem can be reduced to the time progression of the x-coordinate of the separatrix (Fig. 2.1b). In symbolic terms the progression of the separatrix can be described through a binary (e.g. $1, 0$) alphabet *per se*. Namely, each turn of the separatrix around the right or left saddle-focus, is associated with either 1 or 0, respectively. For example, the time series shown in Fig. 2.1b generates the kneading sequences starting with $\{1, 0, 1, 1, 1, 0 \dots\}$ at close parameter values. Thus, to differentiate between complex dynamics near a point of interest, one may want to skip an initial episode of kneading sequences to focus on their tails. Clearly, the sequences corresponding to chaotic dynamics will fluctuate unpredictably as the parameters vary.

The core of the computational toolkit is the binary $\{0, 1\}$ representation of a single solution - the outgoing separatrix of the saddle as it fills out the two spatiality symmetric wings of the Lorenz attractor at different parameter values.

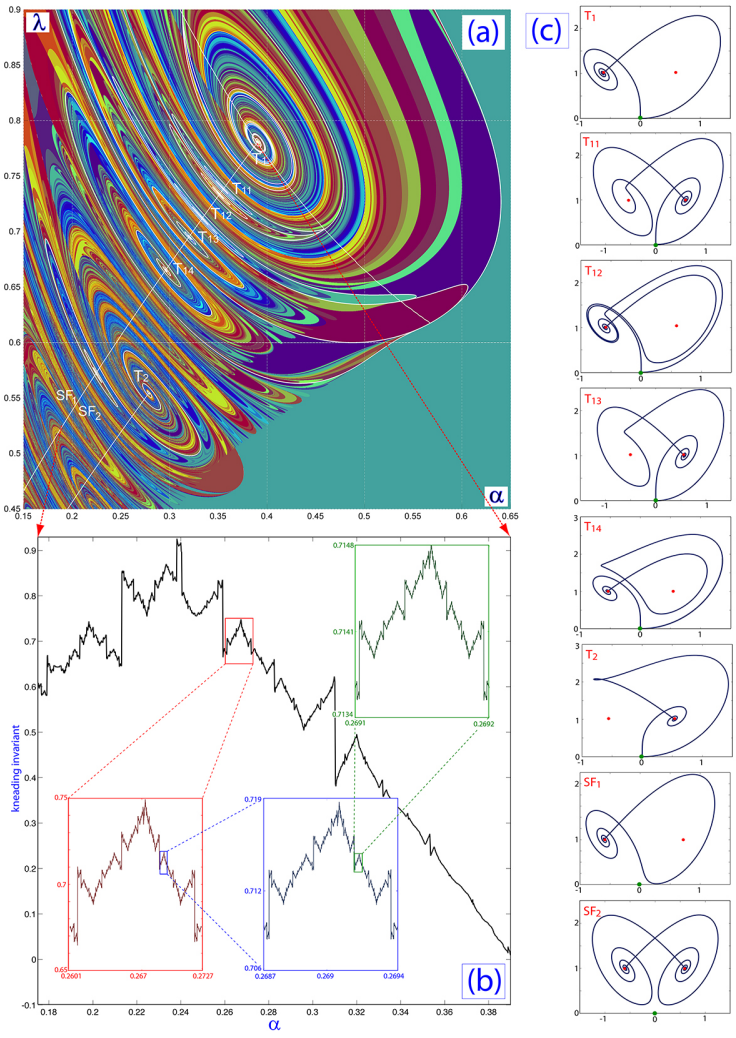

Figure (2.6) (a) Bi-parametric sweep of $\{6-20\}$-kneading range revealing fractal structures of homoclinic bifurcation swirls parented by the primary T-point, $\mathrm{T}_1(0.3903, 0.7805)$ with superimposed white bifurcations curves of separatrix loops obtained by the parameter continuation. Compare its self-similar structure to Bykov's unfolding in Fig. 2.2. (b) Self-similarity in the kneading dependence along the T-point pathway secluded between the curves SF_1 and SF_2 standing for homoclinic and heteroclinic connections of the saddle-foci. Critical and discontinuity points correspond to T-points and homoclinic bifurcations of the saddles shown in the side panels. (c) Various heteroclinic and homoclinic connections corresponding to the bifurcations selected in the bi-parametric sweeps shown in Fig. 2.5 and in the left panel: T_1 — the primary T-point of $\{1, 0^\infty\}$-type; SF_1 and SF_2 — homoclinic and heteroclinic saddle-foci; T_{1k}, $k = 1, 2\ldots$ parented by T_1 and nested between SF_1 and SF_2; T_2 — secondary T-point of $\{1, 0, 1^\infty\}$-type and its subsidiaries.

Such patterns can persist or change with variations of the parameters of the system. Realistically, and numerically, we can assess and differentiate between only appropriately long episodes of patterns, initial or intermediate, due to resolution limits. A positive quantity, called the kneading [49], bearing information about the pattern, allows one to quantify the dynamics of the system. By sweeping bi-parametrically, we create a map of the kneadings. Knowing the range of the kneading, we color-map the dynamics of the system in question onto the parameter plane. Whenever particular kneading quantity persists with variations of control parameters, then the flip-flop pattern does not change, thus indicating that dynamics can be robust (structurally stable) and simple. The straight forward application of this approach nevertheless fails to detect bifurcations, such as period-doubling and pitch-fork of periodic orbits. While this can still be remedied, these bifurcations were not a prime focus of this study elaborating on homoclinic bifurcations and how they can transform the Lorenz attractor.

In the parameter region of the Lorenz attractor, the flip-flop patterns change constantly and unpredictably. Nevertheless, a kneading value remains the same along a level curve. Such a curve corresponds to a homoclinic bifurcation of two separatrix loops of some configuration symbolically and uniquely described by the binary alphabet. No such bifurcation curves may cross or merge unless at a singular point corresponding to some homo- or heteroclinic bifurcation of codimension-two in the parameter plane of the model. As such, by foliating the parameter plane with such multi-colored lines, one can reveal the bifurcation structures and identify organizing centers – the singular points.

The kneading invariant was originally introduced to uniquely quantify the complex dynamics described by two symbols in a system, such as, for example, 1D logistic or skew-tent maps with increasing and decreasing branches separated by a critical point. Such maps emerge in a large number of dissipative systems including ones with Lorenz-like attractors. Moreover such systems can be topologically conjugated if they bear the same kneading invariant [50; 51; 52]. Without finding 1D maps, a kneading sequence $\{\kappa_n\}$ can be directly generated by time progressions of, say, the right separatrix, Γ^+, of the saddle, using the

following rule:

$$\kappa_n = \begin{cases} 1, & \text{when} \quad \Gamma^+ \text{ turns around } O_{\text{right}}, \\ 0, & \text{when} \quad \Gamma^+ \text{ turns around } O_{\text{left}}. \end{cases} \tag{2.2}$$

The kneading invariant is defined in the form of a formal power series

$$K(q, \mu) = \sum_{n=0}^{\infty} \kappa_n \, q^n, \tag{2.3}$$

convergent for $0 < q < 1$. The kneading sequence $\{\kappa_n\}$ comprised of only 1's corresponds to the right separatrix, Γ^+ converging to an equilibrium state or an orbit with $x(t) > 0$. The corresponding kneading invariant is maximized at $\{K_{\max}(q)\} = 1/(1-q)$. When the separatrix converges to an ω-limit set with $x(t) < 0$, then the kneading sequence begins with the very first 1 followed only by 0s. Skipping the very first "1", yields the range, $[0,\, q/(1-q)]$, of the kneading invariant values; at $q = 1/2$ it is $[0,\, 1]$. For each model, one has to figure an optimal value of q: setting it too small makes the convergence too fast so that the tail of the series would have little significance and hence would not differentiate fine dynamics of the system on longer time scales. Note that $q = 1/2$ is the largest value that guarantees the one-to-one correspondence between the time progression of the separatrix and the value of kneading invariant, K.

Given the range and the length of the kneading sequence, a colormap of a preset resolution is defined to provide the conversion of a numeric value of the kneading invariant into a unique color. In this study, the colormap includes 100 different colors chosen so that any two close kneadings are represented by contrasting hues. Specifically, the colormap is given by a 100×3 matrix, the columns of which correspond to [RGB] values standing for the red, green, and blue colors represented by $\{100\}$, $\{010\}$ and $\{001\}$, respectively. The R-column of the colormap matrix has entries linearly decreasing from 1.0 to 0.0, the B-column has entries linearly increasing from 0.0 to 1.0, while any entry of the G-column alternates between 0 and 1 to produce color diversities. So, by construction, the blue color represents kneading invariants in the $\{0.99,\, 1.0\}$ range, the red color on the opposite side of the spectrum corre-

sponds to kneading invariants in the $\{0,\ 0.01\}$ range, and all other 98 colors fill the spectrum in between. A borderline between two colors corresponds to a homoclinic bifurcation of the saddle through which the kneading invariant changes its value. Due to resolution, the colormap is sensitive only to variations of the first two decimals of the kneading value. For this reason we only consider kneading sequences of length 10, with the contribution of the tail about $0.5^{11}/(1-0.5) = 0.5^{10} \approx 10^{-3}$ to the kneading value. To obtain finer structures of the bifurcation diagram foliated by longer homoclinic loops, one should skip a number of initial kneadings to keep episodes 10 entries long or so: $\{3-12\}$, $\{22-31\}$, and so forth. Such a sweep can reveal up to 2^{10} distinct homoclinic bifurcations. A word of caution: having information in excess, i.e., overwhelmingly many bifurcation curves of random colors, will make the bifurcation diagram look noisy on the large scale even though the number of mesh points is large enough. Producing clear and informative diagrams for the given system takes time and some amount of experimental work.

2.3 Symbolic sweeping: swirls and saddles

A bi-parametric, $(\lambda,\ \alpha)$-scan of Eqs. (2.1) at $B = 0$ using the $\{5-15\}$ kneading range is presented in Fig. 2.5. This high-resolution diagram is made of 40 panels, each with $10^3 \times 10^3$ mesh points. A region of a solid color corresponds to a constant kneading invariant, i.e. to structurally stable and simple dynamics in the system. In such regions, trivial attractors, such as stable equilibria or stable periodic orbits, dominate the dynamics of the model. The red, blue and light blue colors correspond to constant values of the kneading invariants: 0, 1 and 2/3 generated, resp., by sequences $\{0\}^\infty$, $\{1\}^\infty$ and $\{10\}^\infty$. Note that the kneading approach does not distinguish between symmetric and asymmetric periodic orbits, for instance, of the figure-eight shape generating the same sequence $\{10\}^\infty$. As such it does not detect pitch-fork and period-doubling bifurcations.

A borderline between two solid-color regions corresponds to a homoclinic bifurcation at which the kneading invariant becomes discontinuous and experiences a sudden jump in its value. So, the border between the blue (the kneading invariant $K = 1$) and the red ($K = 0$)

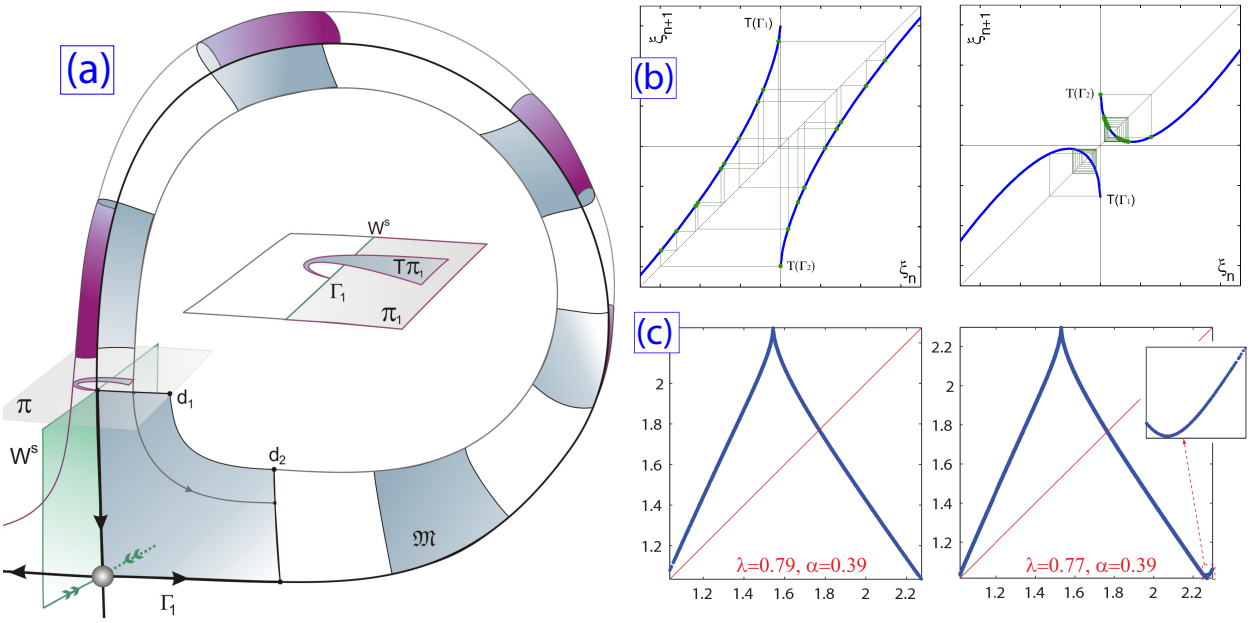

Figure (2.7) (a) Geometry of an inclination-switch homoclinic bifurcation causing the emergence of stable orbits near the saddle with a saddle index $\nu < 1$. Its core element is local expansion ($d_1 < d_2 \sim d_1^{\nu}$) of an area, $\mathfrak{M}$ between a 1D outgoing separatrix Γ^+ and a close trajectory. This is further followed by bending such that the global return map T takes a cross-section Π, transverse to a 2D stable manifold of the saddle, becomes a contraction with stable fixed points, rather than an expansion generating saddle fixed points. (b) 1D discontinuous Lorenz map (2.4) without and with bending, resp., prior to and after the inclination-switch bifurcation. Progressive bending gives rise to a saddle-node bifurcation, followed by a cascade of period-doubling bifurcations, followed by a secondary homoclinics as soon as the graph, $T\Pi_1$ lowers below the ξ_n-axis. (c) The evolution of the cusp-shaped graph of the 1D-map generated by critical points of the z-coordinate of a chaotic trajectory on the Lorenz attractor in the SM-model above and below the boundary $A = 0$, (Fig. 2.8) resulting in the formation of the characteristic hook (bend).

regions corresponds to the bifurcation curve, HB, of the primary homoclinic butterfly. The same curve is continued as a borderline between the blue and light blue regions. The point where all three regions come together on the bifurcation curve corresponds to the resonant saddle with $\nu = s_1/|s_2| = 1$, or with zero saddle value: $\sigma = s_2 + s_1 = 0$. To the right of it, the homoclinic bifurcation with $\sigma < 0$ "glues" two stable periodic orbits, emerging from stable foci through a a supercritical Andronov-Hopf curve, AH, into a single orbit (x, y)-projected as a figure-eight (Fig. 2.5). To the left, the codimension-two point, $\sigma = 0$ ($\nu = 1$) originates a loci (bundle) of bifurcation curves that determine the dynamics of the Lorenz attractor and shape its existence region. The bundle is bordered by two curves: LA, bounding the

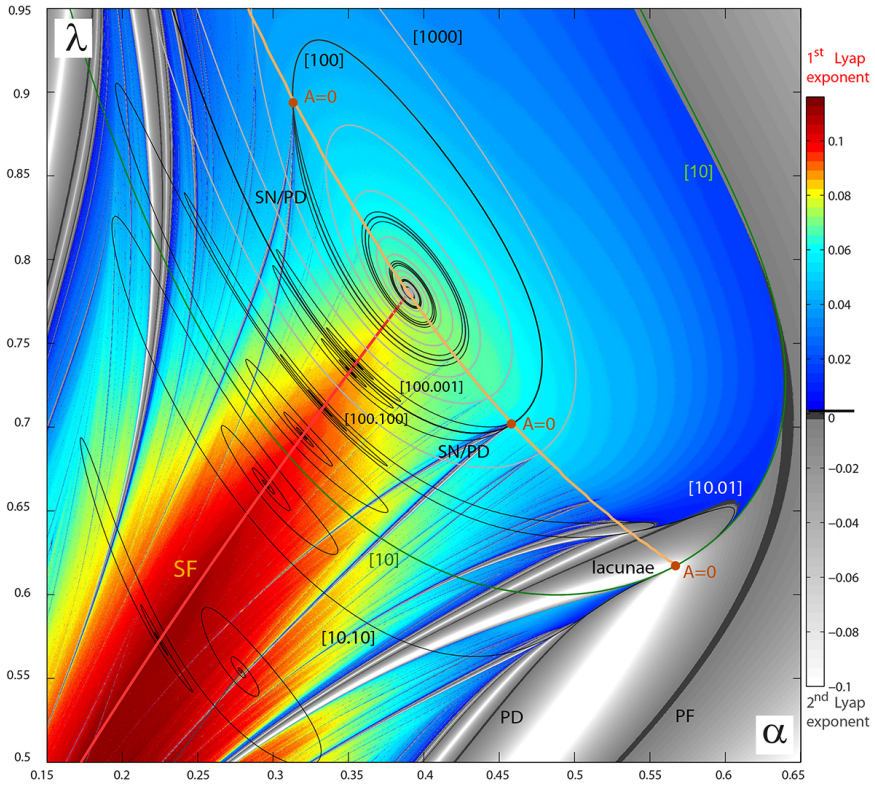

Figure (2.8) Bi-parametric LE-sweep superposed with homoclinic (black) and heteroclinic (red) bifurcation curves. Grey shades and colors are associated with LE quantities: $\lambda_2 < \lambda_1$. Major Shilnikov flames containing stability windows adjacent to codimension-two inclination-switch bifurcations (dots) on the [orange] curve, A=0, demarcating the boundary of the existence region of the Lorenz attractor in the (α, λ)-parameter plane; the SN, PF and PD labels identify saddle-node, pitch-fork and period-doubling bifurcations. Superimposed black lines are several principal bifurcations curves of separatrix loops, which are obtained by the parameter continuation. Note a bifurcation pathway connecting two T-points.

red region from below, corresponds to the formation of the Lorenz attractor. The other curve, 2HB, on the border between the light-blue region and multi-colored region of chaos, corresponds to a double pulsed homoclinic loop [40; 35]. The inclination-switch bifurcation of this loop plays a critical role in the transformation of the Lorenz attractor with no stable periodic orbits into a quasi-hyperbolic one with stable orbits [in stability windows].

This diagram is a demonstration of this new computational approach. A feature of complex, structurally unstable dynamics is a dense occurrence of homoclinic bifurcations, which are represented by curves of various colors that foliate the chaotic region in the bi-

parametric scan. We stress that given the depth (10 kneadings) of the scanning and the resolution of the colormap, the diagram can potentially reveal up to 2^{10} distinct bifurcation curves of homoclinic trajectories up to the indicated length. The top right picture in Fig. 2.5 presents a bi-parametric sweep of the same region, using a longer tail, $\{12-20\}$, of the kneading sequence. The sweep reveals fine organization structures foliating the existence region of the Lorenz attractors with bifurcation bundles, as well as two pronounced saddles separating the loci that converge to the primary T-point. They also show a "turbulent plume" made of swirling bifurcation structures originating from the primary T-point. The plume appears noisy due to color alternations and excess low-scale details. In what follows, we will focus on the complex self-similar organization and interconnection of such bifurcation structures centered around subsequent T-points.

2.4 Self-similarity of homoclinic swirls

The bi-parametric sweep in Fig. 2.6 explores a fractal self-similar organization of bifurcation swirls, which are centered around subsequent T-points. These points, including the secondary one, T_2 at $(0.2784, 0.5543)$, are parented by the primary one, $T_1(0.3903, 0.7805)$, located at right-top corner of the left panel. One can see that the diagrams disclose all details of the bifurcation structures of the Bykov T-points [3]. Fine structures of the bi-parametric scan can be enhanced further by examining longer tails of the kneading sequences. This allows for the detection of smaller-scale swirling structures within the homoclinic scrolls, as predicted by theory (Fig. 2.2). From it we know that the subsidiary/peripheral points, T_{1k}, parented by the primary one, T_1, must nest within an ultra thin wedge bordered by the bifurcation curves corresponding to an initial homoclinic loop of either saddle-focus and a heteroclinic connection between both saddle-foci. To figure out a fractal hierarchy for the embedded swirls, we take a one-parameter sweep of the kneading invariant along a T-point pathway. The result is shown in the bottom panel in Fig. 2.6. The right end point at $\alpha = 0.3903$ in the diagram corresponds to the primary T-point. In it, local maxima and minima are associated to subsidiary T-points, while discontinuous points mark homoclinic

bifurcations at which the kneading abruptly jumps in value. This diagram allows one to evaluate a renormalization factor of the fractal line. We can conjecture that the turbulent transition of homoclinic swirls is imperative for homoclinic bifurcation curves, which cannot cross each other, to embed into the compact region of chaotic dynamics in the SM model. In this region chaotic dynamics in the SM model due to the Lorenz attractor are additionally amplified by spiral chaos due to Shilnikov's saddle-foci. Such chaos in the parameter space caused by the abundance of T-points, and due to interaction of the homoclinics of the saddle and saddle-foci, and contrasts vividly to a well parameterized foliation of the existence region of the Lorenz attractor above the primary T-point. Next we will analyze the way the foliation breaks down on a boundary below which the Lorenz attractor transforms into a quasi-chaotic attractor coexisting with stable periodic orbits with narrow attraction basins. Note that alternation of stability windows with stable periodic orbits and chaos is a feature of systems with saddle-foci and sign constant divergence like the model under consideration.

2.5 Inclination-switch bifurcations

In [29] L.P. Shilnikov introduced the conditions giving rise to bifurcations of codimension-two termed as orbit-flip and inclination-switch that can only occur in 3D+ systems. Besides that, the inclination-switch bifurcation even in the case of an expanding saddle with the saddle index satisfying the condition $1/2 < \nu < 1$ can also lead to the onset of stable orbits in the phase space of systems. As such, the occurrence of such a bifurcation is an alarming sign for the Lorenz attractor in the SM-model. Below we will outline the essence of the inclination-switch bifurcation. Its in-depth analysis is given in [1].

Figure 2.7 illustrates the concept of the an inclination-switch bifurcation, which gives rise to the emergence of a stable orbit. The setup is the following: the 1D separatrix Γ^+ of the saddle of type (2,1) comes back to the saddle along the [vertical] leading direction. We explore the global map that takes a cross-section, Π, transverse to the stable manifold, W^s, onto itself along the homoclinic loop. Typically, the local map near the saddle is an expansion for $\nu < 1$, i.e. it must stretch a square or a volume. Figure 2.7 sketches how the local map

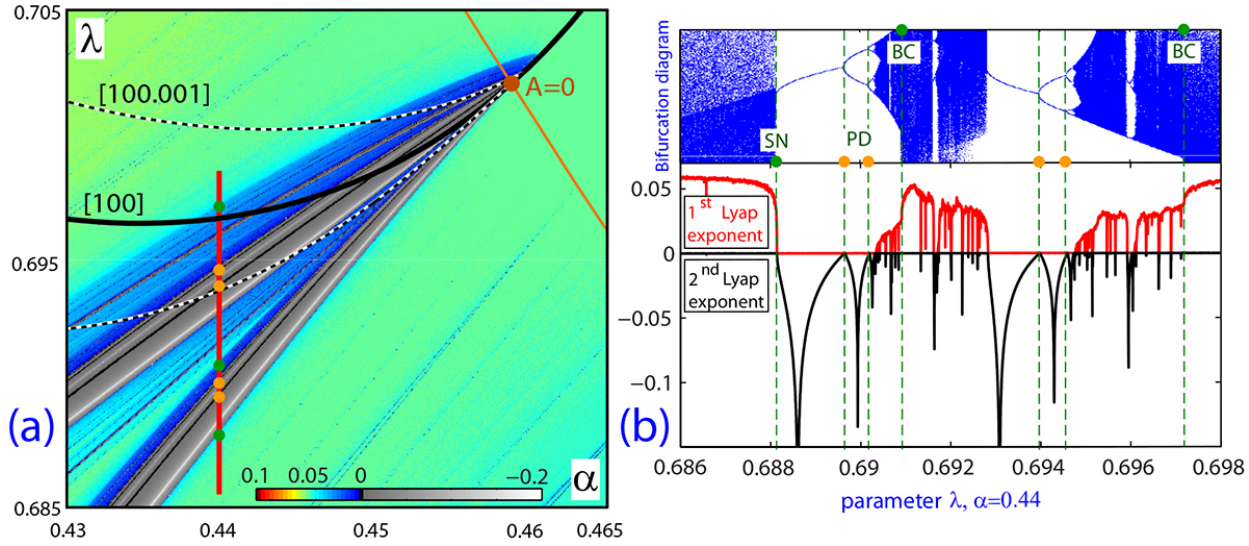

Figure (2.9) (left) LE-sweep magnification of a Shilnikov flame near the codimension-two point of the [100]-homoclinic loop revealing the fine organization of the bifurcation unfolding and the stability windows. (right) One-parameter cut through the Shilnikov flame (depicted in panel (a)) disclosing cascades of SN and PD bifurcations within it, as well as the occurrence of the secondary, [100.100] and [100.001], homoclinics.

takes a small interval $d_1 \ll 1$ on Π into $d_2 \sim d_1^{\nu} > d_1$. Let us picture an evolution, along the separatrix loop, of a piece, $\mathfrak{M}$, of a leading manifold, being defined locally and tangent to a span of the eigenvectors corresponding to the leading stable and unstable characteristic exponents, $s_2 < 0 < s_1$, resp., of the saddle. As $\mathfrak{M}$ is dragged away from the saddle by the outgoing separatrix, it starts curving so that it hits the cross-section, Π, with a transversally squeezed hook due to the strongly stable exponent, $s_3 < s_2$. Because of bending, the image of d_2 becomes shorter than the original, d_1, i.e. $\mathrm{T}\, d_1 < d_1$ which was not the case prior to the bifurcation when the overall map was a stretching one. In the aftermath of bending, the global map T becomes a contraction after it overcomes the persistent stretching effect of the local map near the saddle. This map makes the image $\mathrm{T}\Pi_1$ of the right (relative to the stable manifold, W^s, of the saddle) portion, Π, of the cross-section stretch and bend, so that it looks like a hook or a Smale horseshoe. As such, the map may gain stable fixed points coexisting along with saddle periodic ones.

The 2D return map near the primary homoclinic butterfly of two separatrix loops of a saddle is a core of the geometric model of the Lorenz attractor proposed in [6]. The map is

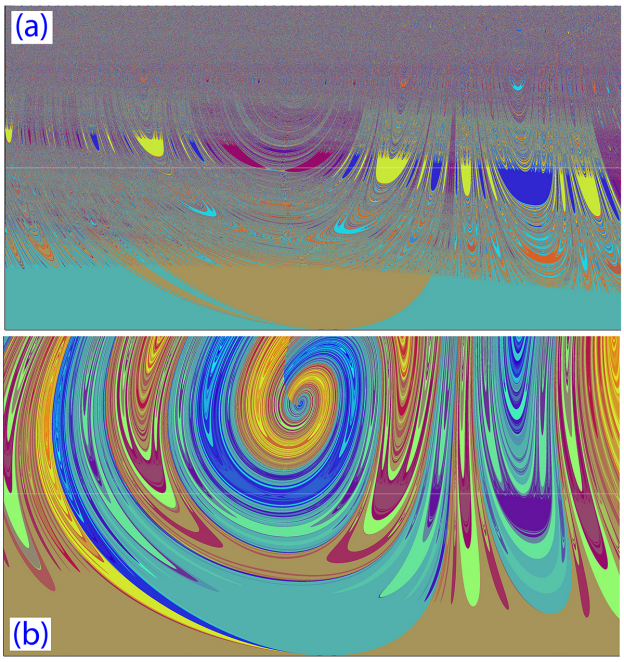

Figure (2.10) (a) $\{6-20\}$ and (b) $\{17-20\}$-kneading ranges revealing a fine structure and self-similarity of the fractal border between the regions of simple dynamics (solid color) and complex chaotic dynamics.

supposed to meet a few analytical conditions guaranteeing that a system in question possesses a genuine chaotic attractor without stable orbits and homoclinic tangencies. A violation of the conditions occurs on a boundary of its existence region. Near the aforementioned codimension-two bifurcations the 2D map can be further reduced to a simplified 1D map (Fig. 2.7) in the following form [1]:

$$\xi_{n+1} = \left[\mu + A|\xi_n|^{\nu} + o(|\xi_n|^{2\nu})\right] \cdot \mathrm{sign}(\xi_n), \tag{2.4}$$

here $1/2 < \nu = |\lambda_2|/\lambda_1 < 1$ is the saddle index, μ controls the distance between a separatrix, Γ^+, and the stable manifold, W^2 of the saddle at the origin, and A is the separatrix value [40]. The term $o(|\xi_n|^{2\nu})$ is no longer negligible whenever $|A| \ll 1$ near the inclination-switch bifurcations. The top right panels in Fig. 2.7 illustrate the geometry of the map for positive and negative A. One can figure from the geometry of the hooked map that the unfolding an inclination-switch bifurcation must include saddle node (tangent) and period-doubling

bifurcations of fixed points, as well as double homoclinics. Say, if the inclination-switch occurs at the homoclinic loop with the [10] kneading, there will be a couple of bifurcation curves of double homoclinics, [10.10] and [10.01] emerging from the codimension-two points. An alternative, though expensive, solution for locating the curve $A = 0$ in the parameter space is by detecting the hooks in the return map generated by successive minima of the z-variable. Two such maps above and below the curve $A = 0$ at two locations, $\alpha = 0.39$, and $\lambda = 0.79$ and $\lambda = 0.77$, are presented in the bottom right panel of Fig. 2.7. The later map features a second smooth critical point in addition to the cusp that will break down the instability and lead to the occurrence of stable periodic orbits in the phase space and stability windows in the parameter space of the SM-model. We note that at lower λ and α values there are other curves similar to $A = 0$ [35]. Crossing down each such curve makes the return map bend again to gain additional turns. With every new turn, the map near the saddle starts appearing like the Poincaré map near a Shilnikov saddle-focus. The distinction though is that the spiraling saddle-focus map generates countably many Smale horseshoes, whereas the map near such twisting saddle has only a finite number of turns.

2.6 Shilnikov flames

The geometry of the formation of homoclinic hooks in Fig. 2.7 suggests a computational algorithm for detecting the boundary in the parameter space of the model beyond which the system may have stable orbits along with the Lorenz attractor [53; 25; 34; 40]. The algorithm takes into consideration the behavior of two trajectories: the separatrix itself and close one above it because the leading direction at the saddle here is the z-axis. The [orange] curve of the hook formation is denoted by $A = 0$ in Fig. 2.8, thus symbolizing the original concept – the zero separatrix quantity A [16]. Above (below) the curve, $A > 0$ ($A < 0$) and hence all separatrix loops are orientable ore become non-orientable (Fig. 2.3). Its intersection points with the corresponding homoclinic curves correspond to codimension-two inclination-switch bifurcations, the sequence of which begins with the very first point on the curve, labeled [10] in Fig. 2.8, standing for the double homoclinic loops.

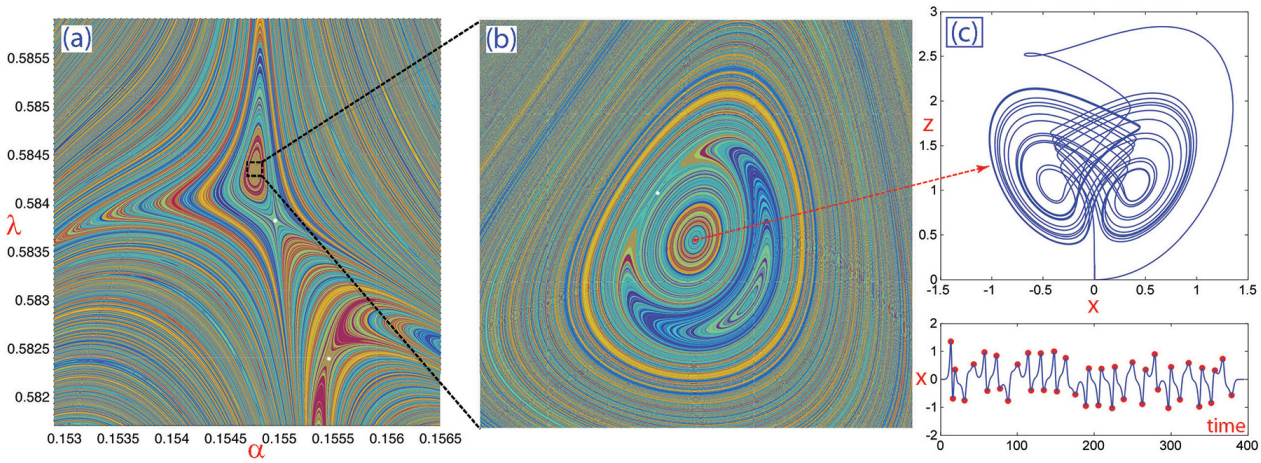

Figure (2.11) (a) Embedded centers and saddles (white dots) in the parameter plane fragment. Scan of $\{20-35\}$-kneading range. (b) Magnification of the center region with a fine arrangement of self-similarity of long flip-flops of homoclinic bifurcations. Scan of $\{25-40\}$-kneading range. (c) Long flip-flop homoclinic connection at ($\alpha = 0.1548$, $\lambda = 0.5843$) corresponding to the center point.

In Fig. 2.8 we present a bi-parametric LP-sweep of the SM-model near the primary T-point to study the transition from the existence region of the Lorenz attractor to the regions of quasi-chaotic dynamics with inclusions of stability windows. Areas with grey shadows stand for the regular dynamics due to the presence of stable periodic orbits, for which $\lambda_2 < 0$, $\lambda_1 = 0$. Here, dark grey lines indicate bifurcations, saddle-node (SN), pitch-fork (PF) and period-doubling (PD), where λ_2 approaches zero from below. The colored regions stand for chaotic dynamics with $\lambda_1 > 0$; particularly, colors in the spectrum are associated with a range of λ_1 positive values. This diagram is superimposed with several homoclinic and heteroclinic bifurcations curves obtained by the parameter continuation technique. The abbreviation SF stands for the bifurcation curves of Shilnikov saddle-foci around which (red zone) the Lyapunov exponent is maximized. Labels [100], [10.01] based on kneading notations, stand for bifurcation curves of homoclinic loops spiraling toward the T-point. Several dots, labeled $A = 0$, mark the locations of codimension-two inclination-switch bifurcations on the [orange] curve below the hook formation that gives rise to the depicted homoclinic curves. The curve $A = 0$ demarcates the boundary of the existence region of the Lorenz attractor leading to its termination and giving rise to the emergence of stable periodic orbits. Such orbits exist and

bifurcate within stability windows, called *Shilnikov flames.* Each such flame originates from a codimension-two homoclinic bifurcation that occurs at the intersection point of a homoclinic bifurcation curve with the curve $A = 0$. Since the Lorenz attractor is structurally unstable, homoclinic bifurcation curves densely foliate its existence region (Fig. 2.5a), and produces countably many codimension-two inclination-switch points on $A = 0$. Loosely speaking, the physical length of homoclinic loops can be viewed as the order number of the Shilnikov flames, which are bigger the lower the order number. Several such flames are revealed in Fig. 2.8: the largest ones originate from the inclination-switch bifurcations (on $A = 0$) corresponding to the shortest homoclinic loops, symbolically encoded as [10], [100], [10.01], etc. The left panel in Fig. 2.10 enlarges the Shilnikov flame at the crossing of $A = 0$ and the [100]-homoclinic loop, while the right panel presents a one-parameter bifurcation diagram along the vertical (red) λ-segment cross-cutting through the flame. Both unambiguously reveal the inner bifurcation organization of the flame including saddle-node bifurcations (Fig. 2.8) followed by a period-doubling cascade and secondary bifurcations of homoclinic loops, here [100.100] and [100.001]. One can see from Fig. 2.8 that the homoclinic bifurcation curves spiral up onto the matching T-points. The saddle-node bifurcations bound the margins of the stability windows, and a period-doubling cascade within, which are all typical for quasi-attractors — where a complex hyperbolic trajectory structure coexists or becomes intermittent with stable periodic orbits. These nonlocal bifurcation puzzles agree well with the Bykov theory of T-points illustrated in Fig. 2.2 and the theory of codimension-two homoclinic bifurcations [35; 1]. As such, the curve $A = 0$ sets a borderline demarcating the existence region of the Lorenz attractor from below in the (α, λ)-parameter space [40].

2.7 Wild chaos in phase & parameter space

In the region below the curve $A = 0$, the dynamics of the SM-model becomes wildly unpredictable. Here, we use two senses of the term "wild." One is that the chaotic dynamics due to the Lorenz attractor are amplified by spiral chaos due to the Shilnikov saddle-foci near the primary T-point pathway, SF, in the LE-diagram in Fig. 2.8. This leads to onsets of *quasi-*

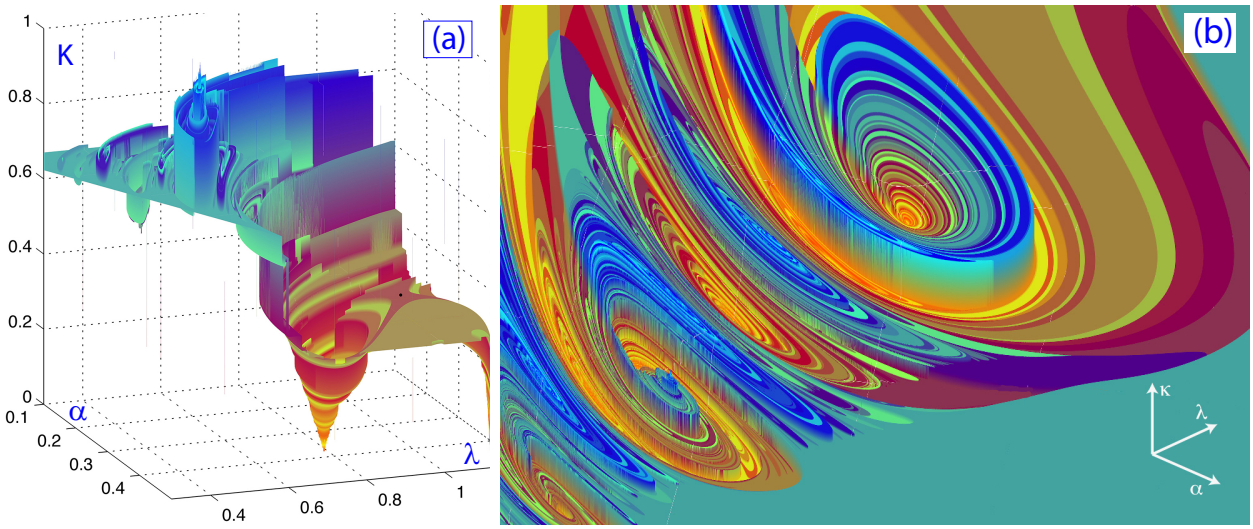

Figure (2.12) (a) Kneading surface depicting the vicinity of the primary T-point – a large vortex in the (α, λ, K)-parameter space, whose basin is bounded by a saddle (white dot). (b) Magnified fragment of the bifurcation surface near the primary T-point stirring the region of wild dynamics with multi-fractal organization; Here is the $\{5-15\}$-kneading range.

chaotic attractors, the paradigm of which was introduced and developed by L.P. Shilnikov within the framework of the mathematical Chaos theory [13; 11; 12]. Such a chaotic set is impossible to parameterize and hence to fully describe its multi-component structure due to dense complexity of ongoing bifurcations occurring within it [43]. The complexity of the bifurcation structure of the Lorenz-like systems in regions of quasi-attractors is a perfect illustration of this paradigm. This is a second sense of the term wild: unlike the well-foliated existence region of the Lorenz attractor by bundles of bifurcation curves, the region of quasi-attractors is intricately stirred by T-points of various scales, and mixed with stability windows corresponding to stable periodic orbits emerging and vanishing as the parameters are varied.

In terms of the Lyapunov exponents quantifying instability of trajectory behaviors, the direct indication of intensifying disorder is the presence of a red(ish) zone around the pathway where the positive (largest) LE is maximized, compared to the cold (blue) chaos of the Lorenz attractor. In the wild-chaos region, bifurcations of homoclinic and periodic orbits become totally unpredictable [54]. One can see from Fig. 2.5(b) showing the $\{12-22\}$-kneading scan

of the SM-model that the parameter region below the primary T-point appears quite noisy. The reason "parameter turbulence" created and stirred by homoclinic swirls of various scales that make it hard to find two points in this region with the same kneading value. Below we will present and discuss a few cases of interesting parameter structures revealed by this kneading toolbox. We remind the Reader that that these are homoclinic structures made of separatrix loops of finite lengths (no more than 50 kneadings).

The first in the list is an organization of a fractal boundary between the regions of chaos and simple dynamics due to stable periodic orbits; the latter is color-coded with grey in Fig. 2.4 and in light-blue in Fig. 2.5(a). Let us re-iterate that the kneading toolbox designed for homoclinic bifurcations does not detect local bifurcations of stable periodic orbits. As such, the region of trivial dynamics looks solid blue without any trace of pitch-fork, saddle-node or period-doubling bifurcations that are known to occur there, as we can see from Fig. 2.4. Figure 2.10 focuses on a fragment of the kneading scan in the vicinity of the T_2-point (Fig. 2.6) near a border between the region of simple dynamics (solid color), dominated by stable periodic orbits and chaos. Its panels, presenting two resolution scans of $\{6-20\}$ and $\{17-20\}$-kneading range, reveal self-similar structures that constitute a fractal border. On the border, a chaotic attractor undergoes an intrinsic crisis and breaks into two asymmetric ones emerging through period-doubling cascades [32; 40], just like the Lorenz model at large Rayleigh numbers [55; 56]. In terms of the 1D bended maps depicted in Fig. 2.7, this occurs when the critical points cross the horizontal axis, which lets trajectories, which used to be trapped on either side of the unimodal graph of the map, switch between both branches thus filling in a symmetric chaotic attractor.

2.7.1 Elliptic islands and saddles

In the region of wild dynamics there are a variety of curious homoclinic bifurcation phenomena that are revealed by the symbolic toolkit. They are by-products of swirling patterns due to T-points, which can be viewed as "dissipative" structures in the parameter space. In contrast, "conservative" (looking) structures are comprised of elliptic islands separated

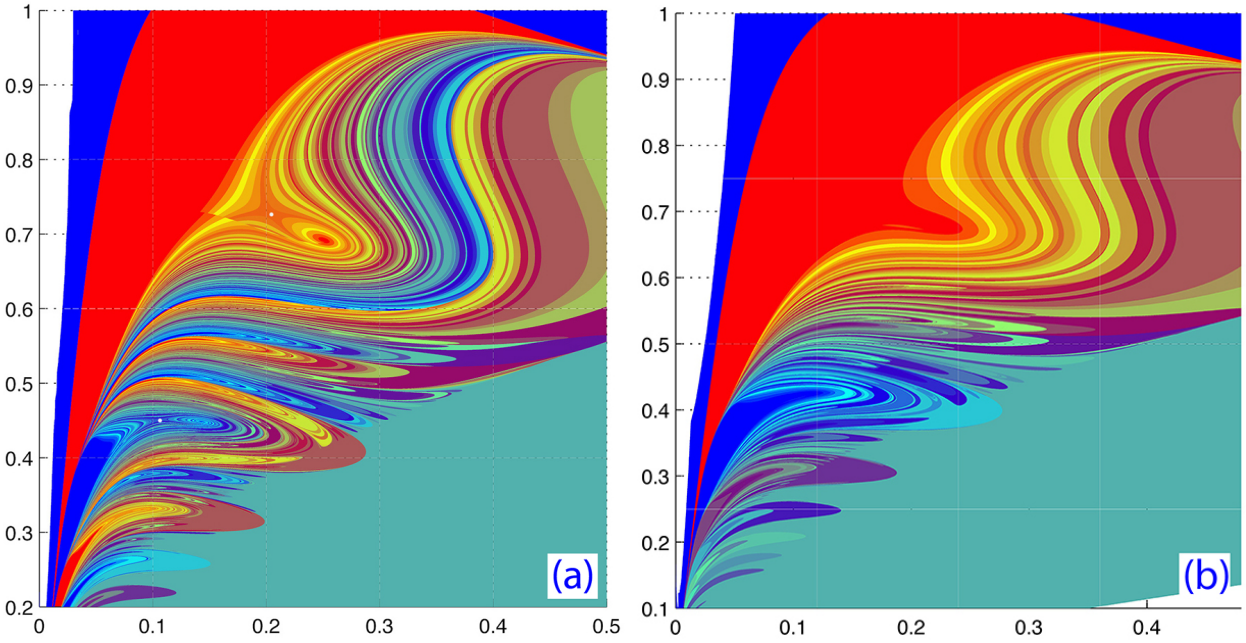

Figure (2.13) Two slices, at $B = 0.11$ and $B = 0.125$, of the 3D bifurcation diagram in the (α, λ, B)-parameter space, showing "saddle-node" bifurcations eliminating T-points merging with nearby saddles (white dots). The kneading range is $\{5 - 15\}$. Compare with Fig. 2.5 at $B = 0$.

by saddles, as the ones shown in Fig. 2.11. An elliptic island appears as a collection of concentric rings. Unlike T-points, each ring is a closed level curve corresponding to a long homoclinic loop with a kneading that does not change along the ring. Increasing the kneading resolution lets one obtain deeper insight into the organization of elliptic islands in the parameter plane. It turns out that, like T-points, there is another self-similar organization of embedded saddles and non-nested centers on smaller scales within which may appear to be outer rings (Fig. 2.11b). The closer one approaches a center of the rings, the greater the number of flip-flops and twists the outgoing separatrix makes before returning to the saddle at the origin. As in the case of conservative dynamics, a saddle in the parameter plane sets a threshold between level curves of constant kneadings.

2.8 "Saddle-node" bifurcations in 3D-parametric sweeps

Homoclinic bifurcation curves disclosed by the computational toolkit can be viewed as level curves of constant kneadings values. Recall that by construction (not counting the very

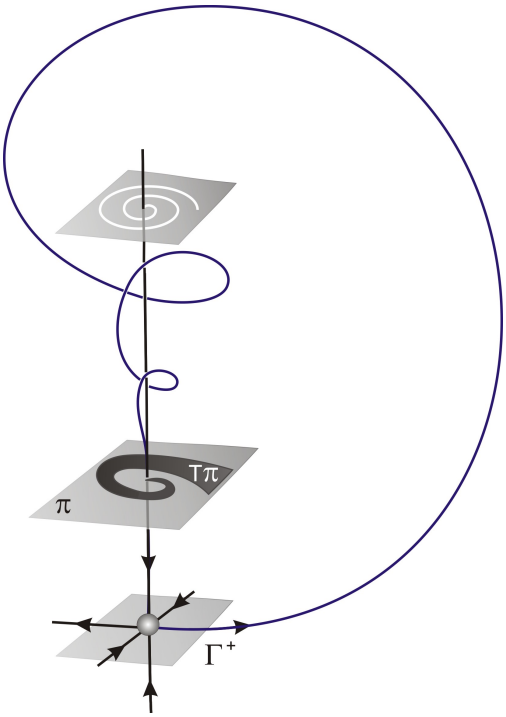

Figure (2.14) Slow-fast dynamics as an origin of an inclination-switch bifurcation in the SM-model. Sketch of a twisting flow making the separatrix of the saddle turn around the stable leading direction, the z-axis, and hence the return map, T, taking a cross-section Π into itself, appears like that of the genuine Shilnikov saddle-focus.

first "+1"), the range of the kneading values is $[0, 1]$. Therefore, we can look at the kneading bifurcation diagrams from different angles, as in Fig. 2.12 depicting two fragments of the kneading *surface* in a 3D (α, λ, K)-parameter space; K from (2.3) denotes the kneading value. Now, T-points are viewed as local maxima and minima (vortices) separated by saddles. In the given context a saddle in the parameter plane is a point at which two level curves corresponding to the same kneading touch and next swap Loosely speaking, such a surface can be visualized as a potential [in terms of physics] with non-crossing pathways other than at singularities – saddles and T-points, and other codimension-two points in the parameter space. This interpretation is useful for a forthcoming explanation of "bifurcations" of bifurcation curves in the SM-model (2.1) as the third parameter, B is varied. Recall that, up to now we have presented the results for $B = 0$.

Figure 2.13 depicts two slices, at $B = 0.05$ and $B = 0.11$, of the 3D bifurcation diagram

in the (α, λ, B)-parameter space. The panels demonstrate the evolution of the original diagram in Fig. 2.5 as B is increased. One can see T-points vanishing with an increase of B through merges with nearby saddles, so that the chaos region will eventually be foliated by untwisting level curves originating from the codimension-two point corresponding to the resonant homoclinic saddle with a zero saddle value, and terminating at ($\alpha = \lambda = 0$), which corresponds to a singular system with all three equilibria gathered at the origin. To draw a parallel with a saddle-node bifurcation of equilibria in a phase plane, one can speak of similar bifurcations of saddle and T-point structures in the parameter space that occur as the kneading surface rids of vertices and becomes "more flattened." Recall that like phase trajectories, homoclinic bifurcation curves do not cross and terminate at singularities – codimension-two points, like T-points, and the ones corresponding to resonant saddle and inclination-switch bifurcations.

2.9 Precursor of inclination-switching

In this final section we will try to rationalize the cause of inclination-switch bifurcations in the SM-model. An evidence or, vice-versa, a consequence of such a bifurcation is various cascades of period-doubling bifurcations that occur in flows, which, loosely speaking, generate bending return maps.

Let us consider the SM-model (2.1), at $B = 0$ for simplicity, in the singular limit $\alpha = 0$, where the z-variable becomes a control parameter:

$$\dot{x} = y, \quad \dot{y} = x - \lambda y - xz, \quad z \geq 0. \tag{2.5}$$

The stability of the only equilibrium state of this linear system (fast subsystem at $\alpha \ll 1$) depends on the height of z: $s_{1,2} = \left[-\lambda \pm \sqrt{\lambda^2 - 4(1-z)}\right]/2$. For $z < \lambda^2/4 + 1$, the origin is a saddle, while it becomes a stable focus at larger z-values. This will determine the dynamics of the system close to the z-axis when α is small. So, whenever the saddle has a homoclinic loop, depending on how high the returning separatrix Γ^+ climbs up in the phase space, it

may turn around the leading stable direction – the z-axis. The number of turns depends on how long the separatrix Γ^+ follows the "spiraling" segment of the z-axis and on how strong the twisting flow is nearby, see the sketch in Fig. 2.14. Multiple inclination-switches help the homoclinic saddle pretend to be a genuine Shilnikov saddle-focus. This phenomenon, called extra-twisting, was also observed in the Lorenz model at small parameter values [57]. Such a twisting in the limiting case is a precursor of the inclination-switch bifurcations in the SM-model and other alike systems. An indirect answer to the question of whether a homoclinic loop is oriented or non-oriented (twisted) is basically determined by how high the returning separatrix goes while approaching the leading z-axis on the stable manifold of the saddle at the origin.

2.10 Model of homoclinic garden (HG)

The Homoclinic Garden (HG) model is described by the following system of three differential equations:

$$\dot{x} = -x + y,\ \dot{y} = (3 + \mu_1)x + y(1 + \mu_2) - xz,\ \dot{z} = -(2 + \mu_3)z + xy \tag{2.6}$$

with three positive bifurcation parameters: μ_1, μ_2, and μ_3. An important distinction of Equation (2.6) from the Lorenz equations is the positive coefficient at y in the second equation. Note that equations with such a term arise e.g. in finite-dimensional analysis of the weakly dissipative Ginzburg-Landau equation near the threshold of the modulational instability ([58]).

Equation (2.6) are $\mathbb{Z}_2$-symmetric. In the relevant region of the parameter space the steady states of the system (2.6) are a saddle at $x = y = z = 0$,along with two symmetric saddle-foci at $x = y = \pm\sqrt{(4 + \mu_1 + \mu_2)(2 + \mu_3)}$, $z = 4 + \mu_1 + \mu_2$. At $\mu_3 = 0$ the system (2.6) possesses the globally attracting two-dimensional invariant surface. If, additionally, μ_2 vanishes, dynamics upon this surface is conservative, and two homoclinic orbits to the saddle coexist due to the symmetry. On adding the provision μ_1, we observe that two real negative

eigenvalues of the linearization matrix at the saddle are equal. Hence, in the parameter space the codimension-3 point $\mu_1 = \mu_2 = \mu_3 = 0$ serves as a global organizing center which gives birth to curves of codimension-two homoclinic bifurcations: resonant saddle, orbit-flip and inclination-switch ([1]) as well as codimension-one bifurcation surfaces corresponding to symmetric homoclinic loops of the origin.

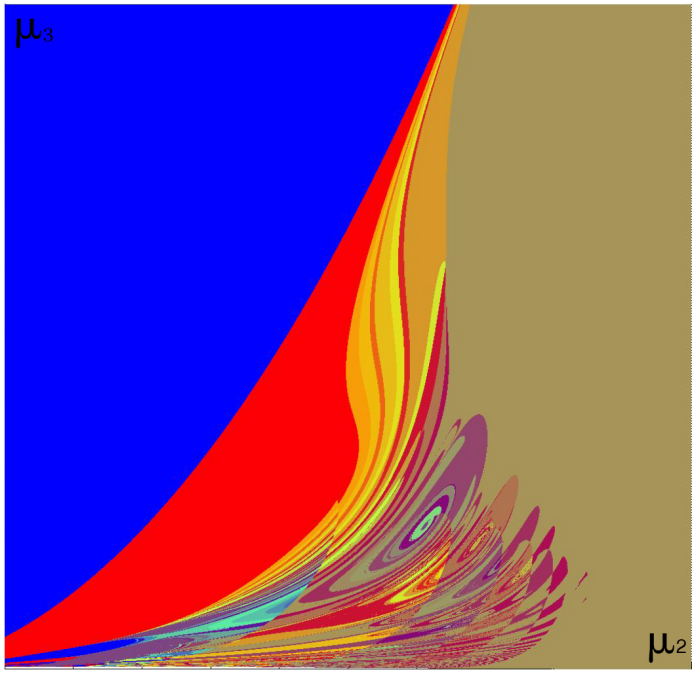

Figure (2.15) Pilot bi-parameter sweeping of the HG-model using the very first 10 kneadings at $\mu_1 = 0$. Solid colors correspond to regions of simple dynamics. Multicolored regions fill out the chaos land. The borderline between red and the blue regions corresponds to the primary homoclinic butterfly bifurcation.

At the first stage of the pilot study of the HG-model, we performed a bi-parametric, (μ_2, μ_3), scan of Eqs. (2.6) using the first 10 kneadings. This colormap of the scan is shown in Fig. 2.15. The brown region is dominated by the stable periodic orbit, coded with two symbols $[1, 0]$. The pilot scan clearly indicates the presence of the complex dynamics in the model. A feature of the complex, structurally unstable dynamics is the occurrence of numerous homoclinic bifurcations, which are represented by border lines of various colors that foliate the corresponding region in the bi-parametric scan. One can note the role of

the codimension-two orbit-flip bifurcation ([1]) at $\mu_1 = \mu_2 = 0$ in shaping the bifurcation diagram of the model. Observe that the depth (10 kneadings) of the scanning can only reveal homoclinic trajectories/bifurcations up to the corresponding configurations/complexity.

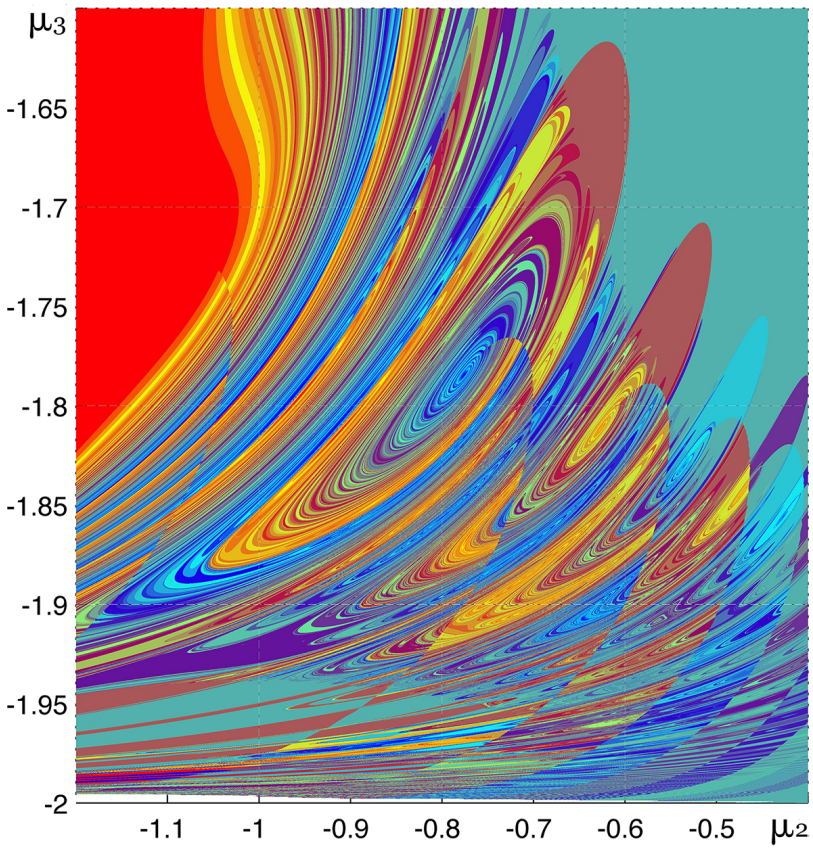

Figure (2.16) High resolution, [5-15] kneading-range scan of dynamics of the HG model showing a complex fractal structure of the parameter space. Centers of swirls correspond to heteroclinic T-points of codimension-2. The scan is made of 16 panels, each with $[10^3 \times 10^3]$ mesh points. One color curve corresponds to a homoclinic bifurcation of the saddle at the origin.

Figure 2.16 represents a high-resolution scan of the complex dynamics of the HG-model, using the same [5-15] kneadings. It is made of 16 panels, each one with $10^3 \times 10^3$ mesh points. This diagram is a de facto demonstration of this computational technique. This color scan reveals a plethora of T-points as well as the saddles separating swirling structures. One can see that the diagram reveals adequately the fine bifurcation structures of the Bykov T-

points ([3]). The structure of the bi-parametric scan can be enhanced further by examining longer tails of the kneading sequences. This allows for the detection of smaller-scale swirling structures within the larger scrolls, as predicted by the theory.

2.11 Lorenz Model: Primary and Secondary T-points

The Lorenz equation ([2]) from hydrodynamics is a system of three differential equations:

$$\dot{x} = -\sigma(x - y),\ \dot{y} = rx - y - xz,\ \dot{z} = -\frac{8}{3}z + xy \tag{2.7}$$

with positive parameters: σ being the Prandtl number quantifying the viscosity of the fluid, and r being a Rayleigh number that characterizes the fluid dynamics. Note that Eqs. (2.7) are $\mathbb{Z}_2$-symmetric.

The primary codimension-two T-point at $(r = 30.38, \sigma = 10.2)$ corresponding to the heteroclinic connections between the saddle and saddle-foci in the Lorenz equation was originally discovered by Petrovskaya and Yudovich ([37]). They initially conjectured that its bifurcation unfolding would include concentric circles, not spirals, corresponding to bifurcation curves for homoclinic loops of $\{1, [0]^{(k)}\}$ symbolic representations, with quite large k (> 40). Figure 2.17 represents the (r, σ) kneading scans of the dynamics of the Lorenz equation near the primary T-point. In the scan, the red-colored region corresponds to a "pre-turbulence" in the model, where chaotic transients converge eventually to stable equilibria. The borderline of this region corresponds to the onset of the strange chaotic attractor in the model. The lines foliating the fragment of the parameter plane correspond to various homoclinic bifurcations of the saddle at the origin. Observe the occurrence of a saddle point in the parameter plane that separates the bifurcation curves that winds onto the T-point from those flowing around it. Locally, the structure of the T-point and a saddle recalls a saddle-node bifurcation. Note too that likewise trajectories of a planar system of ODEs, no two bifurcation curves can cross or merge unless at a singularity, as they correspond to distinct homoclinic loops of the saddle.

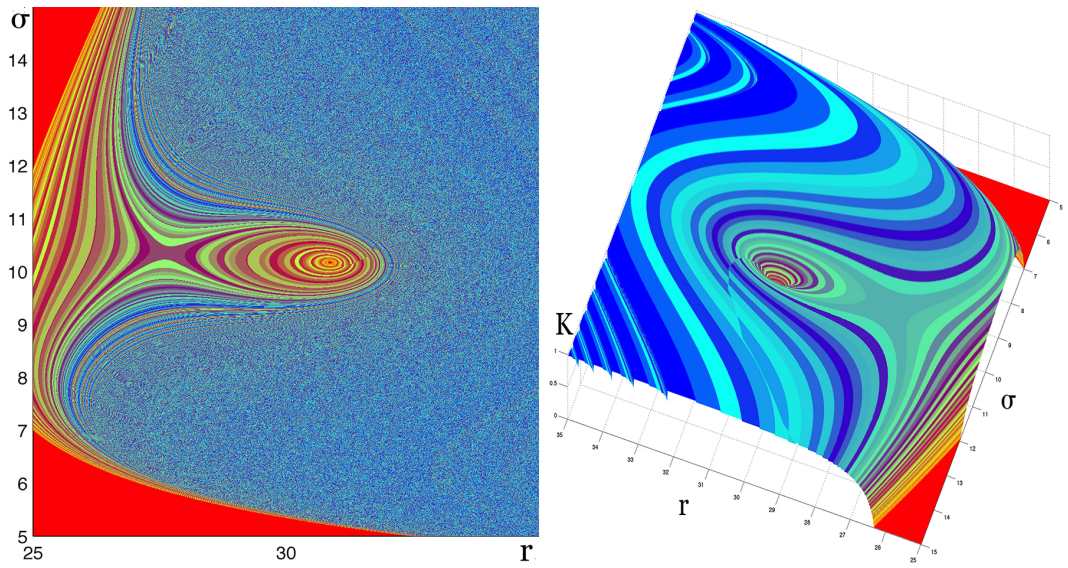

Figure (2.17) Bi-parametric scans, 2D and 3D, of different depths of the Lorenz equation around the primary T-point at ($r = 30.38, \sigma = 10.2$). Solid red region corresponds to the kneading sequence $\{1, [0]^{\infty}\}$ generated by the separatrix converging to the stable focus in the phase space. (left) Combined scan using two kneading ranges, [11-61] and [26-36], reveals the structure of homoclinic bifurcations in a vicinity of the primary T-point. The scan creates an illusion that the bifurcation unfolding contains concentric circles rather than weakly converging spirals due to long lengths of the homoclinic connections. Note a saddle point separating the bifurcations curves (blueish colors) that are supposed to end up at the T-points from those flowing around it on the right and left. (right) 3D kneading scan of the [11-61]-range with the primary T-point in the deep potential dwell (at the level $K = 0$), and a saddle point. One can notice that locally, this pattern in the parameter plane resembles of a typical setup for saddle-node bifurcations.

By construction, the scans based on the kneading episodes, resp. [11-61], and combined [11-61] and [26-36] ranges, shown in Fig. 2.17, let us reveal the sought homoclinic bifurcations and the homoclinic connections of the saddle of the desired lengths. Homoclinic connections that are shorter or longer than the given range will be either represented by solid stripes, or produce "noisy" regions where the resolution (the number of the mesh points) of the scan is not good enough to expose fine details due to the abundance of data information.

Next let us examine the kneading-based scan of the dynamics of the Lorenz equation near the secondary Bykov T-point at ($r = 85, \sigma = 11.9$) shown in Fig. 2.18. Besides the focal point per se, the scan reveals a plethora of subsequent T-points corresponding to more complex

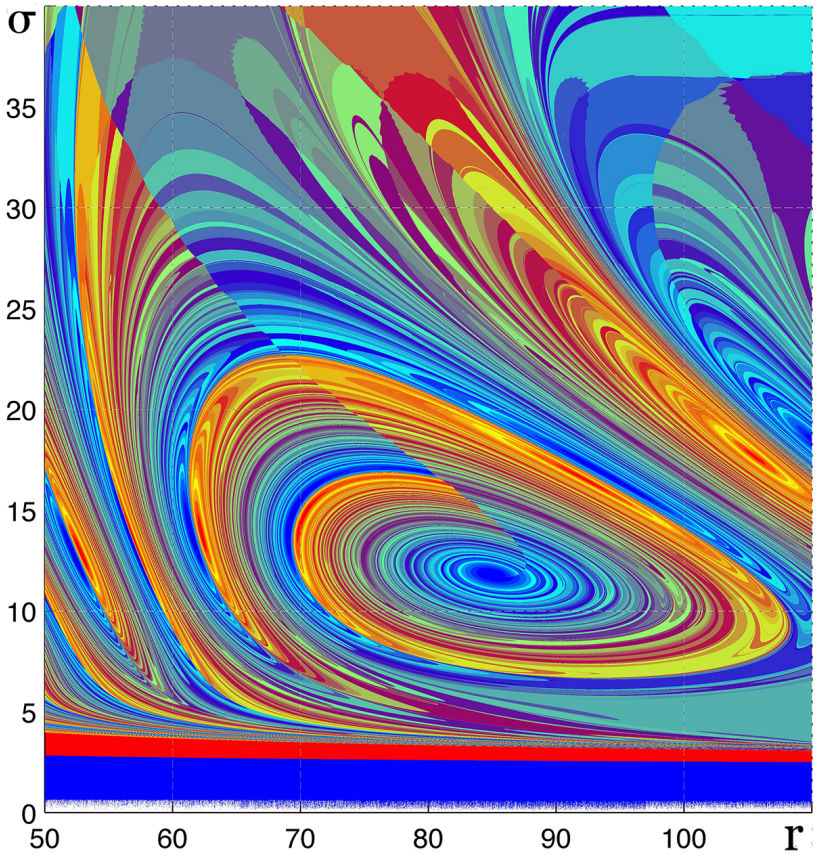

Figure (2.18) Bi-parametric sweeping of the Lorenz equation around the secondary T-point at $(r = 85, \sigma = 11.9)$ using [6-16] kneadings, revealing a plethora of subsequent T-points giving rise to self-similar fractals in the parameter space of the structurally unstable chaotic attractor.

heteroclinic connections between the saddle and saddle-foci. The complexity of the bifurcation structure of the Lorenz-like systems is a perfect illustration of the dynamical paradigm of so-called quasi-chaotic attractors introduced and developed by L.P. Shilnikov within the framework of the mathematical Chaos theory ([11],[12],[13],[14],[54]). Such a chaotic set is impossible to parameterize and hence to describe fully its multi-component structure due to dense complexity of ongoing bifurcations occurring within it. Of special interest here are a few smaller-scale spirals visibly located between the consecutive scrolls around the secondary T-point, that terminate the bifurcation curves starting from the codimension-two inclination switch bifurcations.

PART 3

ORDERED INTRICACY OF HOMOCLINIC OF THE SHILNIKOV SADDLE-FOCUS IN REFLEXION SYMMETRIC SYSTEMS

In this chapter we aim to understand the comprehensive chaotic structure of a reflexion symmetric three-dimensional system with a saddle-focus equilibrium state at the center. Such a system has countable many homoclinic orbits nearby to its primary homoclinic orbit(see [29]). Analytical results will be disclosed in the structural unfolding of the homoclinic bifurcations (HBs) and a symbolic computational tool will be applied to a Chua's circuit for a visual understanding of the theoretical results.

The example Chua's circuit used in this dissertation is:

$$\dot{x} = a(y + \frac{x}{6} - \frac{x^3}{6}), \quad \dot{y} = x - y + z, \quad \dot{z} = -by; \tag{3.1}$$

It has three equilibrium states: $O(0,0,0)$, $O_1(-1,0,1)$ and $O_2(1,0,-1)$. In the following chaotic region of the bi-parametric plane that we are interested, they are all saddle-foci. O has one dimensional unstable manifold (W^u) and two dimensional stable manifold (W^s). O_1 and O_2 are symmetric saddle-foci with one dimensional stable manifold and two dimensional unstable manifold. A rough bifurcation diagram for these equilibria can be found in figure 1 ([59]).

Unlike hyperbolic systems, the Chua's circuit undergoes abrupt transitions of different dynamical structure constantly in certain bi-parametric region due to the three saddle-foci equilibria (see [60]). This chapter will not discuss the chaos caused by the two symmetric saddle-foci because the structure is essentially the same to the Rössler system. It is devoted to the structural sensitivity due to the saddle focus at the origin. It uses 0-1 codes to name homoclinics in this paper. '1' represents the right and '0' represents the left. Due to the symmetry, there is no difference between homoclinics that start from the left or right unstable

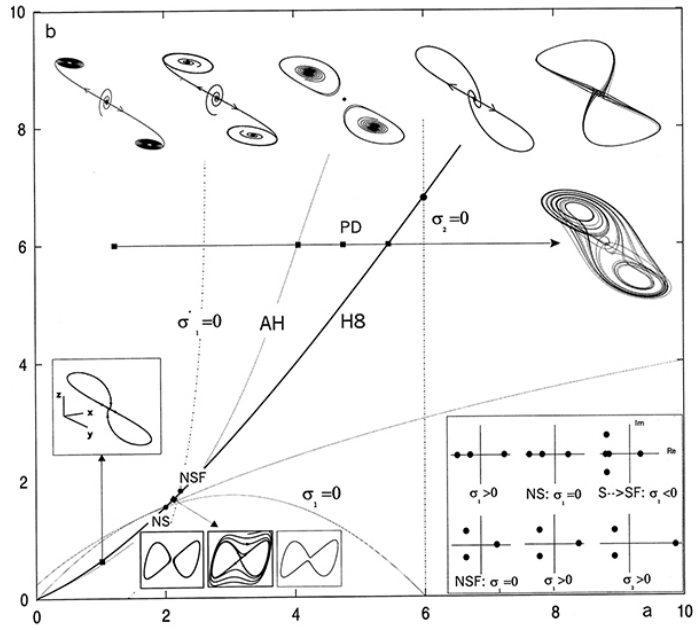

Figure (3.1) It includes Andronov-Hopf bifurcation curve of $O_{1,2}$ and resonant condition curves of equilibrium O: NS, NSF, NDSF and $S \to SF$. H8 is the primary HB curve of O. From left to right at $b = 6$, the first trajectory picture plots when $O_{1,2}$ are stable focus, the second one is the beginning of the AH bifurcation and the third one has larger asymmetric periodic orbits. The asymmetric periodic orbits becomes homoclinic loops in the fourth one and the fifth and sixth ones show the chaotic behavior after the primary homoclinic loops. At the bottom, it also shows how the trajectory structure changes when O is a saddle. Two asymmetric periodic orbit merge together and become homoclinic loops and then the two homoclinic loops bifurcate to a big symmetric periodic orbit. The homoclinic loops have figure-8 shape due to the property of reflexion symmetry of the model.

separatrix of the origin. We always initiate the trajectory from the right (or up) unstable separatrix. If the trajectory loops on the right twice and come back to the origin, we call it a $1, 1$ or right double circuit homoclinic orbit. If it loops on the right and then left and then comes back to the origin, we call it a $(1, 0)$ or left double circuit homoclinic orbit.

3.1 An analytical approach of homoclinic bifurcation (HB) structure of a Shilnikov saddle-focus in a reflexion symmetric system

In a reflexion symmetric system, the origin O is a $(2, 1)$-type Shilnikov saddle-focus. If its one-dimension unstable manifold W_O^u (made of two separatrices) makes one loop and comes

back to its stable manifold W^s_O, a homoclinic orbit is produced, called the primary homoclinic orbit. Small perturbations of parameter values can generate multi-loop homoclinic orbits if the saddle index $\nu < 1$ ([29]). We will show the embedding mechanism of HBs near the primary HB on a bi-parametric plane.

The normal form of the $\mathbb{Z}_3$ system near the saddle-focus is (following [61]).

$$\begin{aligned} \dot{x} &= -\rho(\mu)x - \omega(\mu)y + P(x, y, z, \mu), \\ \dot{y} &= \omega(\mu)x - \rho(\mu)y + Q(x, y, z, \mu), \\ \dot{z} &= \lambda(\mu)z + R(x, y, z, \mu). \end{aligned} \tag{3.2}$$

P, Q and R are smooth functions, and their first derivatives at $O(0, 0, 0)$ vanish for all μ near $\mu = 0$. A single-loop (primary) homoclinic orbit occurs at $\mu = 0$. $\rho(\mu)$, $\omega(\mu)$ and $\lambda(\mu)$ are all positive. The saddle index $\nu(\mu) = \frac{\rho(\mu)}{\lambda(\mu)} < 1$, which guarantees the system's complexity ([29]). In this normalized system, the z-axis is W^u_O and xy-plane is W^s_O. The solution of System (3.2) initiated at a point (x_0, y_0, z_0) can be written as

$$\begin{aligned} x(t) &= e^{-\rho(\mu)t}[x_0 \cos(\omega(\mu)t) - y_0 \sin(\omega(\mu)t)], \\ y(t) &= e^{-\rho(\mu)t}[y_0 \cos(\omega(\mu)t) + x_0 \sin(\omega(\mu)t)], \\ z(t) &= e^{\lambda(\mu)t} z_0. \end{aligned} \tag{3.3}$$

A sufficiently small cylinder is selected to construct a Poincaré return map using a cylinder coordinate system (r, φ, z) ([61]). $\Pi_0 : r = R(-R < z < R)$, $\Pi_1 : z = R(0 < r < R)$ and $\Pi_2 : z = -R(0 < r < R)$ (Figure 3.2). Here R is sufficiently small. When $z_0 > 0$, the mapping $T_0 : \Pi_0 \mapsto \Pi_1((\varphi_0, z_0) \mapsto (r, \theta))$ can be calculated from (3.3). Keep in mind that $x_0 = R\cos\varphi_0$, $y_0 = R\sin\varphi_0$, $x(t) = r\cos\theta$, $y(t) = r\sin\theta$ and $z(t) = R$.

$$T_0 : \quad r = R(z_0/R)^{\nu(\mu)}, \quad \theta = \varphi_0 + (\omega(\mu)/\lambda(\mu)) \ln(R/z_0). \tag{3.4}$$

Similarly when $z_0 < 0$, the mapping $T_0' : \Pi_0 \mapsto \Pi_2((\varphi_0, z_0) \mapsto (r, \theta))$ can be calculated from

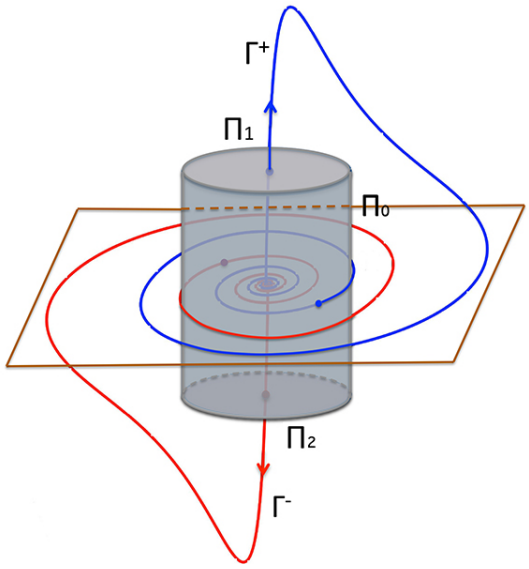

Figure (3.2) The unstable separatrices from the origin, Γ^+ and Γ^-, come back to the origin symmetrically after one loop and generate two symmetric homoclinic orbits. A small cylinder is centered at the origin. Π_1 is the top base, Π_2 is the bottom base and Π_0 is the side of the cylinder.

(3.3).

$$T_0' : r = R(-z_0/R)^{\nu(\mu)}, \quad \theta = \varphi_0 + (\omega(\mu)/\lambda(\mu)) \ln(-R/z_0).$$

The mapping $T_1 : \Pi_1 \mapsto \Pi_0$ ($(x, y) \mapsto (\varphi_0, z_0)$ or $(r\cos\theta, r\sin\theta) \mapsto (\varphi_0, z_0)$) occurs outside the cylinder and its time of flight is short, therefore T_1 can be approximated by a linear transformation.

$$T_1 : \begin{array}{c} \varphi_0 = a_1\mu + a(\mu)x + b(\mu)y = a_1\mu + A(\mu)r\cos(\theta + \alpha_1(\mu)) + O(r^2), \\ z_0 = \mu + c(\mu)x + d(\mu)y = \mu + B(\mu)r\sin(\theta + \alpha_2(\mu)) + O(r^2); \end{array} \tag{3.5}$$

where $A(0)B(0)\cos[\alpha_1(0) - \alpha_2(0)] \neq 0$ for a non-degenerate linear transformation. The mapping $T_1' : \Pi_2 \mapsto \Pi_0$ can be derived from T_1 and the reflexion symmetry. For $(x, y) \in \Pi_2$, $T_1'(x, y)$ and $T_1(-x, -y)$ are symmetric to the origin, therefore

$$T_1' : \varphi_0 = \pi + a_1\mu - A(\mu)r\cos(\theta + \alpha_1(\mu)) + O(r^2), z_0 = -\mu + B(\mu)r\sin(\theta + \alpha_2(\mu)) + O(r^2)$$

Hence when $z_0 > 0$, the return map on Π_0 is $T = T_1 \circ T_0 : \Pi_0 \mapsto \Pi_0$,

$$T: \begin{array}{c} \tilde{\varphi_0} = a_1\mu + A(\mu)R(z_0/R)^{\nu(\mu)}\cos(\varphi_0 + \frac{\omega(\mu)}{\lambda(\mu)}\ln(R/z_0) + \alpha_1(\mu)) + O(z_0^{2\nu_(\mu)}), \\ \tilde{z_0} = \mu + B(\mu)R(z_0/R)^{\nu(\mu)}\sin(\varphi_0 + \frac{\omega(\mu)}{\lambda(\mu)}\ln(R/z_0) + \alpha_2(\mu)) + O(z_0^{2\nu(\mu)}); \end{array}$$

and when $z_0 < 0$, the return map on Π_0 is $T' = T_1' \circ T_0' : \Pi_0 \mapsto \Pi_0$,

$$T': \begin{array}{c} \tilde{\varphi_0} = \pi + a_1\mu - A(\mu)R(-z_0/R)^{\nu(\mu)}\cos(\varphi_0 + \frac{\omega(\mu)}{\lambda(\mu)}\ln(-R/z_0) + \alpha_1(\mu)) + O(z_0^{2\nu_(\mu)}), \\ \tilde{z_0} = -\mu + B(\mu)R(-z_0/R)^{\nu(\mu)}\sin(\varphi_0 + \frac{\omega(\mu)}{\lambda(\mu)}\ln(-R/z_0) + \alpha_2(\mu)) + O(z_0^{2\nu(\mu)}). \end{array}$$

Let $A_0 = A(0)$, $B_0 = B(0)$, $\Omega_0 = \omega(0)/\lambda(0)$, $\nu_0 = \nu(0)$, $\phi_1 = -\alpha_1(0) - \Omega_0 \ln R$ and $\phi_2 = -\alpha_2(0) - \Omega_0 \ln R$. If we keep the dominant terms only, the maps can be simplified as

$$T: \begin{array}{c} \tilde{\varphi_0} = a_1\mu + A_0 R^{1-\nu_0} z_0^{\nu_0}\cos(\Omega_0 \ln z_0 + \phi_1 - \varphi_0) + O(z_0^{2\nu_0}), \\ \tilde{z_0} = \mu - B_0 R^{1-\nu_0} z_0^{\nu_0}\sin(\Omega_0 \ln z_0 + \phi_2 - \varphi_0) + O(z_0^{2\nu_0}). \end{array} \tag{3.6}$$

and

$$T': \begin{array}{c} \tilde{\varphi_0} = \pi + a_1\mu - A_0 R^{1-\nu_0}(-z_0)^{\nu_0}\cos(\Omega_0 \ln(-z_0) + \phi_1 - \varphi_0) + O(z_0^{2\nu_0}), \\ \tilde{z_0} = -\mu - B_0 R^{1-\nu_0}(-z_0)^{\nu_0}\sin(\Omega_0 \ln(-z_0) + \phi_2 - \varphi_0) + O(z_0^{2\nu_0}). \end{array} \tag{3.7}$$

A homoclinic orbit that passes l times through Π_0 is called an l-loop homoclinic orbit, while one with 2 or 3 passes is called a double-loop or a triple-loop homoclinic orbit respectively. If a pass through Π_0 is on the $z > 0$ part, the symbol 1 is assigned, in the case of $z < 0$, the symbol 0 is used. For example, a homoclinic orbit that passes 2 times through Π_0 with $z > 0$ is called a $(1, 1)$ or alternatively right double-loop homoclinic orbit.

3.1.1 $(1, 1)$ or right double-loop homoclinic bifurcation

The right or positive unstable separatrix Γ^+ makes one loop on the right and intersects Π_0 at $(\varphi_0, z_0) = (a_1\mu, \mu)$. If $\mu > 0$, the next loop will be on the right also and according to

the map (3.6), the next intersection point of Γ^+ on Π_0 is

$$\begin{aligned} \varphi_1 &= a_1\mu + A_0 R^{1-\nu_0}\mu^{\nu_0}\cos(\Omega_0 \ln\mu + \phi_1) + O(\mu^{2\nu_0}), \\ z_1 &= \mu - B_0 R^{1-\nu_0}\mu^{\nu_0}\sin(\Omega_0 \ln\mu + \phi_2) + O(\mu^{2\nu_0}), \end{aligned} \tag{3.8}$$

where the term $\varphi_0 = a_1\mu$ is small and omitted.

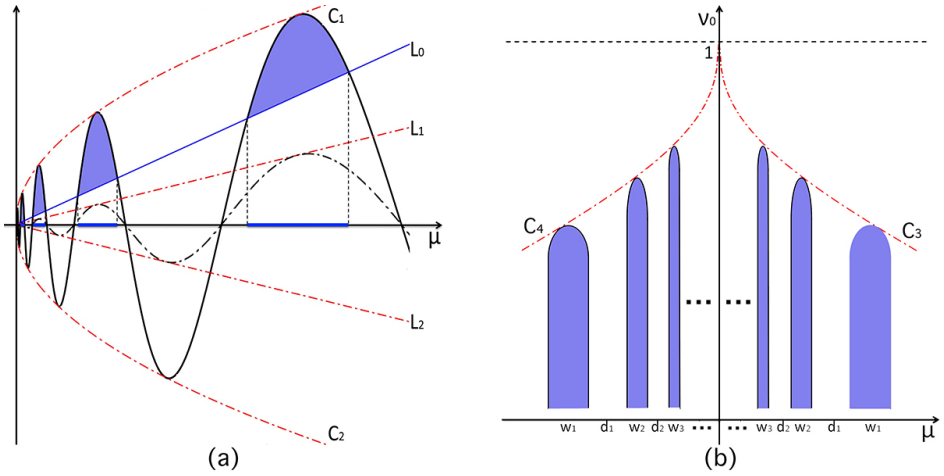

Figure (3.3) (a) $z_1 < 0$ on the parts that the sine function is above the line L_0. The union of the projections of those parts on the μ-axis is the range of μ such that $z_1 < 0$. The endpoints of the intervals are the μ values generating right double-loop homoclinic orbits. When $\nu_0 \to 1$, the amplitude boundary of the sine function $C_{1,2}$ collapses to the two lines $L_{1,2}$ and the blue intervals vanish.(b) The plot sketches the regions of $z_1 < 0$ on (μ, ν_0) plane. The outlines of the blue bars on the $\mu > 0$ side are the $(1,1)$ double-loop HBs. The outlines of the blue $\cap$-bars on the $\mu < 0$ side are the $(1,0)$ double-loop HBs. The blue bars vanish above the curves $C_{3,4}$. The width of the blue bars are w_1, w_2, $\cdots$ respectively. The distance between the consecutive blue bars are d_1, d_2, $\cdots$ respectively.

A $(1,1)$ double-loop homoclinic orbit is produced when $z_1 = 0$, i.e.

$$\mu + O(\mu^{2\nu_0}) = B_0 R^{1-\nu_0}\mu^{\nu_0}\sin(\Omega_0 \ln\mu + \phi_2). \tag{3.9}$$

It is equivalent to

$$\mu^{1-\nu_0} + O(\mu^{\nu_0}) = B_0 R^{1-\nu_0}\sin(\Omega_0 \ln\mu + \phi_2). \tag{3.10}$$

Because μ is sufficiently small and $\nu_0 < 1$, $B_0 R^{1-\nu_0} \sin(\Omega_0 \ln(\mu) + \phi_2) = 0$ approximately. The solutions are $\mu_1^{(n)} = e^{-\frac{2n\pi}{\Omega_0} - \frac{\phi_2}{\Omega_0}}$ and $\mu_2^{(n)} = e^{-\frac{2n\pi}{\Omega_0} \pm \frac{\pi}{\Omega_0} - \frac{\phi_2}{\Omega_0}}$ for a sufficiently large n. In this expression, a '+' is taken when $B_0 > 0$ and a '-' is taken when $B_0 < 0$. Without loss of generality, $B_0 > 0$ is assumed. Noticing that $z_1 < 0$ for $\mu \in (\mu_1^{(n)}, \mu_2^{(n)})$, Γ^+ goes to the left after the first right loop and therefore no right multi-loop HB exists if $\mu \in (\mu_1^{(n)}, \mu_2^{(n)})$. The regions such that $z_1 < 0$ are painted blue in Figure 3.3(b) and 3.4(b). They are parallel bars on the (μ, ν_0)-plane. The outlines of the bars are the $(1, 1)$ double-loop HBs. The width and the distance of the bars, $w_n = \mu_2^{(n)} - \mu_1^{(n)}$ and $d_n = \mu_1^{(n)} - \mu_2^{(n-1)}$, decrease when $n \to \infty$ ($\mu \to 0$), with ratios $\frac{w_{n+1}}{w_n} = \frac{\mu_2^{(n+1)} - \mu_1^{(n+1)}}{\mu_2^{(n)} - \mu_1^{(n)}} = e^{-\frac{2\pi}{\Omega_0}}$ and $\frac{d_{n+1}}{d_n} = \frac{\mu_1^{(n+1)} - \mu_2^{(n)}}{\mu_1^{(n)} - \mu_2^{(n-1)}} = e^{-\frac{2\pi}{\Omega_0}}$ (Figure 3.3(b) and 3.4(b)). Hence the width and the distance of the bars decrease exponentially when approaching the primary HB (the line $\mu = 0$ on the (μ, ν_0)-plane).

When $\nu_0 \to 1$, the term $\mu^{1-\nu_0}$ is becoming significant in Equation (3.10) and no longer negligible. $\mu^{1-\nu_0} = B_0 R^{1-\nu_0} \sin(\Omega_0 \ln \mu + \phi_2)$ and equivalently $\mu = B_0 R^{1-\nu_0} \mu^{\nu_0} \sin(\Omega_0 \ln \mu + \phi_2)$ is used for the calculation of $z_1 = 0$. $z_1 = 0$; therefore, right double-loop homoclinic orbits exist at the intersections of the sine function $y = B_0 R^{1-\nu_0} \mu^{\nu_0} \sin(\Omega_0 ln\mu + \phi_2)$ and the line $L_0 : y = \mu$ in Figure 3.3(a) and 3.4(a). The union of the blue intervals is the range of μ such that $z_1 < 0$ for a constant ν_0. When $\nu_0 \to 1$, the amplitude boundary of the sine function, $C_{1,2} : \pm B_0 R^{1-\nu_0} \mu^{\nu_0}$ collapses to the two lines $L_{1,2} : \pm B_0 \mu$ eventually.

If $B_0 < 1$, the blue intervals will shrink and disappear after the local maximums of the sine function become lower than the line L_0 (Figure 3.3(a)). The closer the interval is to $\mu = 0$, the larger value of ν_0 is needed for the interval to vanish. The corresponding region of such a blue interval is a blue bar on the (μ, ν_0)-plane that terminates when $\mu = B_0 R^{1-\nu_0} \mu^{\nu_0}$, i.e., $\nu_0 = 1 - \frac{\ln B_0}{\ln \mu - \ln R}$ that is the red dash curve C_3 in Figure 3.3(b). The C_3 curve is less than 1 and approaches to 1 when $\mu \to 0$. Such a bar that terminates before reaching the horizontal line $\nu_0 = 1$ is called a $\cap$-bar in this letter. If $B_0 > 1$, the intervals are getting narrower when $\nu_0 \to 1$ but they are not disappearing (Figure 3.4(a)). On the (μ, ν_0)-plane, the $z_1 < 0$ region is a union of blue bars that are not terminated when $\nu_0 \to 1$ (Figure 3.4(b)). We call those blue bars Π-bars in this dissertation.

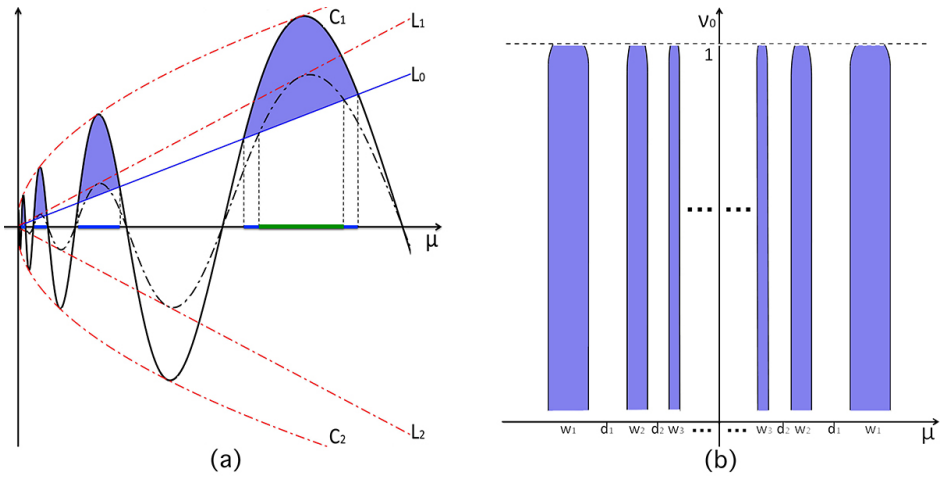

Figure (3.4) (a) $z_1 < 0$ on the parts that the sine function is above the line L_0. The union of the projections of those parts on the μ-axis is the range of μ such that $z_1 < 0$.. The endpoints of the intervals are the μ values generating right double-loop homoclinic orbits. When $\nu \to 1$, the amplitude boundary of the sine function $C_{1,2}$ collapses to the two lines $L_{1,2}$ and the blue intervals are shortened to the green intervals. (b) The plot sketches the regions of $z_1 < 0$ on the (μ, ν_0) plane. The outlines of the blue Π-bars on the $\mu > 0$ side are the $(1,1)$ double-loop HBs. The outlines of the blue bars on the $\mu < 0$ side are the $(1,0)$ double-loop HBs. The width of the blue bars are w_1, w_2, $\cdots$ respectively. The distance between the consecutive blue bars are d_1, d_2, $\cdots$ respectively.

3.1.2 $(1,0)$ or left double-loop homoclinic bifurcation

When Γ^+ makes one loop on the right and intersects Π_0 at $(\varphi_0, z_0) = (a_1\mu, \mu)$ with $\mu < 0$, it must make the second loop on the left. Then it intersects Π_0 for the second time, presumably at the point (φ_1, z_1), which can be found by the map (3.7).

$$\begin{aligned} \varphi_1 = &\quad \pi + a_1\mu - A_0 R^{1-\nu_0}(-\mu)^{\nu_0}\cos(\Omega_0 \ln(-\mu) + \phi_1) + O((-\mu)^{2\nu_0}), \\ z_1 = &\quad -\mu - B_0 R^{1-\nu_0}(-\mu)^{\nu_0}\sin(\Omega_0 \ln(-\mu) + \phi_2) + O((-\mu)^{2\nu_0}). \end{aligned} \tag{3.11}$$

When $z_1 = 0$, i.e. $-\mu + O((-\mu)^{2\nu_0}) = B_0 R^{1-\nu_0}(-\mu)^{\nu_0}\sin(\Omega_0 \ln(-\mu) + \phi_2)$, a $(1,0)$ double-loop homoclinic orbit is produced. It is exactly the same with the case of (1,1) double-loop homoclinic if replacing μ by $-\mu$. Therefore, the structure of (1,0) double-loop HBs is symmetric with the one of (1,1) double-loop HBs, as shown in Figure 3.3(b) and 3.4(b).

Theorem 3.1.1 *Let a reflexion symmetric system has a pair of homoclinic loops to the Shilnikov saddle-focus with $\nu(\mu) < 1$ at $\mu = 0$, i.e. $\nu_0 < 1$. Then, double-loop homoclinics occur at values*

$$|\mu| = B_0 R^{1-\nu_0} |\mu|^{\nu_0} \sin(\Omega_0 \ln |\mu| + \phi_2)$$

where B_0 and $R > 0$ are constants. If $B_0 < 1$, then double-loop HBs are ended up by the curve $\nu_0 = 1 - \frac{\ln B_0}{\ln|\mu| - \ln R}$ in the (μ, ν_0)-plane. The latter curve converges to 1 when $\mu \to 0$. All double-loop HBs accumulate to the primary one from both sides with a scalability ratio $e^{-\frac{2\pi}{\Omega_0}}$ for both the width and distance between the bifurcation curves corresponding to successive homoclinics.

3.1.3 $(1, 1, 1)$ or right triple-loop homoclinic bifurcation

When the right unstable separatrix Γ^+ makes three loops on the right and then intersects W^s, a $(1, 1, 1)$ or right triple-loop homoclinic orbit is produced. The mapping with the dominant terms only is

$$\begin{aligned} z_1 = &\quad \mu - B_0 R^{1-\nu_0} \mu^{\nu_0} \sin(\Omega_0 \ln \mu + \phi_2) + O(\mu^{2\nu_0}), \\ z_2 = &\quad \mu - B_0 R^{1-\nu_0} z_1^{\nu_0} \sin(\Omega_0 \ln z_1 + \phi_2) + O(z_1^{2\nu_0}). \end{aligned} \tag{3.12}$$

Equations of φs are omitted. For finding $(1, 1, 1)$ triple-loop HBs, we are seeking the range of μ such that $z_2 < 0$.

System (3.12) implies $z_1 \sim \mu^{\nu_0}$. Therefore z_1 is small when μ is small. The second equation can be reduced to $sin(\Omega_0 ln z_1 + \phi_2) = 0$ assuming μ is small enough, i.e. $z_1 = e^{-\frac{2m\pi}{\Omega_0} - \frac{\phi_2}{\Omega_0}}$ or $e^{-\frac{2m\pi}{\Omega_0} + \frac{\pi}{\Omega_0} - \frac{\phi_2}{\Omega_0}}$ ($m \in \mathbb{Z}$ and large enough). Notate I_m as the interval of z_1 such that $z_2 < 0$, which is deduced from the m-th period of the sine function, then $I_m \approx (e^{-\frac{2m\pi}{\Omega_0} - \frac{\phi_2}{\Omega_0}}, e^{-\frac{2m\pi}{\Omega_0} + \frac{\pi}{\Omega_0} - \frac{\phi_2}{\Omega_0}})$ ($m \in \mathbb{N}$ and sufficiently large). To be more precise, the small term μ can be considered for the calculation of I_m. An example of I_m is illustrated in Figure 3.5 for a fixed μ value. It is the green interval on the z_1-axis projected from the m-th period of the sine function that is greater than μ. Assume that D_m is the local maximum of the m-th period of the dash sine function $y = B_0 z_1 \sin(\Omega_0 \ln z_1 + \phi_2)$. If $D_m < \mu$, I_m shrinks and

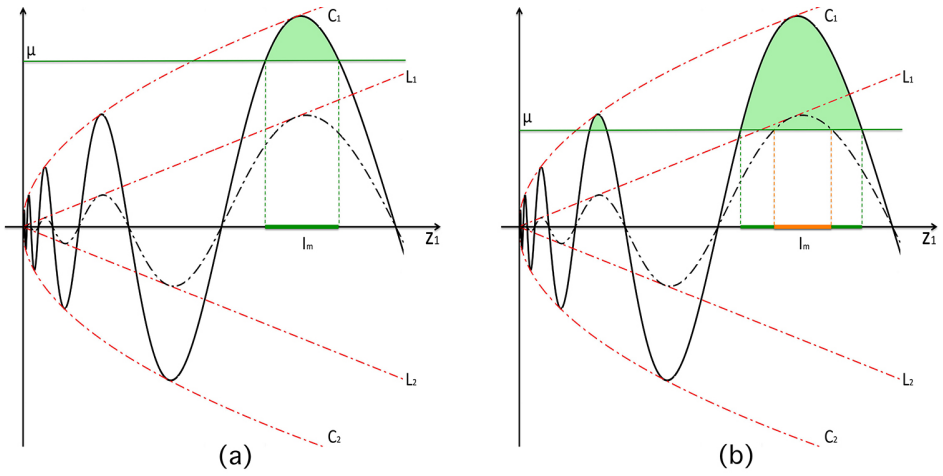

Figure (3.5) The solid sine function is $y = B_0 R^{1-\nu_0} z_1^{\nu_0} \sin(\Omega_0 \ln z_1 + \phi_2)$ bounded by curves $C_{1,2}$. The dashed sine function is $y = B_0 z_1^{\nu_0} \sin(\Omega_0 \ln z_1 + \phi_2)$ bounded by the lines $L_{1,2}$. The projection of the part of the solid sine function that is above the line $y = \mu$ is painted green. (a) The dashed sine function is completely under the horizontal line $y = \mu$. (b) The dashed sine function has a part that is above $y = \mu$ and the projection of it on the z_1-axis is painted orange.

vanishes when $\nu_0 \to 1$ (Figure 3.5(a)). If $D_m > \mu$, I_m narrows down to the orange interval eventually but doesn't vanish when $\nu_0 \to 1$ (Figure 3.5(b)).

The case of $B_0 < 1$ will be discussed first. The first equation in System (3.12) can be written as $\mu - z_1 = B_0 R^{1-\nu_0} z_1^{\nu_0} \sin(\Omega_0 \ln z_1 + \phi_2) + O(z_1^{2\nu_0})$. The right hand side function is the sine function in Figure 3.6(a). Its parts above L_0, painted in blue, are the same ones in Figure 3.3 and the boundaries of the blue bars in Figure 3.6(b) are the $(1,1)$ double-loop HBs as we discussed in the section 2.1. It is sufficient to discuss triple-loop HBs only on one period of the sine function $y = B_0 R^{1-\nu_0} \mu^{\nu_0} \sin(\Omega_0 \ln \mu + \phi_2)$. The chosen period is AB in Figure 3.6(a), the n-th period $\mu \in (e^{-\frac{2n\pi}{\Omega_0} - \frac{\pi}{\Omega_0} - \frac{\phi_2}{\Omega_0}}, e^{-\frac{2n\pi}{\Omega_0} + \frac{\pi}{\Omega_0} - \frac{\phi_2}{\Omega_0}})$. Assume that period has a local minimum m_n at μ_{min} and a local maximum M_n at μ_{max}. When the amplitude boundary curves $C_{1,2}$ collapse to $L_{1,2}$ at $\nu_0 = 1$, the new local minimum and maximum of that period are denoted as m_n' and M_n'. Without designation, the sine function we mention below has this n-th period only. The right triple-loop HBs are drawn between two blue bars, a_n and a_{n+1}, in Figure 3.6(b). The same or similar right triple-loop HBs structure can be found

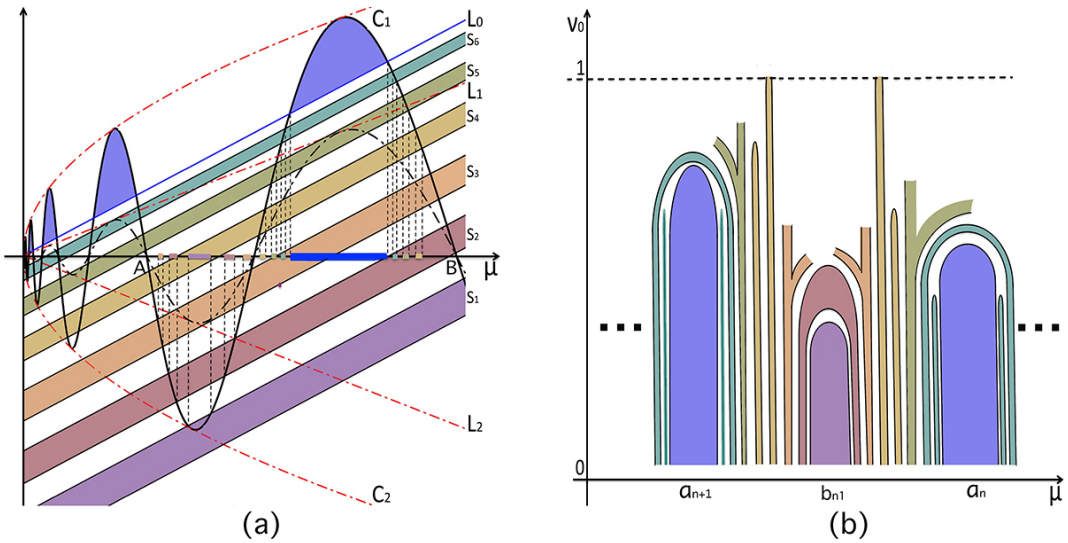

Figure (3.6) $B_0 < 1$. (a) The sine function is $y = B_0 R^{1-\nu_0}\mu^{\nu_0}\sin(\Omega_0 \ln\mu + \phi_2)$ bounded by $C_{1,2} : y = \pm B_0 R^{1-\nu_0}\mu^{\nu_0}$. The dashed sine function is $y = B_0\mu\sin(\Omega_0 \ln\mu + \phi_2)$ bounded by $L_{1,2} : y = \pm B_0\mu$. The interceptions of the strips $S_1 - S_6$ and the sine function are projected to the μ-axis. The strips are parallel to the line $L_0 : y = \mu$. The closer a strip is to L_0, the narrower it is. (b) Two blue $(1,1)$ double-loop $\cap$-bars, a_n and a_{n+1} are drawn in the $\mu - \nu_0$ plane. The $(1,1,1)$ triple-loop pieces fit in between and match the color of the strips in the plot (a) that they are derived from. Close to the blue bar, there are a pair of $\cap$-bars and a bridge that are derived from the strip S_6 in the plot (a). Then there is a pair of "Y" shapes that are derived from the strip S_5. Then there are a pair of yellow $\cap$-bars and a pair of Π-bars that are derived from the strip S_4. Then there is a "Y" shape pair again that is derived from S_3. Then there is a reddish bridge that is derived from S_2. At the very middle of the two blue bars, there is a purple $\cap$-bar b_{n1} that is the widest triple-loop piece. The closer to the blue bar, the narrower the triple-loop piece is. Taking b_{n1} as the center, the left pieces are slightly narrower than the right pieces.

between any other two consecutive blue bars. Recall that $z_2 < 0$ when $z_1 \in I_m$ ($m \in \mathbb{N}$ and sufficiently large), therefore the range of μ such that $z_2 < 0$ is the projection of the interception of $y = \mu - I_m$ and $y = B_0 R^{1-\nu_0}\mu^{\nu_0}\sin(\Omega_0 \ln\mu + \phi_2)$ on the μ-axis. $y = \mu - I_m$ is a strip bounded by two parallel lines for $m \in \mathbb{N}$ and large enough.

All those strips line up under and accumulate to L_0 as m increases. They are getting narrower when approaching L_0, noticing that $\frac{|I_{m+1}|}{|I_m|} = e^{-\frac{2\pi}{\Omega_0}}$. Actually the two boundary lines of each strip are not exactly parallel, I_m is μ related and it can shrink and disappear if we consider the negligible small terms as we discussed earlier. They are considered approx-

imately parallel. Six sample strips $S_1 - S_6$ are chosen and sketched in Figure 3.6(a). The distinct and complete $(1, 1, 1)$ triple-loop HBs can be derived from them. They are painted with different colors for distinction.

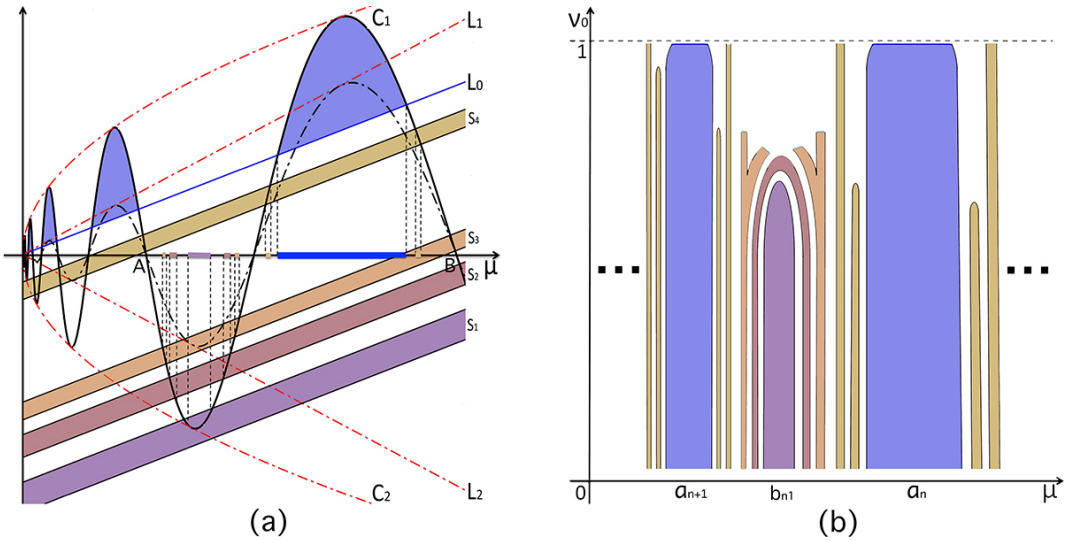

Figure (3.7) $B_0 > 1$. (a) The sine function is $y = B_0 R^{1-\nu_0} \mu^{\nu_0} \sin(\Omega_0 \ln \mu + \phi_2)$ bounded by $C_{1,2} : y = \pm B_0 R^{1-\nu_0} \mu^{\nu_0}$. The dashed sine function is bounded by $L_{1,2} : y = \pm B_0 \mu$. The interceptions of the strips $S_1 - S_4$ and the sine function is projected to the μ-axis. The strips are parallel to the line $L_0 : y = \mu$. The closer a strip is to L_0, the narrower it is. (b) Two blue $(1, 1)$ double-loop bars, a_n and a_{n+1} are drawn on the (μ, ν_0)-plane. The $(1, 1, 1)$ triple-loop bars fit in between and match the color of the strips in the plot (a) that they are derived from. We describe it in the order from the close region of a blue bar to its furthest. Close to the blue bar, there are a pair of yellow $\cap$-bars and a pair of yellow Π-bars that are derived from the strip S_4. Then there is a pair of "Y" shapes that are derived from S_3. Then there is a reddish bridge that is derived from S_2. In the middle of the two blue bars, there is a purple $\cap$-bar b_{n1} that is the widest triple-loop piece. The closer to the blue bar, the narrower the triple-loop piece is. Taking b_{n1} as the center, the left pieces are slightly narrower than the right pieces.

The purple strip S_1 is the very first one that intercepts with the sine function. The projection of this interception on the μ-axis, say p_1, is an interval of μ such that $z_2 < 0$ for a constant ν_0. It is located more or less in the middle of the two blue intervals. When $\nu_0 \to 1$, the amplitude curve $C_{1,2}$ is collapsing to $L_{1,2}$ and p_1 shrinks and vanishes. The 2D picture of p_1 on the $\mu - \nu_0$ plane is the purple $\cap$-bar, say b_{n1}, located more or less in

the middle of the two blue bars, a_n and a_{n+1}, in Figure 3.6(b). In the case of S_2 or S_6, $m_n < (\mu - I_m)|_{\mu=\mu_{min}} < m'_n$ or $M'_n < (\mu - I_m)|_{\mu=\mu_{max}}$. We have two interception parts that will merge to one and then disappear when the sine function moves away from S_2 or S_6 (Figure 3.6(a)). The corresponding region in Figure 3.5(b) is the red bridge on the top of b_{n1}, say b_{n2}, generated by S_2, or the green bridge on the top of the blue bars, say b^1_{n6}, generated by S_6. There can be more than one b_{n2} or b^1_{n6} bridges if there are more than one strip that fit the conditions. Besides, S_6 can generate green $\cap$-bars inside the green bridges, say b^2_{n6} as in Figure 3.6(b) if it is so close to L_0 that the strip is narrow enough to shrink and vanish before the two parts meet and form a bridge when $\nu_0 \to 1$. If $m'_n < (\mu - I_m)|_{\mu=\mu_{min}}$ and $(\mu - I_m)|_{\mu=\mu_{max}<M'_n}$, like S_4 in Figure 3.6(a), the two interception parts do not merge. They generate the yellow bars, either a Π-bar (b^1_{n4}) or a $\cap$-bar (b^2_{n4}), on the (μ, ν_0) plane (Figure 3.6(b)). They can be Π-bars or $\cap$-bars because the width of the strip or equivalently the width of I_m can be smaller but non-zero as in Figure 3.5(b) or vanish as in Figure 3.5(a) when $\nu \to 1$. A narrower strip has a higher chance to shrink and vanish, therefore the yellow $\cap$-bar is located closer to the blue double-loop bars. If m'_n or M'_n is inside a strip, like S_3 or S_5, two of the interception parts with the sine function will merge when the minimum or maximum of the sine function drop inside S_3 and S_5. In the meantime, S_3 and S_5 are shrinking when $\nu_0 \to 1$. Therefore there is a chance that the extreme points are released from S_3 or S_5 and each of the bridges breaks down to two bars again. The corresponding object in the figure 3.6(b) is the pair of orange "Y" shapes generated by S_3, say b_{n3}, or the pair of greenish "Y" shapes generated by S_5, say b_{n5}. Both branches are left open because they can end in different manners. A branch of one "Y" can meet with the symmetric branch of the symmetric "Y" and form a bridge, or they may terminate before meeting. The other branch is Π-shaped ($\cap$-shaped) if the yellow bar next to it is a Π-bar (a $\cap$-bar). The "Y" shape can be considered as a transition stage of a bridge and a bar. And it is easy to see that there can be only one or zero "Y" shape generated in each case of S_3 and S_5. We call $b_{n1} - b_{n6}$ $(1, 1, 1)$ triple-loop pieces. One or more of them can be missing from the picture in Figure 3.6(b) if there is no strip located in the corresponding position in Figure 3.6(a). For

example, b_{n1} can be missing if the first strip that intercepts the sine function has a position like the strip S_2 instead of S_1. Another example is S_4. If the relative positions of μ and the z_1 sine function of all S_4 strips are as Figure 3.5(b), b^2_{n4} type bars will not be in Figure 3.6(b).

The width of a triple-loop piece in Figure 3.6(b) is larger if it is further from the blue bars a_n and a_{n+1} because the width of the corresponding strip is larger. b_{n1} is significantly larger than the others if it exits because S_1 intercepts the sine function at one of its flattest parts. Actually, after taking the derivative of the sine function $y = B_0 R^{1-\nu_0}\mu^{\nu_0}\sin(\Omega_0 \ln\mu + \phi_2)$, we have

$$\frac{dy}{d\mu} = \frac{N_2}{\mu^{1-\nu_0}}\sin(\Omega_0 \ln\mu + \phi_2 + \theta_0) \tag{3.13}$$

where $N_2 = B_0 R^{1-\nu_0}\sqrt{\nu_0^2+\Omega_0^2}$ and $cos\theta_0 = \nu_0/\sqrt{\nu_0^2+\Omega_0^2}$. For a fixed $\nu_0 < 1$, $\frac{dy}{d\mu}$ is very large because μ is small. And therefore the sine function is nearly made of vertical lines except for the small neighborhoods around the extreme points of the sine function $y = B_0 R^{1-\nu_0}\mu^{\nu_0}\sin(\Omega_0 \ln\mu + \phi_2)$. The interception region of S_1 and the sine function is one of these neighborhoods. Therefore the width of b_{n1} is significantly large compared to all the other triple-loop pieces.

On the other hand, the width of a $(1,1,1)$ triple-loop piece should be relatively larger if the corresponding μ value is larger because $\frac{dy}{d\mu}$ is smaller, therefore in Figure 3.6(b) the pieces on the right of b_{n1} are slightly wider than the symmetric pieces on the left of b_{n1}. In conclusion, the very middle one that is the furthest from a_n and a_{n+1}, the purple bar b_{n1} in Figure 3.6(b), has the largest width. In a real structure sweeping, the purple bar or the reddish bridge if the purple bar does not exist, might be the only visible $(1,1,1)$ triple-loop piece. All the others might be too slim to be seen. The boundaries of all the $(1,1,1)$ triple-loop pieces on the (μ,ν_0)-plane are $(1,1,1)$ triple-loop HBs.

Figure 3.7 sketches feature plots to find the region of $z_2 < 0$ and therefore the $(1,1,1)$ triple-loop HBs when $B_0 > 1$. The figure does not have S_5 and S_6 strips and their corresponding HB pieces, the bridges that are on the top of a_n and a_{n+1}, and the transitional "Y" shape. The rest of the story is the same as the case of $B_0 < 1$.

3.1.4 $(1,0,0)$ or left triple-loop homoclinic bifurcation

If the right unstable separatrix Γ^+ makes one loop on the right and then two loops on the left, then intersects W^s of the origin, a $(1,0,0)$ or left triple-loop orbit is produced. The mapping with the dominant terms only is

$$\begin{aligned} z_1 = &\quad -\mu - B_0 R^{1-\nu_0}(-\mu)^{\nu_0}\sin(\Omega_0 \ln(-\mu) + \phi_2) + O((-\mu)^{2\nu_0}), \\ z_2 = &\quad -\mu + B_0 R^{1-\nu_0}(-z_1)^{\nu_0}\sin(\Omega_0 \ln(-z_1) + \phi_2) + O((-z_1)^{2\nu_0}), \end{aligned} \tag{3.14}$$

where $\mu < 0$. Equations of φs are omitted. As in all other cases, we are looking for the range of μ such that $z_2 < 0$ for a fixed ν_0. When ν_0 varies, we have $z_2 < 0$ regions on the (μ, ν_0)-plane. Their boundaries are the $(1,0,0)$ triple-loop HBs.

System (3.14) implies $-z_1 \sim (-\mu)^{\nu_0}$, therefore it is small when $-\mu$ is small. The second equation can be simplified to $sin(\Omega_0 ln(-z_1)+\phi_2) = 0$ when the small term $-\mu$ is omitted, i.e. $-z_1 = e^{-\frac{2m\pi}{\Omega_0}-\frac{\phi_2}{\Omega_0}}$ or $e^{-\frac{2m\pi}{\Omega_0}-\frac{\phi_2}{\Omega_0}+\frac{\pi}{\Omega_0}}$ ($m \in \mathbb{Z}$ and large enough). The interval I_m of $-z_1$ such that $z_2 < 0$, that derived from the m-th period of the sine function, is $(e^{-\frac{2m\pi}{\Omega_0}-\frac{\phi_2}{\Omega_0}}, e^{-\frac{2m\pi}{\Omega_0}-\frac{\phi_2}{\Omega_0}+\frac{\pi}{\Omega_0}})$ approximately. As we discussed in the section 2.3, I_m is actually μ related if we consider the negligible small term μ. The length of I_m can decrease to zero (Figure 3.5(a)) or decrease to a smaller number (Figure 3.5(b)) when $\nu_0 \to 1$.

The case of $B_0 > 1$ is discussed first. The first equation of System (3.14) can be written as $-\mu - z_1 = B_0 R^{1-\nu_0}(-\mu)^{\nu_0}\sin(\Omega_0 \ln(-\mu)+\phi_2)+O((-\mu)^{2\nu_0})$. The right hand side is the sine function of $-\mu$ in Figure 3.8(a) with setting $-\mu$ as the x-axis. Its parts above $L_0 : y = -\mu$, painted in blue, lead to the $(1,0)$ double-loop HBs and have been discussed in the section 2.1. Recall that $z_2 < 0$ when $-z_1 \in I_m$ ($m \in \mathbb{Z}$ and large enough), therefore the range of μ such that $z_2 < 0$ is the projection of the interception of $y = (-\mu) + I_m$ ($m \in \mathbb{Z}$ and large enough) and $y = B_0 R^{1-\nu_0}(-\mu)^{\nu_0}\sin(\Omega_0 \ln(-\mu) + \phi_2)$ on the $(-\mu)$-axis. For each m, $y = (-\mu) + I_m$ is a strip above and parallel to the line L_0. The domain of $-\mu$ such that $z_2 < 0$ is the projection of the interceptions of all such strips and the sine function on the $(-\mu)$-axis. The structure study only need to be done on one of the blue regions (Figure

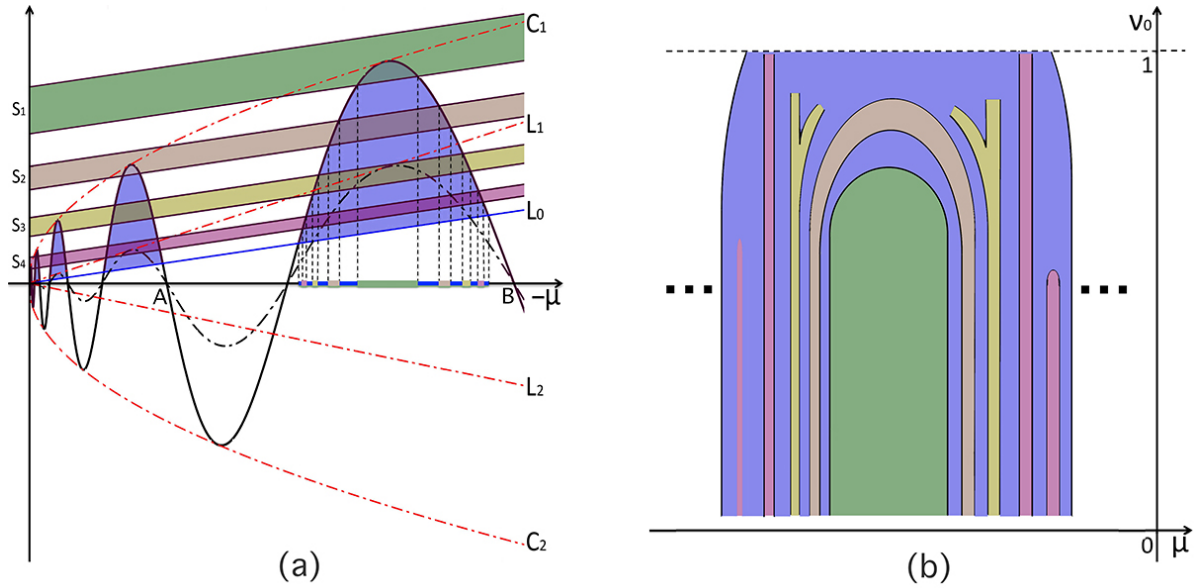

Figure (3.8) $B_0 > 1$. (a) The x-axis is $(-\mu)$-aixs. The solid sine function is bounded by two curves $C_{1,2}$ and the dashed sine function is bounded by two lines $L_{1,2}$. The parts below solid sine function and above the line L_0 are painted blue. Four strips $S_1 - S_4$ line up above L_0. Their interceptions with the solid sine function are projected to the $(-\mu)$-axis. (b) Inside the blue Pi-bar, $(1, 0, 0)$ triple-loop pieces are drawn to match the strips in the plot (a) that they are derived from. From the middle to the both sides of the blue bar, it lists a green bar, a brown bridge, a pair of yellow "Y" pieces, a pink Pi-bar and a pink $\cap$-bar. The width of the green bar in the middle is much larger than the rest. The width of the pieces is decreasing from the middle green bar to the side boundaries of the blue bar. The pieces on the right of the green bar are slightly wider than the pieces on the left.

3.8). Four sample strips $S_1 - S_4$ are picked in Figure 3.8(a) for the distinct and complete study of the $(1, 0, 0)$ triple-loop HBs. The interception of the strip S_1 and the sine function projects an interval on the $(-\mu)$-axis that vanishes when $\nu_0 \to 1$. Its two dimensional plot on (μ, ν_0)-plane is a $\cap$-bar in the middle of the blue Π-bar, painted in green, in Figure 3.8(b). The brown strip S_2 is above the maximum of the dashed sine function. Therefore, the two interception parts will merge and then vanish when $\nu_0 \to 1$. It forms the brown bridge in Figure 3.8(b). The maximum of the dashed sine function is inside the strip S_3 and, therefore, there is a chance to produce a pair of "Y" shapes inside the blue bar (Figure 3.8(b)). The pink strip S_4 is under the maximum of the dashed sine function. Its two interception parts

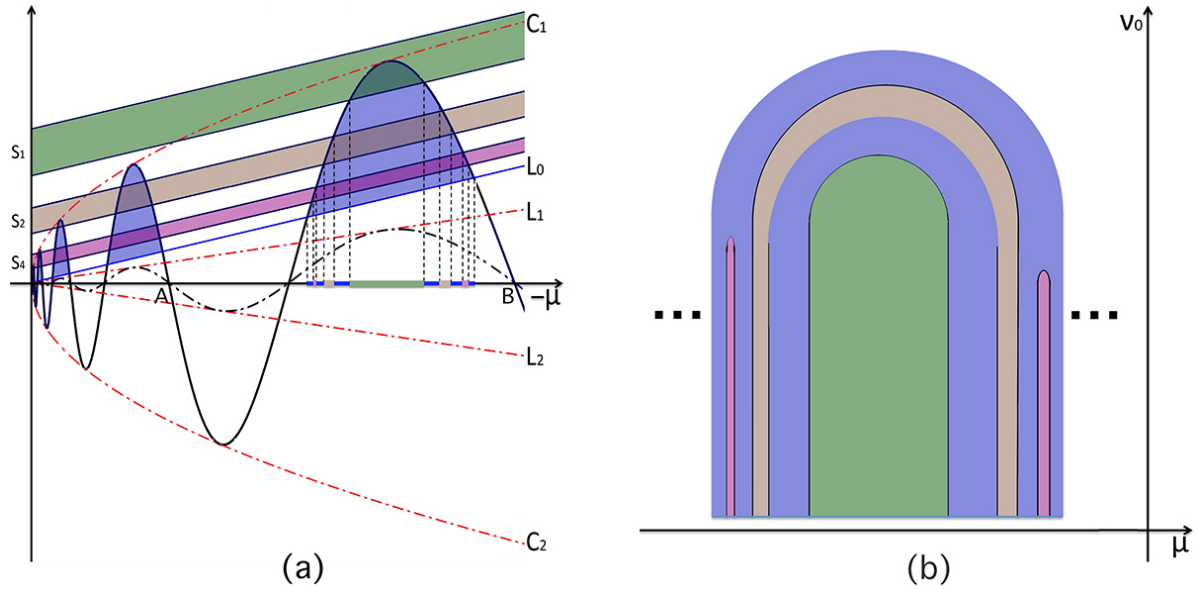

Figure (3.9) $B_0 < 1$. (a) The x-axis is $(-\mu)$-aixs. The solid sine function is bounded by two curves $C_{1,2}$ and the dashed sine function is bounded by two lines $L_{1,2}$. The parts below solid sine function and above the line L_0 are painted blue. Three strips S_1, S_2 and S_4 line up above L_0. Their interceptions with the solid sine function are projected to the $(-\mu)$-axis. (b) Inside the blue Π-bar, $(1,0,0)$ triple-loop pieces are drawn to match the strips in the plot (a) that they are derived from. From the middle to the both sides of the blue bar, it lists a green bar, a brown bridge, and a pink $\cap$-bar. The width of the green bar in the middle is much larger than the rest. The width of the pieces is decreasing from the middle green bar to the side boundaries of the blue bar. The pieces on the right of the green bar are slightly wider than the pieces on the left.

cannot merge and they become a pair of Π-bars or $\cap$-bars (Figure 3.8(b)). The $\cap$-bar is closer to the boundaries of the blue Π-bar. Same as the section 2.3, the green bar in the middle and the pair of "Y" shapes can only have one of each if they exist. The other pieces can have more than one of each in their neighborhoods. Also one or more of the triple-loop pieces in Figure 3.8(b) can be missing. The width of the green bar is much larger than the rest. In conclusion, the $(1,0,0)$ triple-loop HBs fall inside the $(1,0)$ double-loop HBs. In a real structure sweeping, probably the green bar is the only $(1,0,0)$ triple-loop structure that we can see. The rest is simply too slim to be seen because the sine function is made of nearly vertical line segments and the green bar is derived from one of the flattest parts of the sine

function. The boundaries of the $(1,0,0)$ triple-loop pieces are the $(1,0,0)$ triple-loop HBs.

If $B_0 < 1$, the dashed sine function is totally outside of the blue regions. Everything is the same as in the case of $B_0 > 1$ except that we don't have yellow "Y" shapes and pink Π-bars in the picture (Figure 3.9). It is obvious that we can not have "Y" shapes. We can not have pink Π-bars because the blue region will vanish at one point and therefore all the interceptions inside must vanish at a certain point too.

3.1.5 $(1,1,1,\cdots)$ or right multi-loop homoclinic bifurcation

When the right unstable separatrix of the origin Γ^+ loops on the right l times and then hits the stable manifold W^s, a $(1,1,1,\cdots,1)_l$ or right l-loop homoclinic orbit is produced ($l > 3$). The Poincaré mapping with the dominant terms only is (equations of φs are omitted)

$$\begin{aligned}
z_1 &= \mu - B_0 R^{1-\nu_0}\mu^{\nu_0}\sin(\Omega_0 \ln \mu + \phi_2) + O(\mu^{2\nu_0}),\\
z_2 &= \mu - B_0 R^{1-\nu_0} z_1^{\nu_0}\sin(\Omega_0 \ln z_1 + \phi_2) + O(z_1^{2\nu_0}),\\
&\cdots\\
z_{l-2} &= \mu - B_0 R^{1-\nu_0} z_{l-3}^{\nu_0}\sin(\Omega_0 \ln z_{l-3} + \phi_2) + O(z_{l-3}^{2\nu_0}),\\
z_{l-1} &= \mu - B_0 R^{1-\nu_0} z_{l-2}^{\nu_0}\sin(\Omega_0 \ln z_{l-2} + \phi_2) + O(z_{l-2}^{2\nu_0}).
\end{aligned} \tag{3.15}$$

The goal is to find the structure of the right l-loop HBs, assuming that we already know all the right multi-loop HBs up to order $l-1$. The equivalent problem is to find $R_l = \{\mu | z_{l-1} < 0\}$, given $R_i = \{\mu | z_{i-1} < 0\}$ $(2 \le i \le l-1)$. Obviously $z_{i-1} > 0$ $(2 \le i \le l-1)$ for $\mu \in R_l$ (System (3.15)). Therefore R_l disjoints $\bigcup_{i=2}^{l-1} R_i$, i.e. $R_l \subset \overline{\bigcup_{i=2}^{l-1} R_i}$. It guarantees the right l-loop HBs fits into the gaps of all the right HBs of lower orders.

Equation System (3.15) can be written as

$$z_1 = \mu - B_0 R^{1-\nu_0}\mu^{\nu_0}\sin(\Omega_0 \ln \mu + \phi_2) + O(\mu^{2\nu_0}), \quad z_{l-1} = f_\mu(z_1).$$

where $f_\mu(\cdot)$ is a smooth function. With a constant $\nu_0 < 1$, the range of z_1 such that $z_{l-1} < 0$ can be solved from $f_\mu(z_1) < 0$. It is a union of countable disjoint positive intervals for a fixed

μ value. These intervals of right l-loop HBs correspond to the strips in Figure 3.6 ($B_0 < 1$) or Figure 3.7 ($B_0 > 1$); they cannot overlap the strips generating lower order right HBs. The shape of the right l-loop HB pieces on the (μ, ν_0)-plane should be determined by the positions of their corresponding strips as we discussed in Section 2.3. We point it out that the intervals are μ related and, therefore, the sides of those strips are not perfectly parallel in general. This fact does not influence the results much but it may break the symmetric arrangement of the right l-loop HBs. For example, in Figure 3.6(b), there may be more yellow bars on the left of the purple $\cap$-bar than on the right.

However, intervals solved from $f_\mu(z_1) < 0$ may merge when $\nu_0 \to 1$, if $l > 3$. As a result, a bridge can exist at a wrong position; for example, a bridge can show up in the yellow bar region in Figure 3.6(b)if $l > 3$. Taking $l = 4$ as an example, this misplacement can be explained by solving System (3.15) for the range of μ such that $z_3 < 0$. We start from solving the last equation to get the range of z_2 such that $z_3 < 0$, which is the union of the purple intervals on the z_2-axis approximately in Figure 3.10(a). The interval I is one of them and marked out in Figure 3.10(a) for further explanation. The range of z_2 is then used in the second last equation $z_2 = \mu - B_0 R^{1-\nu_0} z_1^{\nu_0} \sin(\Omega_0 \ln z_1 + \phi_2) + O(z_1^{2\nu_0})$ to get the range of z_1 such that $z_3 < 0$. It is a union of countable intervals again, among which the intervals J_1 and J_2 of z_1 are derived from the interval I of z_2 on one period of the sine function of z_1 (Figure 3.10(b)). Finally, the range of z_1 is then employed into the first equation $z_1 = \mu - B_0 R^{1-\nu_0} \mu^{\nu_0} \sin(\Omega_0 \ln \mu + \phi_2) + O(\mu^{2\nu_0})$ to obtain the range of μ such that $z_3 < 0$. Of course it is a union of countable intervals of μ. k_{11} and k_{12} are the ones derived from the interval J_1 of z_1 on one period of the sine function of μ. k_{21} and k_{22} are the ones derived from the interval J_2 of z_1 on the same period of the sine function of μ (Figure 3.10(c)). When $\nu_0 \to 1$, the intervals J_1 and J_2 are merging (Figure 3.10(b)). If J_1 and J_2 merge before k_{11} and k_{12} merge, k_{11} and k_{21} will merge and generate a bridge piece of 4-loop HB, so do k_{12} and k_{22} in Figure 3.10(c).

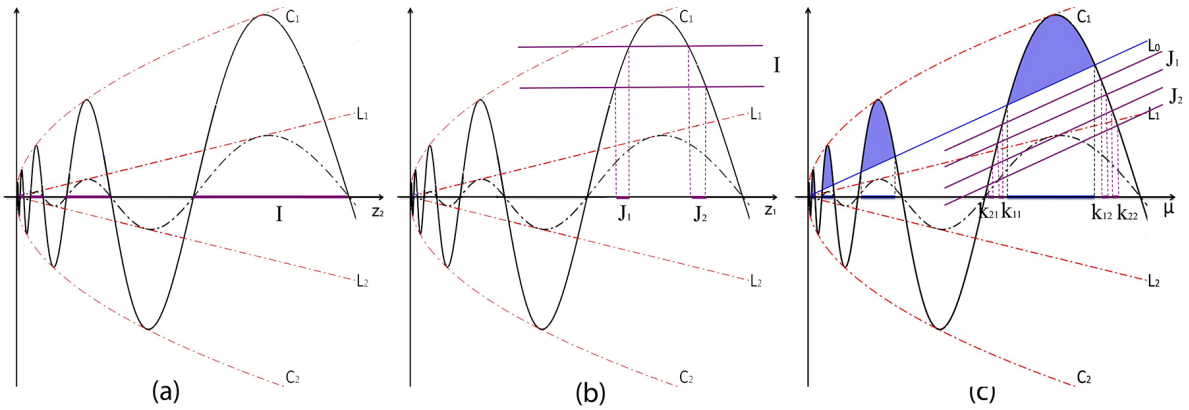

Figure (3.10) (a) The positive parts of the sine function of z_2 are projected onto z_2-axis and painted purple. One of them is notated as I.(b) A purple interval from (a),I, corresponds to a strip that intercepts the sine function of z_1. The purple intervals on the z_1-axis are the projections of the intercepts and they are notated as J_1 and J_2. (c) The intervals from (b) corresponds to two strips and they intercept the sine function of μ. The purple intervals on the μ-axis are the projections of the intercepts and they are notated as k_{11}, k_{12}, k_{21} and k_{22} respectively.

3.1.6 $(1, 0, 0, \cdots)$ or left multi-loop homoclinic bifurcation

When Γ^+ loops on the right once and then on the left $l-1$ times ($\mu < 0$) and then hits the stable manifold W^s, an $(1, 0, 0, \cdots, 0)_l$ or left l-loop homoclinic orbit is produced. The Poincaré mapping with the dominant terms only is (equations of φs are omitted)

$$\begin{aligned}
z_1 &= -\mu - B_0 R^{1-\nu_0}(-\mu)^{\nu_0}\sin(\Omega_0 \ln(-\mu) + \phi_2) + O((-\mu)^{2\nu_0}),\\
z_2 &= -\mu + B_0 R^{1-\nu_0}(-z_1)^{\nu_0}\sin(\Omega_0 \ln(-z_1) + \phi_2) + O((-z_1)^{2\nu_0}),\\
&\cdots\\
z_{l-2} &= -\mu(+/-) B_0 R^{1-\nu_0}(-z_{l-3})^{\nu_0}\sin(\Omega_0 \ln(-z_{l-3}) + \phi_2) + O((-z_{l-3})^{2\nu_0}),\\
z_{l-1} &= -\mu(-/+) B_0 R^{1-\nu_0}(-z_{l-2})^{\nu_0}\sin(\Omega_0 \ln(-z_{l-2}) + \phi_2) + O((-z_{l-2})^{2\nu_0}).
\end{aligned} \tag{3.16}$$

The sign $(+/-)$ is alternating in the above equation system.

To find the structure of the left l-loop HBs is to find the range of μ such that $z_{l-1} < 0$, say D_l. Obviously $L_l \subset L_{l-1}$ because $z_{l-2} < 0$ in System (3.16). Therefore, the set, $\{L_i\}_{i=2}^{\infty}$,

is decreasing for any $0 < \nu_0 < 1$. System (3.16) can be rewritten as

$$z_1 = -\mu - B_0 R^{1-\nu_0}(-\mu)^{\nu_0}\sin(\Omega_0 \ln(-\mu) + \phi_2) + O((-\mu)^{2\nu_0}), \quad z_{l-1} = g_\mu(z_1).$$

where $g_\mu(\cdot)$ is a smooth function. The range of z_1 such that $z_{l-1} < 0$ is a union of countable disjoint negative intervals for a fixed μ. Similar to the section 2.5, the structure of left l-loop HBs can be illustrated by Figures 3.8 and 3.9. The same structure repeats inside the middle green $\cap$-bar, only bridges can be inside a bridge and only bars can be inside a bar other than the middle green bar (a side bar). However, when $l > 3$, bridges can be inside a side bar and a bar can be inside a bridge.

3.1.7 Mixed multi-loop homoclinic bifurcation

The homoclinic orbits that are not left or right homoclinic orbits, are called mixed multi-loop homoclinics. The system will be a mix of equations from Systems (3.15) and (3.16). The small term μ is omitted for simplification. Let

$$f_0(x) = (+/-)B_0 R^{1-\nu_0}(-x)^{\nu_0}\sin(\Omega_0 \ln(-x) + \phi_2),$$
$$f_1(x) = -B_0 R^{1-\nu_0} x^{\nu_0}\sin(\Omega_0 \ln x + \phi_2).$$

The mapping for a $(1, \alpha_1, \alpha_2, \cdots, \alpha_{l-1})$ l-loop homoclinic orbit is

$$z_1 = f_{\alpha_1}(\mu),\ z_2 = f_{\alpha_2}(z_1),\ \cdots,\ z_{l-2} = f_{\alpha_{l-2}}(z_{l-3}),\ z_{l-1} = f_{\alpha_{l-1}}(z_{l-2}), \tag{3.17}$$

where $\alpha_i \in \{0, 1\}$ for $1 \le i \le l$. Rewrite it as

$$z_{l-2} = F(\mu) = f_{\alpha_{l-2}} \circ f_{\alpha_{l-3}} \circ \cdots \circ f_{\alpha_1}(\mu), \quad z_{l-1} = f_{\alpha_{l-1}}(z_{l-2}), \tag{3.18}$$

Similar to the discussion in the section 2.3, $\frac{df_0}{dx}, \frac{df_1}{dx} \approx \infty$ except for the small neighborhoods of their extreme points. Therefore $\frac{dF}{d\mu} = \frac{df_{\alpha_{l-2}}}{dz_{l-3}} \cdot \frac{df_{\alpha_{l-3}}}{dz_{l-4}} \cdots \frac{df_{\alpha_1}}{d\mu} \approx \infty$ except for the small neighborhoods of its extreme points. Thus the function $y = F(\mu)$ is a collection of nearly

vertical line segments and obviously is bounded. It has many extreme points because $\frac{dF}{d\mu} = 0$ at the points where $\frac{df_{\alpha_i}}{dz_{i-1}} = 0$ $(1 \leq i \leq l-2$ and $z_0 = \mu)$. The oscillating function in Figure 3.11 is an example of the function $z_{l-2} = F(\mu)$ if $\mu > 0$ and it is similar if $\mu < 0$. For the sake of structure visibility, the monotone parts are not so steep as they should be in Figure 3.11. The blue projection intervals on the μ-axis collect all the μ values such that $z_{l-2} < 0$, and they are $(1, \alpha_1, \alpha_2, \cdots, \alpha_{l-2})$ $(l-1)$-loop intervals.

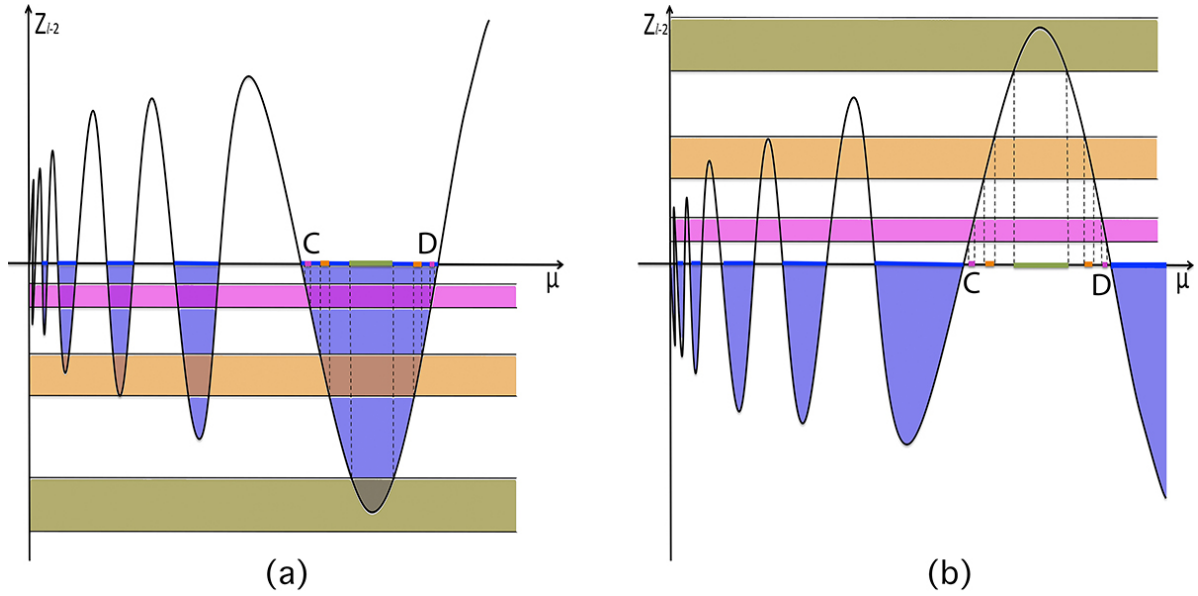

Figure (3.11) The oscillating function is assumed to be $z_{l-2} = F(\mu)$ where $\mu > 0$. The regions of $z_{l-2} < 0$ are marked blue. The projections of them on the μ-axis are marked as blue intervals. Points C and D are the endpoints of one of the intervals.(a) In the case of $\alpha_{l-1} = 0$, the strips of $z_{l-1} = f_{\alpha_{l-1}}(z_{l-2}) < 0$ are beneath the μ-axis. The projected intervals of the interceptions of the strips and the oscillating function are inside the blue intervals. (b) In the case of $\alpha_{l-1} = 1$, the strips of $z_{l-1} = f_{\alpha_{l-1}}(z_{l-2}) < 0$ are above the μ-axis. The projected intervals of the interceptions of the strips and the oscillating function fall in the gaps of the blue intervals.

If $\alpha_{l-1} = 0$, without loss of generality, assume that $f_{\alpha_{l-1}}(z_{l-2}) = -B_0 R^{1-\nu_0}(-z_{l-2})^{\nu_0} \sin \Omega_0 \ln(-z_{l-2}) + \phi_2)$. The solutions of $z_{l-1} = f_{\alpha_{l-1}}(z_{l-2}) < 0$ are $z_{l-2} \in (-e^{-\frac{2m\pi}{\Omega_0} + \frac{\pi}{\Omega_0} - \frac{\phi_2}{\Omega_0}}, -e^{-\frac{2m\pi}{\Omega_0} - \frac{\phi_2}{\Omega_0}}) = I_m$ $(m \in \mathbb{Z}$ and large enough). The interval between I_m and I_{m+1} is notated as $J_m = (-e^{-\frac{2m\pi}{\Omega_0} - \frac{2\pi}{\Omega_0} - \frac{\phi_2}{\Omega_0}}, -e^{-\frac{2m\pi}{\Omega_0} + \frac{\pi}{\Omega_0} - \frac{\phi_2}{\Omega_0}})$ $(m \in \mathbb{Z}$ and large enough).

It is easy to see that $I_{m+1}/I_m = J_{m+1}/J_m = e^{-\frac{2\pi}{\Omega_0}}$. $\{I_m\}$ are strips beneath and accumulated to the μ-axis in Figure 3.11 (three example strips are sketched). The projection intervals on the μ-axis of the interception of the strips and $z_{l-2} = F(\mu)$ are the $(1, \alpha_1, \alpha_2, \cdots, \alpha_{l-1})$ l-loop intervals and they are inside the blue intervals, i.e., the $(1, \alpha_1, \alpha_2, \cdots, \alpha_{l-2})$ $(l-1)$-loop intervals. $(1, \alpha_1, \alpha_2, \cdots, \alpha_{l-2})$ $(l-1)$-loop homoclinic orbits occur at the endpoints of the blue intervals, such as points C and D in Figure 3.11. Inside the example blue region, the green interval is much wider than the rest of the l-loop intervals because it is derived from one of the extreme points of the function $z_{l-2} = F(\mu)$ and the rest intervals are derived from the nearly vertical line segments.

If $\alpha_{l-1} = 1$, the solutions of $z_{l-1} = f_{\alpha_{l-1}}(z_{l-2}) < 0$ are positive intervals and therefore the $(1, \alpha_1, \alpha_2, \cdots, \alpha_{l-1})$ l-loop intervals are in the gaps of the $(1, \alpha_1, \alpha_2, \cdots, \alpha_{l-2})$ $(l-1)$-loop intervals (Figure 3.11(b)). The middle l-loop interval is significantly longer than the rest in Figure 3.11(b) because it is derived from a flat part of the function $z_{l-2} = F(\mu)$.

For a real structure scanning, the middle HB pieces derived from the flat regions of the function $z_{l-2} = F(\mu)$ might be the ones that are visible. All the rest pieces derived from the nearly vertical parts are too slim to be seen.

In the neighborhood of a endpoint of a $(1, \alpha_1, \alpha_2, \cdots, \alpha_{l-2})$ $(l-1)$-loop interval, such as C or D in Figure 3.11, the oscillating function $z_{l-2} = F(\mu)$ is linear approximately. Therefore the $(1, \alpha_1, \alpha_2, \cdots, \alpha_{l-1})$ l-loop intervals that are in those neighborhoods keep a scalability ratio $e^{-\frac{2\pi}{\Omega_0}}$ of width and distance since $I_{m+1}/I_m = J_{m+1}/J_m = e^{-\frac{2\pi}{\Omega_0}}$.

Theorem 3.1.2 *Under the conditions of Theorem 3.1.1, all* $(\alpha_1, \alpha_2, \cdots, \alpha_l)$ *l-loop HBs where* $\alpha_i \in \{0, 1\}$ *($1 \le i \le l$), are located within the* $(\alpha_1, \alpha_2, \cdots, \alpha_{(l-1)})$ $(l-1)$*-loop HBs if* $\alpha_l = 0$ *or fall into the gaps among the* $(\alpha_1, \alpha_2, \cdots, \alpha_{(l-1)})$ $(l-1)$*-loop HBs if* $\alpha_l = 1$*. Their scalability ratio of width and distance is* $e^{-\frac{2\pi}{\Omega_0}}$ *if they are in a small neighborhood of the* $(\alpha_1, \alpha_2, \cdots, \alpha_{(l-1)})$ $(l-1)$*-loop HBs.*

3.2 Homoclinic bifurcation structure sweeping of a Chua's circuit by a computational method

For System (3.1), the NSF curve of O is $b = \frac{(a^2-33a+36)(a-6)}{36(3-a)}$(i.e., saddle index $\nu = 1$). The NDSF curve of O is $a = 6$(i.e., saddle index $\nu = 1/2$). They are plotted in Figure 3.1 and 3.13. The curve such that $\nu = 0$ at the origin O does not exist in System (3.1). However the curve for $\nu = \xi$ at O is $b = (\frac{7a(a-6)}{12} - \frac{\xi(a-6)^3}{36(1-2\xi)^2})/(a\xi - 3)$ for $\xi \neq 1/2$ and $0 < \xi < 1$. It has an asymptote $a = 3/\xi$ and therefore we can take $a = 3/\xi$ as the $\nu = \xi$ curve approximately. The curve of $\mu = 0$ is the $H8$ curve in figure 1. The transformation from the (μ, ν_0) plane to the (a, b) plane is easy to follow, thus System (3.1) is an ideal example to check the theory built in section 2. A bi-parametric structural sweeping of System (3.1) is done by using the computational method introduced earlier in this chapter (see [62]) with small changes.

3.2.1 The introduction of the computational method

The Chua's circuit (3.1) has three equilibrium states: $O(0, 0, 0)$, $O_1(-1, 0, 1)$ and $O_2(1, 0, -1)$. We follow the trajectory that initiates from the right unstable separatrix of the origin and record "1" if it makes a loop around the right equilibrium $O_2(1, 0, -1)$ and "0" if it makes a loop around the left equilibrium $O_1(-1, 0, 1)$. Computationally, we record "1" if x reaches a positive maximum that is greater than "1" and record "0" if x reaches a negative minimum that is less than "-1" (see Figure 3.12). A binary sequence (named as a kneading sequence) is recorded for a pair of fixed parameter values of a and b. We point it out that the first symbol is skipped in this study since it is always "1". The binary sequence is then converted to a decimal number by $K(a, b) = \sum_{n=1}^{\infty} \kappa_n \, q^n$, where $\{\kappa_n\}_{n=1}^{\infty}$ is the corresponding kneading sequence, and q is a constant to be selected. $0 < q < 1$ is required to guarantee convergence. In this study, $q = 0.5$ is chosen and, therefore, $K(a, b) \in [0, 1]$. The decimal number is named a kneading invariant. A colormap with 100 different colors is then developed to assign colors to kneading invariants. Therefore we are able to produce a colorful system sweep on a bi-parametric plane by calculating the kneading invariants of

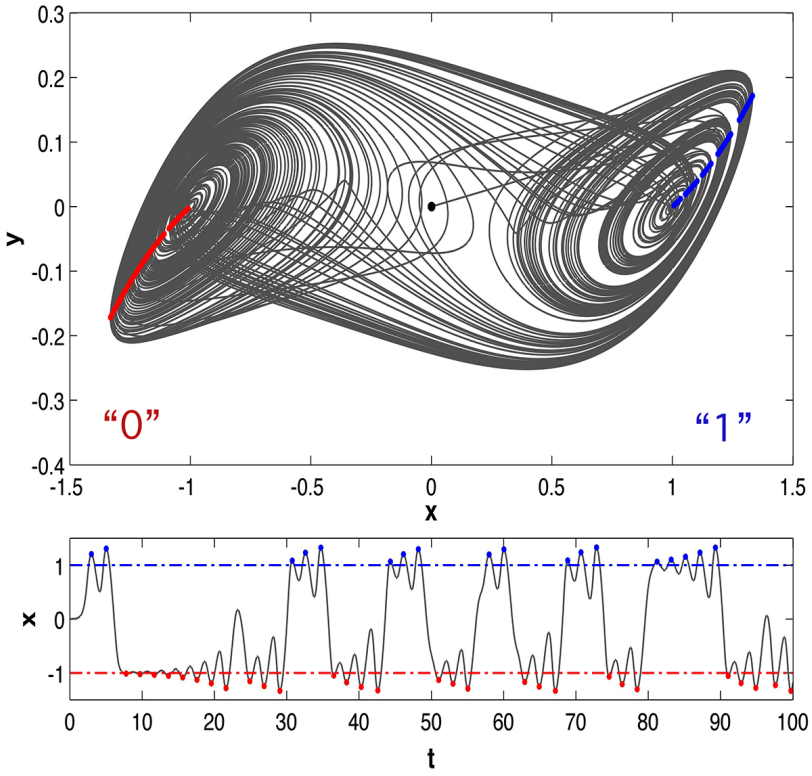

Figure (3.12) This is a trajectory plot for a=10.16 and b=14.7, when the trajectory starts from the right separatrix of the origin. The black dot in the top picture is the origin. When the x-value reaches a minimum that is smaller than -1, we record it as '0' and mark a blue dot in the picture. When the x-value reaches a maximum that is larger than 1, we record it as '1' and mark a red dot in the picture. We have two views of this. The top one is the 3D picture of the trajectory. The bottom one is the trajectory plot of x vs time t.

1000×1000 points on the (a, b) plane. A separate line between two color blocks that are next to each other is a homoclinic bifurcation curve. Using Denis Demidov's code made for GPU device, a structure plot can be generated in about 15 minutes. Practically, we choose a truncated subsequence to calculate a kneading invariant and its feasible length is 10 because $0.5^{10} \approx 0.001 \ll 0.01$ and the colormap can only detect the tenth and hundredth decimal position of a kneading invariant that is known between 0 and 1. The detail can be found earlier in this chapter ([62]).

Figure 3.13(a) is such a structural sweeping with an added neutral saddle-focus bi-

furcation(NSF) curve, i.e., the curve with saddle index $\nu = 1$, and saddle-to-saddle-focus bifurcation(S-SF) curve, and NDS/NDSF curve, i.e. the curve with saddle index $\nu = 1/2$. The interesting region is the wedge that accumulates plenty of HBs and suggests a chaotic behavior. The wedge is located on the right of the NSF curve and above the S-SF curve and therefore the origin is a saddle focus with the saddle index less than 1, satisfying Shilnikov's condition.

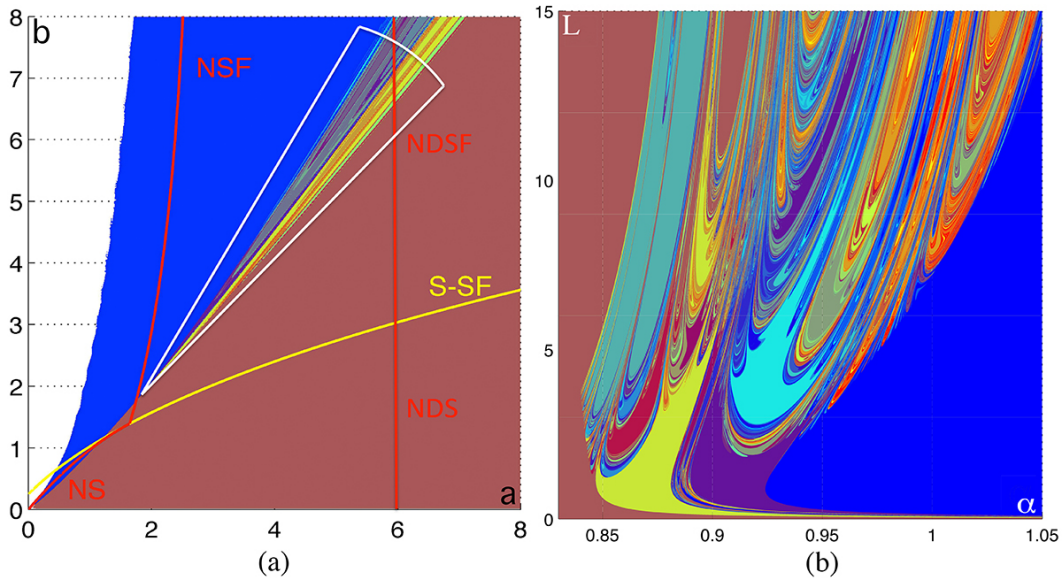

Figure (3.13) (a) The picture is the structure plotting of the Chua's Circuit that we are discussing in this paper. A 2-12 element symbolic subsequence is used. The NSF and NS curve corresponds to saddle index $\sigma = 0$ or $\nu = 1$. $\nu > 1$ left of the curve and $\nu < 1$ right of the curve. The NDSF and NDS curve corresponds to saddle index $\nu = 1/2$. The yellow curve in the picture is the boundary curve of saddle to saddle focus of the origin. The three curves intersect at the point $(1.6458, 1.3934)$. The solid color regions have trivial dynamics or trivial kneading values. The little colorful wedge is the double scroll chaotic region caused by homoclinic bifurcations. The sector bounded by the white curves is the region in which we employed the transformation. The center of the sector is at $(1.8623, 1.8743)$. (b) Structure sweeping of the sector in (a) after the transformation. α is the angle of a radius inside the sector. It ranges from 0.8 to 1.05. L is the length of a radius inside the sector and it ranges from 0 to 15. Every line in the picture that separates two different colors is a homoclinic bifurcation curve on the (α, L) bi-parametric plane. A 6-15 element kneading subsequence are used.

To have a better look inside the wedge, we can use a transformation to fan it out. A

sector is taken, as in Figure 3.13(a), and it is bounded by white curves. The center of the sector is $(1.8623, 1.8743)$. Two new parameters, α and L, are used for the transformation. Here α is the radian measure of the angle between a radius inside the sector and the positive x-axis and L is the length of the radius. The transformation is expressed as below

$$a = L \cdot cos(\alpha) + 1.8623, b = L \cdot sin(\alpha) + 1.8743, \tag{3.19}$$

where $\alpha \in (0.8, 1.05)$ and $L \in (0, 15)$. The structural plot of the sector after transformation is shown in Figure 3.13(b). Hundreds of HBs appear but it is hard to see how they are arranged. That is the task we are resolving now.

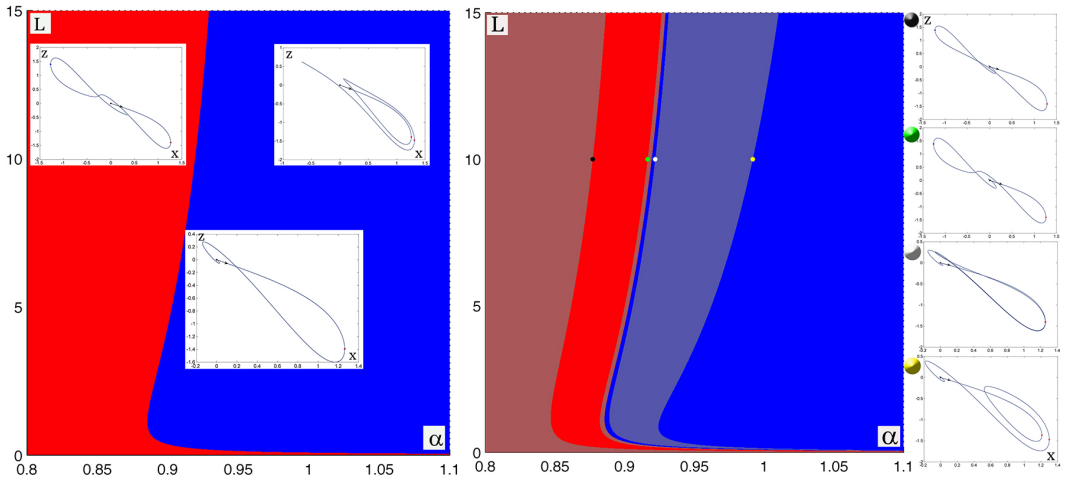

Figure (3.14) The left picture is a 2-2 subsequence kneading invariant plotting. The trajectories in the red region have symbolic sequences starting from $\{1, 0, \ldots\}$ and those in the blue region have symbolic sequences starting from $\{1, 1, \ldots\}$. The separating line is the primary homoclinic bifurcation curve. All parameter points on the curve have corresponding symbolic sequence $\{1\}$. The 2-3 subsequence kneading invariant plot gives another two new homoclinic bifurcation curves. The one that the black and yellow points are on corresponds to the symbolic sequence $\{1, 0\}$. The one that the white and yellow points are on corresponds to the symbolic sequence $\{1, 1\}$. The position of the black point in $\alpha - l$ plane is $(0.876898493756, 9.995)$. The position of the green point is $(0.91631772114, 9.995)$. The position of the white point is $(0.921727874, 9.995)$. The position of the yellow point is $(0.991649733, 9.995)$

In Figure 3.14, kneading invariants calculated by 2-2 element subsequences (where for

each parameter point, only the second element is taken) reveal the primary HB, H_1. Kneading invariants calculated from the 2-3 (element) subsequences disclose double-loop HBs. The double-loop HBs lie on the both sides of H_1 ($\mu = 0$) symmetrically as shown in figure 3.14. The left side of H_1 corresponds to $\mu < 0$ and the right side corresponds to $\mu > 0$. Only one double-loop HB piece on each side of H_1 can be seen in the picture. They correspond to the largest blue bars in Figure 3.3(b) or 3.4(b). The rest of the infinitely many double-loop HB pieces are too narrow to be seen due to the reason discussed in section 3. The plot done by kneading invariants calculated from 2-4 kneading subsequences exposes triple-loop HBs, and so on. The longer the kneading sequence used, the higher the order of HBs that are found in the structure plot. Six-15 kneading subsequences are used to plot Figure 3.13(b). Theoretically, 2-15 kneading subsequence should be used for revealing all the HBs up to 14-loops. But computationally only the first 10 elements in a sequence are consequential. Therefore the 6-15 subsequences are chosen and in practice the $(1-5)$-loop HBs are still in the picture done by the 6-15 kneading subsequences.

3.2.2 $(1, 1, 1, \ldots)$ or right multi-loop homoclinic bifurcation curves

Figure 3.13(b) shows all HBs up to certain order. To show only right homoclinic bifurcation curves, we need to change the method of the calculation for kneading invariants. For a kneading sequence, we calculate the number of 1s before a 0 shows up. Assuming the number is n, the corresponding kneading invariant is defined as $K(\alpha, L) = n/20$ (In this study, the total length of a kneading sequence is 20). To show the primary HB, we round $K(\alpha, L)$ to 1 if it is greater than 0.5×1 and then plot using the colormap (Figure 3.15(a)). To add right double-loop HBs to the plot (a), we round $K(\alpha, L)$ to 1 if it is greater that 0.5×2 (Figure 3.15(b)). To add right triple-loop HBs to the plot(b), we round $K(\alpha, L)$ to 1 if it is greater that 0.5×3, and so on.

The primary HB, H_1 shows in Figure 3.15(a). The only visible right double-loop HB in Figure 3.15(b) corresponds to the largest and the furthest blue bar to the right in Figure 3.3 or 3.4. The two pink pieces emerging in Figure 3.15(c) are right triple-loop bars generated

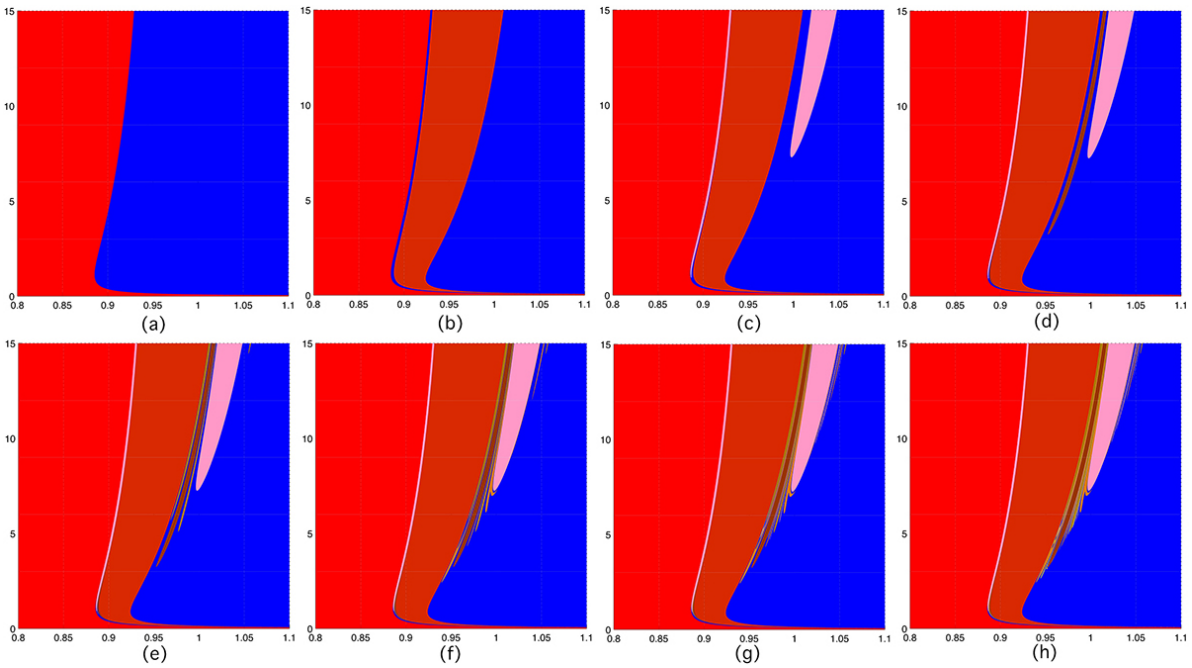

Figure (3.15) (a) A plot that only has the primary HB. (b) A plot that has right homoclinic bifurcation curves up to order 2, i.e. primary and $(1,1)$ double-loop HBs. (c) A plot that has right HBs up to order 3, i.e. primary, $(1,1)$ double-loop and $(1,1,1)$ triple-loop HBs. (d) A plot that has right HBs up to order 4. (e) A plot that has right HBs up to order 5. (f) A plot that has right HBs up to order 6. (g) A plot that has right HBs up to order 7. (h) A plot that has right HBs up to order 8.

from the strip S_1 and they correspond to the large purple bar in the center of Figure 3.6(b) or 3.7(b). And of course the boundaries of the pink pieces are right triple-loop HBs. All the rest of the right triple-loop HB pieces discussed in the section 2.3 are too slim to be seen. The right 4-loop HBs fall in the gaps between the right triple-loop HBs, and the right 5-loop HBs fall in the gaps between the the right 4-loop HBs, and so on. The higher order HBs are harder to see because they are narrower. The dark red new piece in the plot (d) is obviously generated from the strip S_4 in Figure 3.6 because it is a $\cap$-bar and it is between the blue and the purple bars. Two more visible yellow pieces show up in the plot (e). Their boundaries are right 5-loop HBs and their position tells us that they are generated from the strip S_4, too. There is a "Y" shaped piece emerging in the plot (f) near the triple-loop pink piece that is generated from the strip S_1 in Figure 3.6. An enlarged picture of the plot (f)

can be found in Figure 3.16. According to its position, it must be derived from the strip S_3 in Figure 3.6. Of course, its boundary is a right 6-loop HB. In the enlarged figure 3.16(b), a bridge can be found on the top of a yellow piece that was determined earlier to be derived from the strip S_4 in Figure 3.6. It violates Figure 3.6, but it was discussed in section 2 that violations can happen after triple-loops.

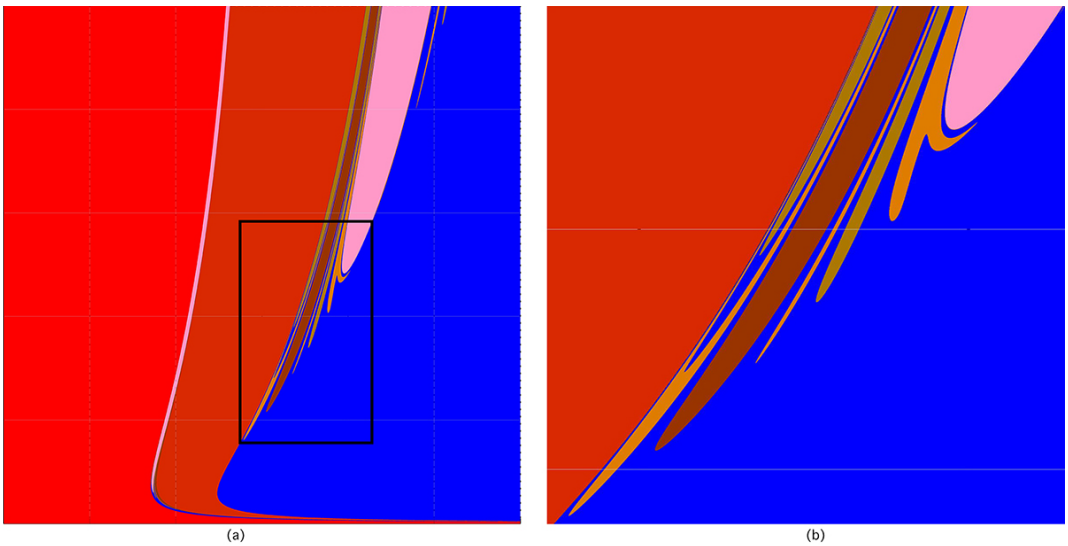

Figure (3.16) (a) It is the plot (f) in Figure 3.11, i.e. A plot that has right HBs up to order 6. (b) It is an enlarged plot of the rectangular area in (c).

3.2.3 $(1, 0, 0, \ldots)$ or left multi-loop homoclinic bifurcation curves

To have left HBs only, a similar method to the section 3.2 is used for calculating the kneading invariants. Skip the first symbol and count the number of 0s before the first 1, assuming the number is n. Then the kneading invariant is defined as $K(\alpha, L) = n/20$. To show the primary HB only, $K(\alpha, L)$ is rounded to 1 if it is greater than 0.5×0. To add right double-loop HBs to the structure plot, $K(\alpha, L)$ is rounded to 1 if it is greater that 0.5×1. To add right triple-loop HBs to the plot, $K(\alpha, L)$ is rounded to 1 if it is greater that 0.5×2, and so on. Figure 3.17 lists 6 plots with left multi-loop HBs only. The plot (a) has primary and $(1, 0)$ double-loop HBs; the plot (b) has primary, $(1, 0)$ double-loop and $(1, 0, 0)$

triple-loop HBs, and so on. Only one of the infinitely many left double-loop pieces is visible in the plot (a) and the rest of them are too slim to be seen as discussed in the section 2. Similarly, only one of the infinitely many left triple-loop pieces is visible in Figure 3.17(b) and it must correspond to the middle green bar in Figure 3.8(b) or 3.9(b) that is derived from the strip S_1 and the story repeats.

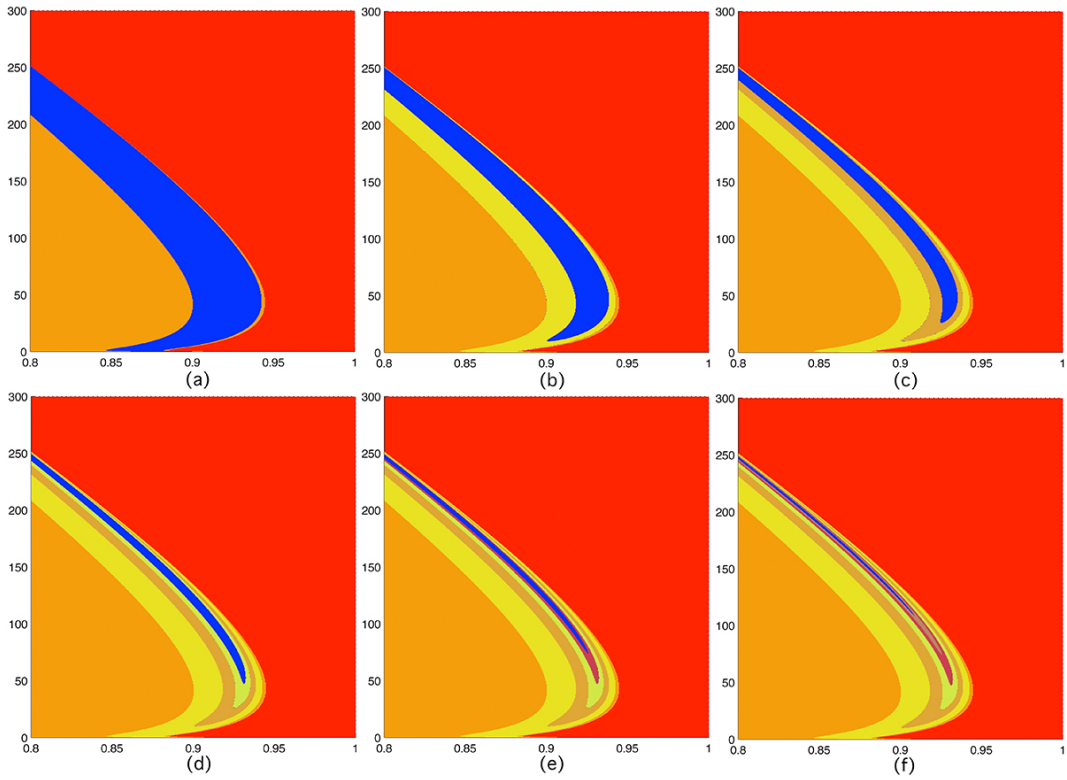

Figure (3.17) (a) A plot that has left HBs up to order 2, i.e. primary and $(1,0)$ double-loop HBs. (b) A plot that has left HBs up to order 3, i.e. primary, $(1,0)$ double-loop and $(1,0,0)$ triple-loop HBs. (c) A plot that has left HBs up to order 4. (d) A plot that has left HBs up to order 5. (e) A plot that has left HBs up to order 6. (f) A plot that has left HBs up to order 7.

3.2.4 Mixed multi-loop homoclinic bifurcation curves

Figure 3.18 lists 6 system-structure-sweepings of the Chua's circuit with one more loop HBs added in each successive picture. The plot (a) has primary and double HBs; the plot

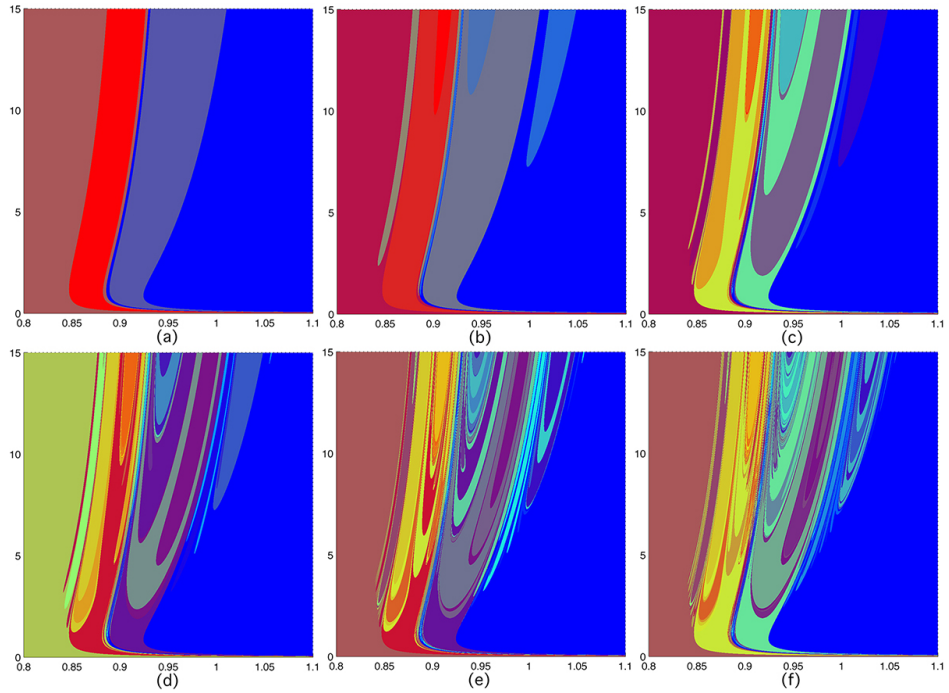

Figure (3.18) The kneading invariants are calculated by the expression $K(a,b) = \sum_{n=1}^{\infty} \kappa_n \, 0.5^n$. (a)This plot has HBs up to order 2, i.e. primary and double-loop HBs. The kneading invariants are calculated from the 2-3 subsequences of the kneading sequences. (b)This plot has HBs up to order 3, i.e. primary, double-loop and triple-loop HBs. The kneading invariants are calculated from the 2-4 subsequences of the kneading sequences. (c)This plot has HBs up to order 4. The kneading invariants are calculated from the 2-5 subsequences of the kneading sequences. (d)This plot has left HBs up to order 5. The kneading invariants are calculated from the 2-6 subsequences of the kneading sequences. (e)This plot has left HBs up to order 6. The kneading invariants are calculated from the 2-7 subsequences of the kneading sequences. (f)This plot has left HBs up to order 7. The kneading invariants are calculated from the 2-8 subsequences of the kneading sequences.

(b) has primary, double and triple HBs, and so on. At the end, the plot (f) has all HBs with up to 7 loops. The double HBs locate on the both sides of the primary HB symmetrically and are already discussed in the section 3.1. l-loop HBs fit into the plot with HBs up to order $l-1$ either by squeezing into the gaps or falling inside the lower order HB pieces. Very likely only the HB pieces that derive from the strips that intercept the flat extreme point regions, such as the green strip in Figure 3.11, are visible in the plots. There are infinitely many HBs that are too slim to be seen according to the analysis stressed in the section 2.

It is too complicated and unnecessary to do a complete unfolding discussion on the mixed multi-loop HBs plots (Figure 3.18). But some interesting details can be pointed out. For example, from plot (b) to plot (c), two visible bridges are added in the right double-loop HB piece and they must be derived from the strip S_2 in Figure 3.8 or 3.9. There are also two symmetric *cap*-bars added to the picture in the left double-loop HB piece, and they must be derived from the strip S_4 in Figure 3.8 or 3.9. Similar details can be found in the plots. We will not go over them one by one here.

PART 4

INTRINSIC MECHANISMS STUDY IN THREE ESCAPE CELLS NETWORKS

4.1 Fitzhugh-Nagumo model

$$\begin{aligned} x' &= m(x - x^3) - y + I, \\ y' &= \epsilon\left(\frac{1}{1+e^{-k(x-x_0)}} - y\right) \end{aligned} \tag{4.1}$$

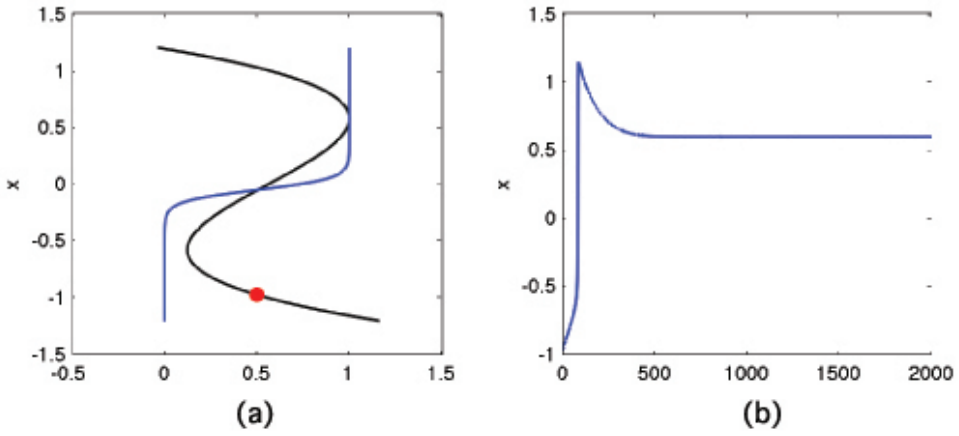

Figure (4.1) Escape case for one cell. In this picture, $I = 0.562$, $\epsilon = 0.02$, $k = 20$, $m = 1.14$, $x_0 = -0.05$, and the initial point is at $(-0.97, 0.5)$. The slow nullcline just touches the top knee point of the fast nullcline. With a stable equilibrium state on the top stage of the fast nullcline, the cell converges to the equilibrium state on the depolarization branch.

The equation set (4.1) models a cell by a slow-fast system. It has a cubic fast nullcline branch, $y = m(x-x^3)+I$, shown as the black cubic curve in Figure 4.1(a) and the Boltzmann function as its slow nullcline branch, $y = \frac{1}{1+e^{-k(x-x_0)}}$, shown as the blue curve in Figure 4.1(a). The two extreme points on the black curve are called knee points in this paper. Escape refers to the case where the slow nullcline intersects the upper branch, representing active voltage,

of the fast nullcline and produces a stable equilibrium state. From its location, this fixed point models a tonic spiking state. The stable fixed point must be close to the top knee point so that a small inhibition kick can remove it and open a gap at the top knee point, allowing the cell to move to the lower branch. This is referred to as the cell escaping from the spiking state. The parameter I, m, k and x_0 can be adjusted to generate escape cases. The specific values of those parameters are less strict for the phase dynamics of three escape cells that we will elaborate on later. For convenience and consistency, we fix them as $I = 0.562$, $m = 1.14$, $k = 20$ and $x_0 = -0.05$ for the escape case.

4.2 3-cell escape network

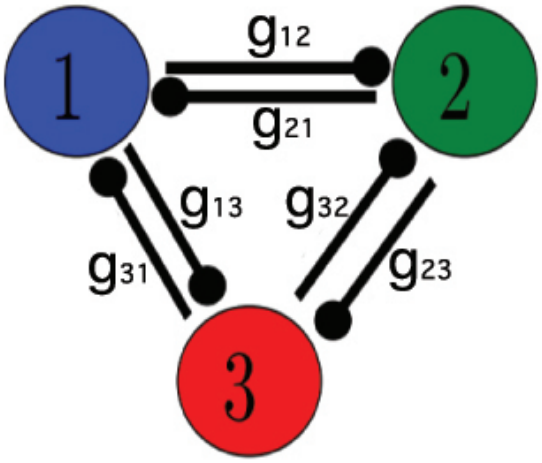

Figure (4.2) Three cell network with reciprocally inhibitory connections. The coupling strengths are labeled in the diagram.

With a small perturbation of the fast nullcline to the left, the system shown in Figure 4.1 produces a little gap which allow the cell to switch branches. Actually, a perturbation larger than 0.0008 will generate such a gap. To avoid blocking the bottom gap and shutting off the cell by creating a hyperpolarization stable equilibrium state, the perturbation should

be less than 0.124.

$$\begin{aligned}
x_1' &= m(x_1 - x_1^3) - y_1 + I - g_{21} \cdot \tfrac{x_1 - E}{1+e^{-k_1 x_2}} - g_{31} \cdot \tfrac{x_1 - E}{1+e^{-k_1 x_3}}, \\
y_1' &= \epsilon \left(\tfrac{1}{1+e^{-k_2(x_1 - x_0)}} - y_1 \right), \\
x_2' &= m(x_2 - x_2^3) - y_2 + I - g_{12} \cdot \tfrac{x_2 - E}{1+e^{-k_1 x_1}} - g_{32} \cdot \tfrac{x_2 - E}{1+e^{-k_1 x_3}}, \\
y_2' &= \epsilon \left(\tfrac{1}{1+e^{-k_2(x_2 - x_0)}} - y_2 \right), \\
x_3' &= m(x_3 - x_3^3) - y_3 + I - g_{13} \cdot \tfrac{x_3 - E}{1+e^{-k_1 x_1}} - g_{23} \cdot \tfrac{x_3 - E}{1+e^{-k_1 x_2}}, \\
y_3' &= \epsilon \left(\tfrac{1}{1+e^{-k_2(x_3 - x_0)}} - y_3 \right),
\end{aligned} \tag{4.2}$$

where $I = 0.562$, $k_1 = k_2 = 20$, $x_0 = -0.05$, $m = 1.14$ and $E = -1.2$. Parameter ϵ and g can be varied for the case study. Two cells that each produces a perturbation of 0.0004 can open a gap for a third cell, thus we use a range of $[0.0004, 0.124]$ as coupling strength, gs . To sustain the mechanism of the slow-fast system, ϵ should be relatively small. In this paper, the range of ϵ is set as $(0, 0.35]$ for the escape case.

4.3 Symmetric 3-cell network

First we consider the symmetric case, i.e, $g_{21} = g_{31} = g_{12} = g_{32} = g_{13} = g_{23}$. TW states and PM states can be stably generated by the symmetric escape system of three cells. However, PM only exist in a small range of parameter values. With $\epsilon = 0.25$, Figure 4.3 illustrates a progression of the phase torus diagram with all g values varied. As can be seen, there are 5 states in total, two TWs and three PMs. At $g = 0.0004$, there are only two TW states. At $g = 0.0006$, three PMs are created from the three saddles thus there are 5 states. We can see from Figure 4.3(b) that the two TWs undergo an Andronov-Hopf bifurcation and generate two stable periodic orbits. When experiencing a TW, the phase differences of the three cells will shift periodically instead of keeping a steady ratio.

When the g value increases from 0.0006 to 0.0011 in Figure 4.3(a-c), the periodic orbits of TWs are getting bigger while the PM basins grow also. Eventually in Figure 4.3(d), at $g = 0.003$, the periodic orbits of TWs merge with the three saddles around them and vanish as 5 states are reduced to 3 states. In Figure 4.3(e), the periodic orbits of TWs

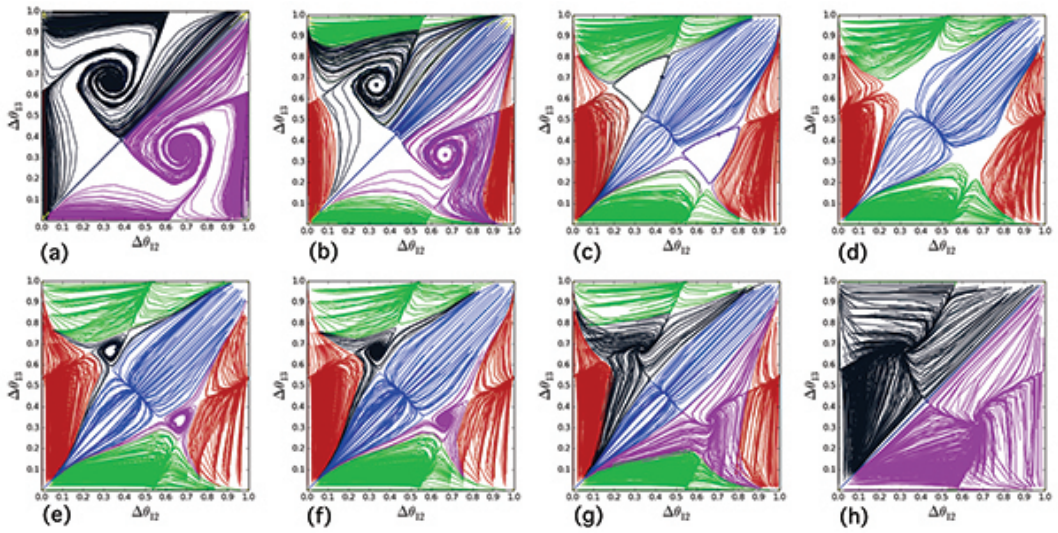

Figure (4.3) $I = 0.562$, $\epsilon = 0.25$, $k = 20$, $m = 1.14$, $x_0 = -0.05$ (a) $g_{21} = g_{31} = g_{12} = g_{32} = g_{13} = g_{23} = 0.0004$. There are two TW states. (b) $g_{21} = g_{31} = g_{12} = g_{32} = g_{13} = g_{23} = 0.0006$. There are two TWs and three PMs. And the two TWs are experiencing Andronov-Hopf bifurcations. (c) $g_{21} = g_{31} = g_{12} = g_{32} = g_{13} = g_{23} = 0.0011$. Two periodic orbits of TWs get bigger and are near to merge with the three saddle points around them. (d) $g_{21} = g_{31} = g_{12} = g_{32} = g_{13} = g_{23} = 0.003$. The TW periodic orbits merger with the saddles and vanish. There are three PM states. (e) $g_{21} = g_{31} = g_{12} = g_{32} = g_{13} = g_{23} = 0.009$. There are 5 states, the TW periodic orbits depart from the saddles. (f) $g_{21} = g_{31} = g_{12} = g_{32} = g_{13} = g_{23} = 0.01$. The TW periodic orbits shrink to TW equilibrium states and an Andronov-Hopf bifurcation occurs. (g) $g_{21} = g_{31} = g_{12} = g_{32} = g_{13} = g_{23} = 0.015$. The TW basins enlarge. (h) $g_{21} = g_{31} = g_{12} = g_{32} = g_{13} = g_{23} = 0.025$. The three PM merge with the saddles and vanish. There are only two TW states left.

are separated from the saddles and emerge. Again there are 5 states again at $g = 0.009$. Another Andronov-Hopf bifurcation occurs and the periodic orbits shrink to stable equilibria of TW in Figure 4.3(f) when $g = 0.01$. With increasing gs, the TWs increase their basins and eventually run the three PMs out of the picture at $g = 0.025$ in Figure 4.3(h). From $g = 0.025$ up to $g = 0.124$, there are only 2 states on the phase torus as in Figure 4.3(h). The 5 states case only exist for a range of g from 0.0006 to 0.025.

It was observed that with a different value of ϵ, the progressive diagrams as g increases can be found in Figure 4.3. For example, when $\epsilon = 0.07$, from $g = 0.0004$ to $g = 0.124$, we see only the last two pictures in Figure 4.3, i.e., pictures (g) and (h). The phase diagrams

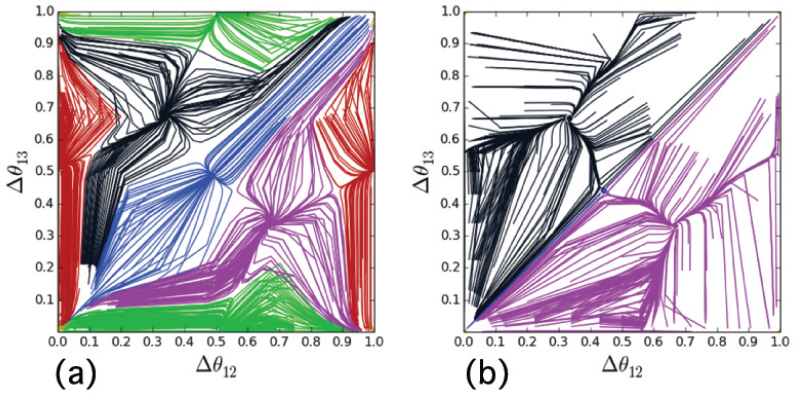

Figure (4.4) $I = 0.562$, $\epsilon = 0.07$, $k = 20$, $m = 1.14$, $x_0 = -0.05$. (a) $g_{21} = g_{31} = g_{12} = g_{32} = g_{13} = g_{23} = 0.0008$. There are two TW states and three PMs. (b) $g_{21} = g_{31} = g_{12} = g_{32} = g_{13} = g_{23} = 0.04$. There are only three PM states.

are plotted in Figure 4.4. Plot (a) has all 5 states at $g = 0.0008$ and plot (b) has two TW states at $g = 0.04$. After $g > 0.04$, the phase picture will keep producing only two TWs.

4.4 Asymmetric 3-cell network

Now we will discuss the asymmetry cases and the phase diagram changes accordingly. When we change the g_{31} connection alone, it breaks the symmetry of the system and the blue and red cells cannot stay together (refer to Figure 4.2). Therefore, we lose the green

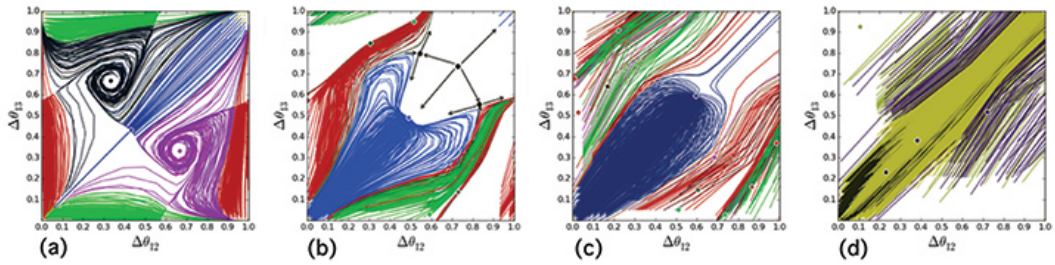

Figure (4.5) $\epsilon = 0.25$. Increase the value of g_{31}. (a) $g_{21} = g_{31} = g_{12} = g_{32} = g_{13} = g_{23} = 0.0006$. There are 5 states. (b) $g_{21} = g_{12} = g_{32} = g_{13} = g_{23} = 0.0006$ and $g_{31} = 0.0008$. Only blue PM is left. (c) $g_{21} = g_{12} = g_{32} = g_{13} = g_{23} = 0.0006$ and $g_{31} = 0.001$. (d) $g_{21} = g_{12} = g_{32} = g_{13} = g_{23} = 0.0006$ and $g_{31} = 0.0015$.

PM. The blue and green cells cannot stay together because the red cell inhibits the blue and green cells with different strengths, and so it will push the blue cell and the green cell apart. The blue PM is the only one that survives this asymmetry. We use $\epsilon = 0.25$ and $g = 0.0006$ as example values in Figure 4.5.

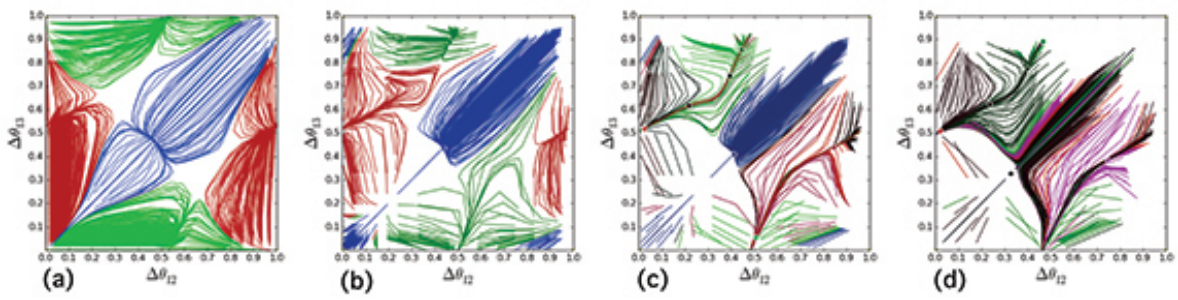

Figure (4.6) $\epsilon = 0.25$. Decrease the value of g_{31}. (a) $g_{21} = g_{31} = g_{12} = g_{32} = g_{13} = g_{23} = 0.003$. There are 3 PM states. (b) $g_{21} = g_{12} = g_{32} = g_{13} = g_{23} = 0.003$ and $g_{31} = 0.002$. Only blue PM is left. (c) $g_{21} = g_{12} = g_{32} = g_{13} = g_{23} = 0.003$ and $g_{31} = 0.0015$. (d) $g_{21} = g_{12} = g_{32} = g_{13} = g_{23} = 0.003$ and $g_{31} = 0.001$.

Figure 4.5(a) is a phase plot of the symmetric model with $\epsilon = 0.25$ and $g = 0.0006$. It has all 5 states. When we slightly increase g_{31} from 0.0006 to 0.0008 and keep the rest coupling strength as 0.0006, the blue PM becomes the "king of the mountain" and the red and the green PMs disappear. In each the white space, there are three equilibria, two saddle and one unstable fixed points, as sketched in Figure 4.5(b). In Figure 4.5(c), the three equilibria that we sketch in (b) merge and become one saddle. Eventually this new saddle merge with the blue PM and a stable periodic orbit (the diagonal line) is created as shown in Figure 4.5(d). The resulting rhythm is the green and red cells staying together and the blue cell change its phase difference periodically.

If we decrease g_{31}, the merge will go the other way. Let's use $\epsilon = 0.25$ and $g = 0.003$ as an example as in Figure 4.6. The symmetric model has three PM states in the phase picture (Figure 4.6(a)). When we change g_{31} from 0.003 to 0.002, the red and green PMs are still in the phase picture as shown in Figure 4.6(b). In Figure 4.6(c), the red and green cells merge with two saddles and generate a stable periodic orbit. Therefore, the red and green PMs are

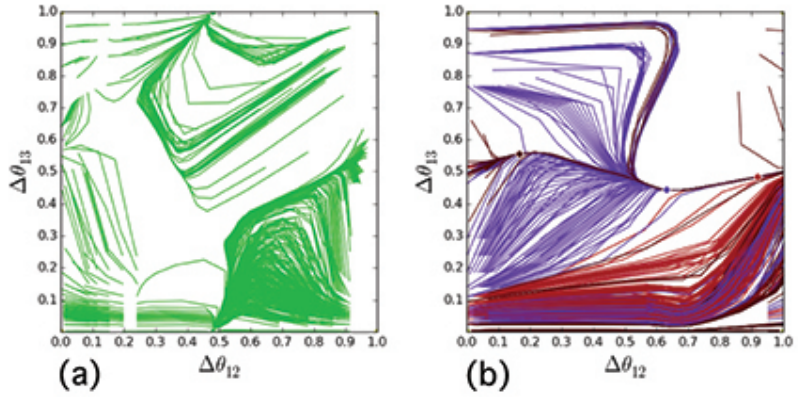

Figure (4.7) $\epsilon = 0.25$ (a) $g_{21} = g_{12} = g_{32} = g_{23} = 0.003$ and $g_{31} = g_{13} = 0.0015$. Only the green PM is left. (b) $g_{21} = g_{12} = g_{32} = g_{23} = 0.003$ and $g_{31} = g_{13} = 0.006$. A stable horizontal periodic orbit is created.

vanished. In plot (d), g_{31} is decreased to 0.001. The blue PM merges with the two saddles on its shoulder and vanishes. All the trajectories converge to the stable periodic orbit created by the red and green cells in plot (c).

Next we change g_{13} and g_{31} equally. If we weaken them equally, the green PM will dominate the whole region eventually (Figure 4.7(a)). If we increase them equally, a horizontal stable periodic orbit with $\Delta\theta_{13}$ around 0.5 is generated as shown in Figure 4.7(b). That means that the blue cell and the red cell will fire in anti-phase while the green cell shifts its relative position periodically.

Now we keep $g_{12} = g_{23} = g_{31}$ and $g_{13} = g_{32} = g_{21}$. If $g_{12} = g_{23} = g_{31}$ is relatively stronger, eventually the 1321 or green-red-blue TW will dominate the phase torus as in Figure 4.8, or vice versa.

Next we change g_{31} and g_{32} equally and keep the other connections the same. When decreasing $g_{31} = g_{32}$, the phase plot will have a stable periodic orbit eventually as in Figure 4.9(a). When increasing $g_{31} = g_{32}$, the phase plot will have a stable periodic orbit eventually as in Figure 4.9(b) if the rest of gs are relatively small, or the phase plot will only have the red equilibrium state and the red cell becomes the "king of the mountain" as in Figure 4.9(c) if the rest of gs are relatively large.

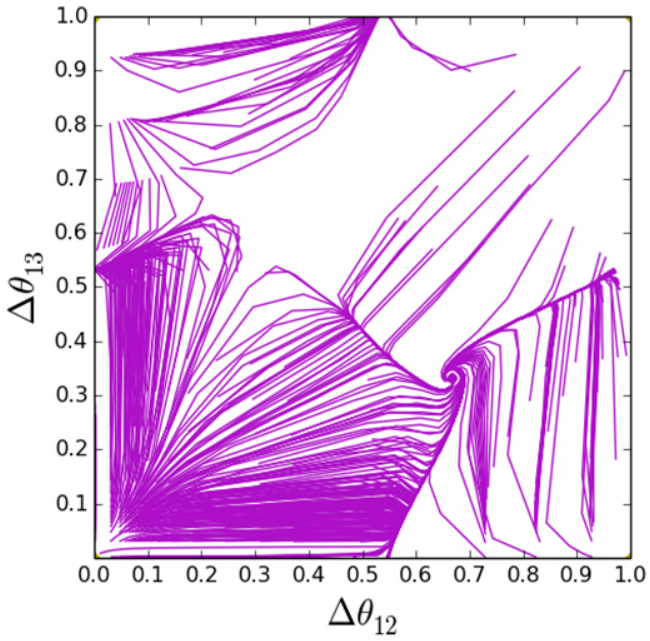

Figure (4.8) $\epsilon = 0.25$. $g_{12} = g_{23} = g_{31} = 0.013$ and $g_{13} = g_{32} = g_{21} = 0.01$. Only the 1321 or green-red-blue TW is left.

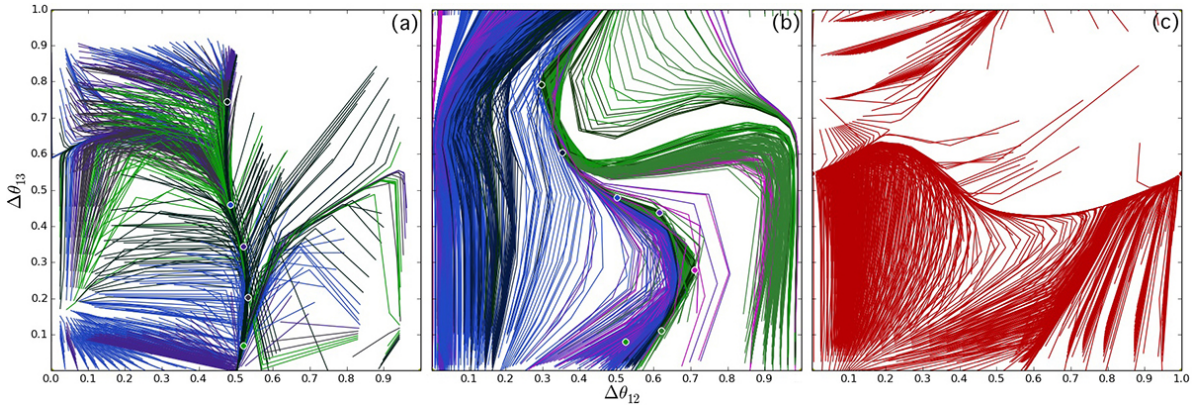

Figure (4.9) $\epsilon = 0.25$. (a) $g_{31} = g_{32} = 0.008$ and $g_{21} = g_{12} = g_{13} = g_{23} = 0.025$. There is a stable periodic orbit, a saddle and a unstable equilibrium point in the picture. (b) $g_{31} = g_{32} = 0.0008$ and $g_{21} = g_{12} = g_{13} = g_{23} = 0.0006$. There is a stable periodic orbit. (c) $g_{31} = g_{32} = 0.025$ and $g_{21} = g_{12} = g_{13} = g_{23} = 0.015$. There is only a red stable equilibrium state.

PART 5

CONCLUSIONS

This dissertation presents two case studies on organizations of homoclinic bifurcations in the parameter space segment. One is in a $\mathbb{Z}_2$ symmetric Lorenz like system, the Shimizu-Morioka model, with a saddle at the center. The other is in a reflexion symmetric system with a Shilnikov saddle-focus at the origin.

The Shimizu-Morioka model is discussed in part 2. It sheds light on the pivotal role of homoclinic and heteroclinic bifurcations as emergent centers for pattern formations in parameter spaces corresponding to complex dynamics. It also reveals universal principles of chaotic dynamics in deterministic systems with Lorenz-like attractors, which include the Lorenz equation itself and similar models [30; 63; 44; 45]. All these systems feature various codimension-two heteroclinic and homoclinic bifurcations such as Bykov T-points, resonant saddles and inclination-switching. We have demonstrated mechanisms generating Shilnikov flames, which underlie the bifurcation transitions from the Lorenz attractor to wildly chaotic quasi-attractors, and outline multi-fractal organizations of the corresponding regions in the parameter space. Our numerical experiments with kneading-based scans of several Lorenz-like systems have unambiguously revealed a wealth of multi-scale swirling and saddle structures occurring in intrinsically fractal regions corresponding to strange chaotic attractors with Shilnikov saddle-foci in diverse systems. This original computational method based on kneading invariants will greatly benefit in-depth studies of an array of other systems with homoclinic chaotic dynamics, that support the introduction of symbolic partitions.

On a technical side, we note that with the use of GPU parallel simulations and optimized Taylor expansion ODE integrators the time needed for completion of exhausting bi-parametric kneading scans of extra high-resolutions can be reduced by one or two orders.

The reflexion saddle-focus case is discussed in part 3. A general theory is built for the

arrangement of the HBs of a $Z2$ symmetric dynamical system with a saddle-focus. It points out that the scalability ratio of width and distance of $(l+1)$-loop HBs is $e^{-\frac{2\pi}{\Omega_0}}$ if they are in the small neighborhoods of the l-loop HBs. And probably the middle multi-loop HBs are the only visible ones in the structural plots because the rest are much skinnier. Then we did system structure plots of chosen Chua's circuit and each plot has homoclinic bifurcations up to certain order. Those plots verified the theory we built in section 2.

However, the theory only works for the systems when the unstable separatrix of the origin does not get close to the symmetric saddle foci $O_{1,2}$; therefore, the systems are fully decided by the saddle focus at the origin. When the unstable separatrix does travel close to $O_{1,2}$, the theory we built in section 2 no longer works well and the dynamics near $O_{1,2}$ need to be considered. One important concept in this case is T-points. A T-point is a co-dimension 2 point and it plays an organizing role of chaotic system. It is, in fact, a heteroclinic connection between two saddle-focus that have different topological type. In the case of the Chua's circuit, a heteroclinic connection between the origin O and O_1 or O_2 makes a T-point. Bykov studied this kind of T-point (Orbit structure in a neighborhood of a separatrix cycle containing two saddle-foci, Amer. Math. Soc. Transl. (2) Vol. 200, 2000) and concluded that on a bi-parametric plane, there are homoclinic bifurcations that spiral towards a T-point and there are infinitely many T-points in a neighborhood of a T-point.

In addition, there are infinitely many T-points in a reflexion symmetric saddle-focus system according to Bykov ([3]) but many of them are too tiny to be detected due to numerical limitation. For example, there probably is a T-point in the limit of the blue region in the figure 3.17, which is too tiny to be seen. We do see a T-point in our plots (see the figure 5.1). The corresponding trajectories of the T-point is plotted in the figure 5.1. The right unstable separatrix of the origin Γ^+ loops on the right twice and then hits O_1. The trajectory on the 2-dimensional unstable manifold of O_1 intersects the stable manifold of O and converges to O eventually.

In Figure 5.1, we also see an area that accumulates a lot of closed HBs. It is because of a nontransversal T-point. It is illustrated by Antonio Algaba and Manuel Merino etl. ([64]).

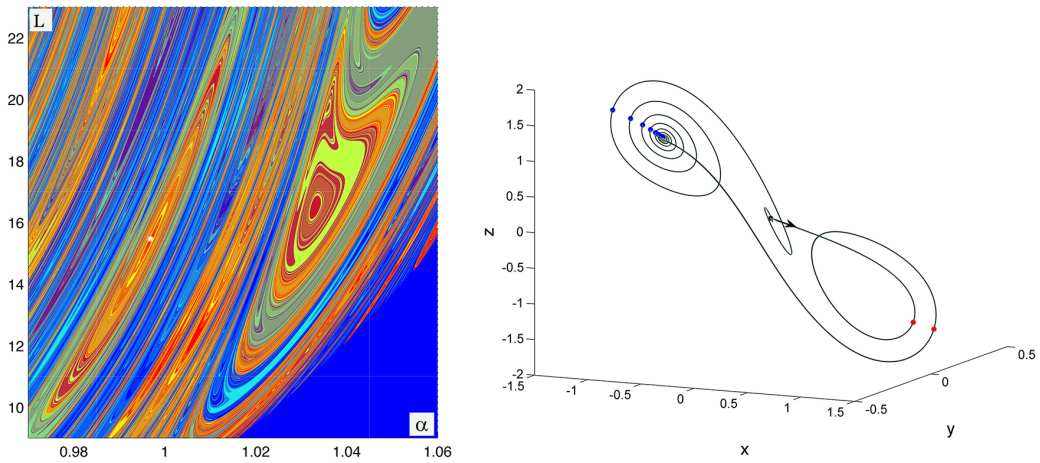

Figure (5.1) The left color picture is a structure scanning on phase plane with $\alpha \in [0.97, 1.06]$ and $L \in [9, 23]$. It is made of 42 panels and has $42 \times 1000 \times 1000$ points. 7-17 kneading subsequence is used for the plotting. The white point in the picture corresponds to a t-point as the center of a typical spiral structure. It is $(0.9971, 15.2888)$ approximately. The trajectory of Γ^+ at this T-point is shown in the right picture.

In three dimensional parametric space, the set of T-points are one dimensional curves and the set of homoclinics are two dimensional surfaces that spiral towards the T-points curves. If a bi-parametric plane cross a T-point curve nontransversally, we will see a lot of closed HBs like in Figure 5.1.

The dissertation also has a chapter on the application of dynamical systems in neuroscience. It discussed a three-cell network of CPGs with reciprocal inhibitory connections. The three cells are all escape cells. A FitzHugh-Nagumo model is used in the study. Both symmetric and asymmetric cases are explored by using phase-lag techniques on a torus. Two traveling-waves and three pace-makers can be detected in some cases while two traveling-waves are the only states for a large range of parameter values. The dynamics can go several ways in an asymmetric network. Interesting results can be seen in some of the figures. The phase-lag technique which is an effective technique can be used to reveal the intrinsic mechanisms of three-cell neuron networks.

Bibliography

[1] L. Shilnikov, A. Shilnikov, D. Turaev, and L. Chua, *Methods of qualitative theory in nonlinear dynamics. Parts I and II.* World Scientific Publishing Co. Inc., 1998,2001.

[2] E. Lorenz, "Deterministic nonperiodic flow," *J. Atmospheric Sci.*, vol. 20, pp. 130–141, 1963.

[3] V. V. Bykov, "On the structure of bifurcations sets of dynamical systems that are systems with a separatrix contour containing saddle-focus.‘," *Methods of Qualitative Theory of Differential Equations, Gorky University (in Russian)*, pp. 44–72, 1980.

[4] L. Shilnikov, "Bifurcation theory and the Lorenz model." *Appendix to Russian edition of "The Hopf Bifurcation and Its Applications." Eds. J. Marsden and M. McCraken*, pp. 317–335, 1980.

[5] V. Afraimovich, V. Bykov, and L. Shilnikov, "The origin and structure of the Lorenz attractor," *Sov. Phys. Dokl.*, vol. 22, pp. 253–255, 1977.

[6] ——, "On structurally unstable attracting limit sets of Lorenz attractor type," *Trans. Moscow Math. Soc.*, vol. 44, no. 2, pp. 153–216, 1983.

[7] L. Shilnikov, "On a problem of poincare and birkhoff," *Math. USSR Sb.*, vol. 3, no. 3, pp. 353–371, 1967.

[8] ——, "Structure of the neighborhood of a homoclinic tube of an invariant torus," *Soviet Math., Dokl.*, vol. 9, no. 3, pp. 624–627, 1968.

[9] ——, "The theory of bifurcations and quaziattractors," *Uspekh. Math. Nauk.*, vol. 36, no. 4, pp. 240–242, 1981.

[10] ——, "Chua's circuit: Rigorous results and future problems," *Inter. J. Bif. Chaos*, vol. 4(3), pp. 489–518, 1994.

[11] ——, "Mathematical problems of nonlinear dynamics: A tutorial. Visions of nonlinear mechanics in the 21st century," *Journal of the Franklin Institute.*, vol. 334(5-6), pp. 793–864, 1997.

[12] ——, "Bifurcations and strange attractors," *Proc. Int. Congress of Mathematicians, Beijing (China) (Invited Lectures).*, vol. 3, pp. 349–372, 2002.

[13] V. Afraimovich and L. Shilnikov, "Strange attractors and quasiattractors," in *Nonlinear dynamics and turbulence*, ser. Interaction Mech. Math. Ser. Boston, MA: Pitman, 1983, pp. 1–34.

[14] D. Turaev and L. Shilnikov, "An example of a wild strange attractor," *Sbornik. Math.*, vol. 189(2), pp. 291–314, 1998.

[15] L. Shilnikov, "A case of the existence of a countable number of periodic motions," *Sov. Math. Dokl.*, vol. 6, pp. 163 –166. Original: On the case of existence of a countable set of periodic movements. *Dokl. Akad. Nauk SSSR* **160**(3), 558–561, 1965.

[16] ——, "The existence of a denumerable set of periodic motions in four-dimensional space in an extended neighborhood of a saddle-focus." *Soviet Math. Dokl.*, vol. 8(1), pp. 54–58, 1967.

[17] ——, "A contribution to the problem of the structure of an extended neighborhood of a rough equilibrium state of saddle-focus type." *Math. USSR Sbornik*, vol. 10, pp. 91–102, 1970.

[18] V. Afraimovich and L. Shilnikov, "On some global bifurcations connected with the disappearance of a fixed point of saddle-node type," 1974, vol. 15, p. 17611765.

[19] ——, "On invariant two-dimensional tori, their breakdown and stochasticity," in *Amer. Math. Soc. Trans.*, ser. translated from Methods of the Qualitative Theory of Differential Equations, Gor'kov. Gos. University, 3–25 (1983). translated from Methods of the

Qualitative Theory of Differential Equations, Gor'kov. Gos. University, 3–25 (1983), 1991, vol. 149, no. 2, pp. 201–212.

[20] N. Gavrilov and L. Shilnikov, "On three-dimensional dynamical systems close to systems with a structurally unstable homoclinic curve. I," *Sbornik: Mathematics*, vol. 14, no. 4, pp. 467–485, 1972.

[21] ——, "On three-dimensional dynamical systems close to systems with a structurally unstable homoclinic curve. II," *Sbornik: Mathematics*, vol. 19, no. 1, pp. 139–165, 1973.

[22] L. Shilnikov, "On a new bifurcation of multidimensional dynamical systems." *Sov. Math. Dokl.*, vol. 10, pp. 1389–1371, 1969.

[23] L. Shilnikov and A. Shilnikov, "Shilnikov saddle-node bifurcation," *Scholarpedia*, vol. 3(4), p. 4789, 2008.

[24] J. Sinai and E. Vul, "Hyperbolicity conditions fro the Lorenz model," *Physica D*, vol. 2, no. 240, pp. 3–7, 1981.

[25] V. Bykov and A. Shilnikov, "On the boundaries of the domain of existence of the Lorenz attractor," *Selecta Math. Soviet.*, vol. 11, no. 4, pp. 375–382, 1992.

[26] W. Tucker, "The Lorenz attractor exists," *C. R. Acad. Sci. Paris*, vol. 328, no. 1, pp. 1197–1202, 1999.

[27] L. Shilnikov, "Some cases of generation of periodic motions in an n-dimensional space." *Soviet Math. Dokl.*, vol. 3, pp. 394–397, 1962.

[28] ——, "Some cases of generation of period motions from singular trajectories." *Mat. Sbornik*, vol. 61(103), pp. 443–466, 1963.

[29] ——, "On the birth of a periodic motion from a trajectory bi-asymptotic to an equilibrium state of the saddle type." *Soviet Math. Sbornik*, vol. 35(3), pp. 240–264, 1968.

[30] R. Barrio, A. Shilnikov, and L. Shilnikov, "Kneadings, symbolic dynamics, and painting Lorenz chaos," *Inter. J. Bif. Chaos*, vol. 22, no. 4, pp. 1 230 016–1 230 040, 2012.

[31] T. Shimizu and N. Morioka, "On the bifurcation of a symmetric limit cycle to an asymmetric one in a simple model," *Physics Letters A*, vol. 76, no. 3-4, pp. 201 – 204, 1980.

[32] A. Shilnikov, "Bifurcations and chaos in the Morioka-Shimizu model. Part I," *Methods of Qualitative Theory of Differential Equations, Gorky University (in Russian)*, pp. 180–193, 1986.

[33] ——, "Bifurcations and chaos in the Morioka-Shimizu model. Part II," *Methods of Qualitative Theory of Differential Equations, Gorky University (in Russian)*, pp. 130–138, 1989.

[34] ——, "Bifurcation and chaos in the Morioka-Shimizu system," *Selecta Math. Soviet.*, vol. 10(2), pp. 105–117, 1991.

[35] A. Shilnikov, L. Shilnikov, and D. Turaev, "Normal forms and Lorenz attractors," *Inter. J. Bif. Chaos*, vol. 3, no. 5, pp. 1123–1139, 1993.

[36] A. Vladimirov and D. Volkov, "Low-intensity chaotic operations of a laser with a saturable absorber," *Optics Communications*, vol. 100(1-4), pp. 351–360, 1993.

[37] N. Petrovksaya and V. Yudovich, "Homolinic loops on the Saltzman-Lorenz system," *Methods of Qualitative Theory of Differential Equations, Gorky University (in Russian)*, pp. 73–83, 1980.

[38] C. Robinson, "Homoclinic bifurcation to a transitive attractor of Lorenz type." *Nonlinearity*, vol. 2, pp. 495–518, 1989.

[39] M. R. Rychlik, "Lorenz attractors through Šilnikov-type bifurcation. I," *Ergodic Theory Dynam. Systems*, vol. 10, no. 4, pp. 793–821, 1990.

[40] A. Shilnikov, "On bifurcations of the Lorenz attractor in the Shimizu-Morioka model," *Physica D*, vol. 62(1-4), pp. 338–346, 1993.

[41] G. Tigan and D. Turaev, "Analytical search for homoclinic bifurcations in the Shimizu-Morioka model," *Physica D*, vol. 18, no. 240, pp. 985–989, 2011.

[42] P. Glendinning and C. Sparrow, "T-points: a codimension two heteroclinic bifurcation," *J. Stat. Phys.*, vol. 43, no. 3, pp. 479–488, 1986.

[43] V. V. Bykov, "The bifurcations of separatrix contours and chaos," *Phys. D*, vol. 62, no. 1-4, pp. 290–299, 1993.

[44] T. Xing, J. Wojcik, R. Barrio, and A. Shilnikov, "Symbolic toolkit for chaos explorations," in *International Conference on Theory and Application in Nonlinear Dynamics (ICAND 2012)*. Springer International Publishing, 2014, pp. 129–140.

[45] T. Xing, J. Wojcik, M. Zaks, and A. Shilnikov, "Multi-fractal kaos," in *Special volume honouring the memory of John S. Nicolis*. World Scientific Publishing Co. Inc., 2014.

[46] L. Shilnikov and A. Shilnikov, "Shilnikov bifurcation," *Scholarpedia*, vol. 2(8), p. 1891, 2007.

[47] J. Guckenheimer and R. F. Williams, "Structural stability of Lorenz attractors," *Inst. Hautes Études Sci. Publ. Math.*, vol. 50, no. 50, pp. 59–72, 1979.

[48] J. L. Kaplan and J. A. Yorke, "Preturbulence: a regime observed in a fluid flow model of Lorenz," *Comm. Math. Phys.*, vol. 67, no. 2, pp. 93–108, 1979.

[49] J. Milnor and W. Thurston, "On iterated maps of the interval," *Lecture Notes in Math.*, vol. 1342, pp. 465–563, 1988.

[50] D. Rand, "The topological classification of Lorenz attractors," *Mathematical Proceedings of the Cambridge Philosophical Society*, vol. 83(03), pp. 451–460, 1978.

[51] M. Malkin, "Rotation intervals and dynamics of Lorenz type mappings." *Selecta Math. Sovietica*, vol. 10, pp. 265–275, 1991.

[52] C. Tresser and R. Williams, "Splitting words and Lorenz braids," *Physica D*, vol. 62(1–4), pp. 15–21, 1993.

[53] V. Bykov and A. Shilnikov, "Boundaries of the domain of existence of a Lorenz attractor," *Methods of Qualitative Theory of Differential Equations, Gorky University (in Russian)*, pp. 151–159, 1989.

[54] S. V. Gonchenko, L. P. Shil'nikov, and D. V. Turaev, "Dynamical phenomena in systems with structurally unstable Poincare homoclinic orbits." *Chaos*, vol. 6, no. 1, pp. 15–31, 1996.

[55] K. Robins, "Periodic solutions and bifurcation structure at high r in the Lorenz model," *Physica D*, vol. 3, no. 36, pp. 457–456, 1979.

[56] V. Franceschini, "A feigenbaum sequence of bifurcations in the Lorenz model," *Physica D*, vol. 3, no. 22, pp. 397–406, 1980.

[57] C. Sparrow, *The Lorenz equations: bifurcations, chaos, and strange attractors*, ser. Applied Mathematical Sciences, Vol. 41. New York: Springer-Verlag, 1982.

[58] B. A. Malomed and A. A. Nepomnyashchy, "Onset of chaos in the generalized Ginzburg-Landau equation," *Phys. Rev. A*, vol. 42, pp. 6238–6240, 1990.

[59] A. I. Khibnik, D. Roose, and L. O. Chua, "How similar is the performance of the cubic and the piecewise-linear circuits of chua?" *International Journal of Bifurcation and chaos*, vol. 3, no. 2, pp. 363–384, 1993.

[60] S. V. Gonchenko, D. V. Turaev, P. Gaspard, and G. Nicolis, "Complexity in the bifurcation structure of homoclinic loops to a saddle-focus," *Nonlinearity*, vol. 10, no. 2, pp. 409–423, 1997.

[61] P. Gaspard, "Generation of a countable set of homoclinic flows through bifurcation," *Physics Letters*, vol. 97, no. 1, pp. 1–4, 1983.

[62] T. Xing, R. Barrio, and A. Shilnikov, "Symbolic quest into homoclinic chaos," *International Journal of Bifurcation and Chaos*, no. 8, 2014.

[63] R. Barrio, F. Blesa, S. Serrano, T. Xing, and A. Shilnikov, "Homoclinic spirals: Theory and numerics," in *Progress and Challenges in Dynamical Systems*. Springer Berlin Heidelberg, 2013, pp. 53–64.

[64] A. Algaba and M. Merino, "Open-to-closed curves of saddle-node bifurcations of periodic orbits near a nontransversal t-point in chua's equation," *International Journal of Bifurcation and Chaos*, vol. 16, no. 9, pp. 2637–2647, 2006.